FACULTY
OF MATHEMATICS
AND PHYSICS
Charles University

DOCTORAL THESIS

ÁBEL KÁLOSI

ELEMENTARY PROCESSES AT LOW TEMPERATURES – REACTIONS OF H_3^+ AND N_2H^+ IN AFTERGLOW PLASMAS

Department of Surface and Plasma Science
Supervisor: doc. RNDr. Radek Plašil, Ph.D.
Scientific advisor: prof. RNDr. Juraj Glosík, DrSc.
Study programme: Physics
Study branch: Physics of Plasmas and Ionized Media

April, 2019

DECLARATION

I declare that I carried out this doctoral thesis independently, and only with the cited sources, literature and other professional sources.

I understand that my work relates to the rights and obligations under the Act No. 121/2000 Sb., the Copyright Act, as amended, in particular the fact that the Charles University has the right to conclude a license agreement on the use of this work as a school work pursuant to Section 60 subsection 1 of the Copyright Act.

Prague, April, 2019

Ábel Kálosi

ACKNOWLEDGEMENTS

During my PhD studies I have been a part of a scientific collaboration with many people who deserve acknowledgement for their contribution to this thesis. I would like to thank my supervisor doc. RNDr. Radek Plašil, Ph.D. for introducing me to the field and my scientific adviser prof. RNDr. Juraj Glosík, DrSc. for giving me the opportunity to participate in the experimental research conducted in his laboratory. I am grateful to both of them for their professional guidance.

I would also like to express my gratitude to Prof. Andreas Wolf and Dr. Oldřich Novotný for offering me the opportunity to stay at the Max-Planck-Institut für Kernphysik in Heidelberg and learn new experimental and computational techniques.

This work would not have been possible without my colleagues from the Laboratory of Elementary Processes in Plasma in Prague, most notably RNDr. Petr Dohnal, Ph.D. and RNDr. Štěpán Roučka, Ph.D., and the E-Cool team in Heidelberg.

BIBLIOGRAPHIC INFORMATION

TITLE: Elementary Processes at Low Temperatures – Reactions of H_3^+ and N_2H^+ in Afterglow Plasmas
AUTHOR: Ábel Kálosi
DEPARTMENT: Department of Surface and Plasma Science
SUPERVISOR: doc. RNDr. Radek Plašil, Ph.D.

ABSTRACT: Electron-ion recombination and ion-neutral interactions play a pivotal role in the chemical evolution of molecules in the Interstellar Medium (ISM). Physical conditions under which these processes undergo in the ISM include a wide range of temperatures and particle number densities. This thesis contributes to the experimental study of named low temperature phenomena in the range of 30 K to 300 K focusing on the reactions of hydrogen-containing light molecules. The employed experimental techniques are based on a combination of a Stationary Afterglow (SA) instrument with a Continuous Wave Cavity Ring-down Spectrometer (cw-CRDS). The main scientific contributions of this thesis can be split into three topics. (1) The proton and deuteron containing isotopic system of H_3^+ ions. The isotopic fractionation process in collisions with hydrogen and deuterium gas was investigated in low temperature discharges, nominal ion temperatures of 80 K to 140 K, by deducing relative ion densities in the experiments. These are necessary for afterglow studies of isotopic effects in electron-ion recombination of the studied ions. (2) Vibrational spectroscopy of N_2H^+ ions focusing on first overtone ($2\nu_1$ band) transitions and ion thermometry, the first step towards studies of electron-ion recombination. (3) The role of *para*/*ortho* spin modifications in the reactive collision system of $H_3^+ + H_2$. The *para*-H_3^+ fraction in afterglow plasmas was investigated as a function of the *para*-H_2 fraction in experiments with *para*-enriched hydrogen gas in the nominal temperature range of 30 K to 60 K.

KEYWORDS: electron-ion recombination, dissociative recombination, astrochemistry, afterglow plasmas, vibrational spectroscopy

PUBLICATIONS

This thesis builds on a series of articles published during the course of the described work. Some ideas and figures have appeared previously in the following publications:

Dohnal, P., Á. Kálosi, R. Plašil, Š. Roučka, A. Kovalenko, S. Rednyk, R. Johnsen, and J. Glosík (2016). 'Binary and ternary recombination of H_2D^+ and HD_2^+ ions with electrons at 80 K.' In: *Physical Chemistry Chemical Physics* 18.34, pp. 23549–23553. DOI: 10.1039/C6CP04152C.

Dohnal, P., D. Shapko, Á. Kálosi, M. Kassayová, Š. Roučka, S. Rednyk, R. Plašil, M. Hejduk, and J. Glosík (2019). 'Towards state selective recombination of H_3^+ ions at astrophysically relevant conditions.' In: *Faraday Discussions*. DOI: 10.1039/C8FD00214B.

Kálosi, Á., P. Dohnal, D. Shapko, Š Roučka, R. Plašil, R. Johnsen, and J. Glosík (2017). 'Overtone spectroscopy of N_2H^+ molecular ions–application of cavity ring-down spectroscopy.' In: *Journal of Instrumentation* 12.10, p. C10010. DOI: 10.1088/1748-0221/12/10/C10010.

Plašil, R., P. Dohnal, Á. Kálosi, Š. Roučka, R. Johnsen, and J. Glosík (2017). 'Stationary afterglow measurements of the temperature dependence of the electron–ion recombination rate coefficients of H_2D^+ and HD_2^+ in He/Ar/H_2/D_2 gas mixtures at $T = 80 - 145$ K.' In: *Plasma Sources Science and Technology* 26.3, p. 035006. DOI: 10.1088/1361-6595/aa5916.

Plašil, R., P. Dohnal, Á. Kálosi, Š. Roučka, D. Shapko, S. Rednyk, R. Johnsen, and J. Glosík (2018). 'Stationary afterglow apparatus with CRDS for study of processes in plasmas from 300 K down to 30 K.' In: *Review of Scientific Instruments* 89.6, p. 063116. DOI: 10.1063/1.5036834.

CONTENTS

I FIRST GLANCES

1 INTRODUCTION 3

2 THEORY 7

- 2.1 Dissociative Recombination 7
- 2.2 Three-body Recombination 10
- 2.3 Spectra of Molecules 11
  - 2.3.1 Angular Momenta 12
  - 2.3.2 Rotational Transitions 12
  - 2.3.3 Vibrational Transitions 13
  - 2.3.4 Electronic Transitions 14
- 2.4 Ion-molecular Reactions 15
  - 2.4.1 Nuclear Spin in Reactive Collisions 17
  - 2.4.2 Isotopic Substitution 17

3 STATE OF THE ART 19

- 3.1 Trihydrogen Cation and Its Isotopologues 19
  - 3.1.1 Symmetries and Quantum Numbers 19
  - 3.1.2 Vibrational Transitions 21
  - 3.1.3 Conversion Reactions 24
  - 3.1.4 DR Rate Coefficients 27
  - 3.1.5 Three-body Recombination 31
- 3.2 Protonated Nitrogen Cation 32
  - 3.2.1 Symmetries and Quantum Numbers 32
  - 3.2.2 Spectroscopic Observations 33
  - 3.2.3 Production Reactions 35
  - 3.2.4 DR Rate Coefficients 37

II EARLY STAGES

4 EXPERIMENTAL TECHNIQUES 43

- 4.1 The Merged-beam Technique 43
  - 4.1.1 The Cryogenic Storage Ring 44
- 4.2 Afterglow Techniques 49
  - 4.2.1 Stationary Afterglow with CRDS 50
  - 4.2.2 Afterglow Analysis 51
  - 4.2.3 Ambipolar Diffusion 55
  - 4.2.4 Chemistry and Temperatures 55
- 4.3 Laser-aided Plasma Diagnostics 58
  - 4.3.1 Laser Absorption Spectroscopy 58
  - 4.3.2 Spectral Line Intensity 60
  - 4.3.3 Spectral Line Shape 61
  - 4.3.4 Optical Cavities 63
  - 4.3.5 Cavity Ring-down Spectroscopy 65
  - 4.3.6 Temporally Resolved CRDS 68

4.3.7 A cw-Cavity Ring-down Spectrometer 69
5 DEUTERATED ISOTOPOLOGUES OF H_3^+ 73
5.1 Statistical Tools 73
5.1.1 The Baseline 74
5.1.2 Differential Signals 76
5.2 Ion Aided Thermometry 78
5.2.1 Translational Temperature 79
5.2.2 Rotational Temperature 82
5.2.3 Neutral Gas Temperature 83
5.3 Isotopic Fractionation 85
5.4 Discussion and Conclusions 87
5.4.1 Systematic Errors 87
6 OVERTONE SPECTROSCOPY OF N_2H^+ 89
6.1 Spectral Survey 89
6.1.1 Wavemeter Calibration 90
6.1.2 Absorption Line Shape 91
6.1.3 Signal Optimisation 91
6.1.4 Molecular Constants 93
6.1.5 Vibrationally Excited States 94
6.2 Line Intensities 95
6.2.1 Rotational Temperature 96
6.2.2 Vibrational Temperatures 98
6.3 Discussion and Conclusions 99

III CRYOGENIC CONDITIONS
7 A CRYOGENIC STATIONARY AFTERGLOW INSTRUMENT 103
7.1 Insulation and Experimental Vacuum 103
7.2 Cryogenics 105
7.3 Microwave Cavity 107
7.4 Microwave Power Source 109
7.5 Cavity Ring-down Spectrometer 110
8 COMPUTER SIMULATED EXPERIMENTS 115
8.1 Plasma in Code 115
8.1.1 A Spatial Approach 116
8.1.2 Hot Electrons in the Discharge 119
8.1.3 What Comes After the Discharge 122
8.1.4 An Afterglow in Equilibrium 123
8.2 Cryogenic Plasmas 124
8.2.1 Plasma Density Profiles 126
8.2.2 Plasma Density Evolution 127
8.3 Through the CRDS 130
8.3.1 Systematic Effects 131
8.3.2 Model vs Experiment 132
8.3.3 Advanced Ring-down Processing 134
8.4 Discussion and Conclusions 136
8.4.1 Predictive Power 136

8.4.2 Final Approach 137

9 CRYOGENIC AFTERGLOW PLASMAS 139

9.1 Pursuit of Sensitivity 139

9.1.1 First Experiments 140

9.1.2 Record Low Temperature 141

9.1.3 Temperature Calibration 143

9.2 Para vs Ortho 144

9.2.1 Para-enriched Hydrogen 145

9.2.2 Spin Manifold Rotational Temperatures 146

9.2.3 Reactive Collisions 147

9.3 Discussion and Conclusions 150

9.3.1 Temperature Estimates 151

9.3.2 Para/Ortho Equilibrium 152

10 SUMMARY AND OUTLOOK 155

BIBLIOGRAPHY 157

IV ATTACHED PUBLICATIONS

A BIBLIOGRAPHIC RECORD 173

LIST OF FIGURES

Figure 1 Potential energy curves and DR pathways. . . 9
Figure 2 Vibrational and electronic transitions in molecules. 16
Figure 3 Rotational levels of H_3^+. 20
Figure 4 Relative ion number densities of the H_3^+ isotopic system. 25
Figure 5 Prediction of the *para*–H_3^+ fraction as a function of the *para*–H_2 fraction. 26
Figure 6 DR rate coefficients of *para*–H_3^+ and *ortho*–H_3^+. 29
Figure 7 DR rate coefficients of the deuterated H_3^+ isotopic system. 30
Figure 8 Simulated first overtone spectrum of N_2H^+. . 36
Figure 9 DR rate coefficients of N_2H^+. 38
Figure 10 Stationary Afterglow with Cavity Ring-down Spectroscopy. 51
Figure 11 Theoretical line shape comparision. 62
Figure 12 Fabry-Perot transmission characteristics. 64
Figure 13 Ion translational temperature. 81
Figure 14 Absorption lines of HD_2^+. 82
Figure 15 Observed relative intensities of HD_2^+ transitions. 84
Figure 16 Relative densities of H_3^+ isotopologues. 86
Figure 17 Comparison of N_2H^+ absorption intensities. . 90
Figure 18 Experimental absorption line shape example. . 92
Figure 19 Doublet absorption line example. 95
Figure 20 Set of observed absorption line intensities. . . 96
Figure 21 Relative intensities of N_2H^+ transitions. 97
Figure 22 Technical schematics of the cryogenic SA-CRDS. 104
Figure 23 Temperature evolution during cool-down and warm-up. 107
Figure 24 Electric field in the microwave resonator. . . . 109
Figure 25 Optical schematics of the cw-CRDS. 111
Figure 26 Longitudinal profile of plasma number density. 117
Figure 27 Normalised longitudinal profiles of effective electron temperature. 121
Figure 28 Longitudinal and radial profiles of normalised H_3^+ number density. 128
Figure 29 Temporal evolution of the plasma model. . . . 129
Figure 30 Temporal evolution of relative effective width parameters. 130
Figure 31 cw-CRDS simulated column number density. . 133

Figure 32 Comparison of cw-CRDS simulated and experimental column number densities. 135
Figure 33 H_3^+ absorption lines at the lowest temperature. 142
Figure 34 Estimators of neutral gas temperature. 143
Figure 35 *Para*-manifold rotational temperature determination of H_3^+. 147
Figure 36 *Para*-H_3^+ fraction determination. 148
Figure 37 *Para*-H_3^+ fraction in afterglow plasmas. 149

LIST OF TABLES

Table 1 Experimentally probed transitions of $H_3{}^+$ istopologues. 22
Table 2 Ground state rotational energy levels of $H_3{}^+$ istopologues. 23
Table 3 Permanent and transition dipole moments of N_2H^+. 35
Table 4 Parameters of the employed cw-CRDS. 74
Table 5 Parameters of the employed laser sources. . . . 76
Table 6 Experimentally probed transitions of the $H_3{}^+$ istopologue system. 80
Table 7 Estimated temperatures in He/Ar/H_2/D_2 experiments. 85
Table 8 Molecular constants of N_2H^+. 94
Table 9 Parameters of the longitudinal diffusion model. 117
Table 10 Parameters of the 2D plasma model. 125
Table 11 Parameters of the enhanced cw-CRDS. 132
Table 12 Experimentally probed transitions of $H_3{}^+$. . . 146

ACRONYMS

ADC Analogue-to-Digital Converter
AOM Acousto-optic Modulator
APD Avalanche Photodiode

CRDS Cavity Ring-down Spectroscopy
CSR Cryogenic Storage Ring
cw-CRDS Continuous Wave Cavity Ring-down Spectrometer

DFB Distributed Feedback
DR Dissociative Recombination

ECDL External Cavity Diode Laser

FA Flowing Afterglow
FALP Flowing Afterglow with Langmuir Probe
FSR Free Spectral Range
FWHM Full Width at Half Maximum

HTS High Temperature Superconductor

ISM Interstellar Medium

MPIK Max-Planck-Institut für Kernphysik

PDE Partial Differential Equation
PEC Potential Energy Curve
PES Potential Energy Surface

RD Ring-down
RF Radio Frequency
RTDs Resistance Temperature Detectors

SA Stationary Afterglow
SA-CRDS Stationary Afterglow with Cavity Ring-down Spectroscopy
SIFT Selected Ion Flow Tube
SMA SubMiniature version A

UHV Ultra High Vacuum
UV Ultraviolet

ZPE Zero-point Energy

Part I

FIRST GLANCES

Where we explore the basic concepts behind elementary interactions of charged molecules with free electrons, and hopefully some other particles too.

1

INTRODUCTION

Gaseous media exposed to ionising radiation or energetic particles contain charged species including atomic and molecular ions. The process through which the positive ions neutralise is known as recombination. It can occur through capture of free electrons or negative ions depending on the physical nature of the ionised media. The energy released in this process corresponds to the ionisation potential. In case of atomic species the only way this energy can be dispersed is either through the emission of radiation or transfer to a third body. In plasmas of relatively low density neither of these processes is very efficient. Recombination of atomic ions with free electrons is generally considered a slow process compared to multi-atomic species. Molecular ions, on the other hand, can effectively undergo dissociative break-up and transform the potential energy into the kinetic energy of the resulting fragments. This process is called Dissociative Recombination (DR) and is the underlying topic of this thesis.

DR has been called many times one of the most complex molecular collision processes since it has been keeping theorists and experimentalist busy for more than half a century. It naturally occurs in a wide range of plasmas from the coldest areas of the Interstellar Medium (ISM) through the ionospheres of planets and moons to the everyday laboratory experiments. First proposals of the aforementioned process were related to the explanation of electron densities in the earth's ionosphere since atomic recombination was known to be too slow to account for the observations. It appeared in publications early as 1937 (still an unnamed process) by, e. g., Massey 1937 and Bates and Massey 1947. DR earned its name together with a theoretical estimate of the recombination rate coefficient from Bates 1950.

It is not the purpose of this introduction to give a thorough review of 60 years of theoretical and experimental research in the field of DR. A collection of basic ideas behind the mechanism of DR can be found in the recent review paper by Florescu-Mitchell and Mitchell 2006, published proceedings of the conference series devoted to *Dissociative Recombination: Theory, Experiment and Application* and also in the excellent book by Larsson and Orel 2008. Up to now we have been referring to DR as a general process of molecular ions, the detailed quantum mechanical description is naturally done on a case by case basis since DR is strongly system dependent. This thesis is further specialised in the case of molecular ions relevant for astrochemistry.

Just as laboratory experiments produce all manners of plasmas of different chemical composition, densities and temperatures so does the visible universe contain a wide range of environments from cold to hot, sparse to dense, almost neutral to completely ionised. The purpose of astrochemistry is to explain the observed abundances of molecular species (neutral, ionised or even negatively charged) that can be readily found in a wide range of physical conditions (Millar 2015). The development of ground based millimetre and sub-millimetre receivers has given rise to a steady flow of newly observed molecules in the ISM (an extensive list is provided by Endres et al. 2016, *CDMS*[1]). Astrochemistry frequently employs complex chemical models to predict the abundances of observed molecules. Even though the networks of chemical reactions employed in these computer simulations contain thousands of possible pathways, DR has been shown to play a key role in molecular synthesis (Geppert and Larsson 2008). One of the challenges of astrochemistry is to keep informed about the properties of already observed molecular species and their possible reactions. This way astrochemistry relies on both laboratory measurements and theoretical groundwork giving motivation and research opportunities in the field of so called laboratory astrophysics.

Generally, laboratory astrophysics is the study of astrophysical phenomena in earth- or space-based laboratory experiments. The most relevant from these for astrochemistry are the study of chemical reactions and spectroscopy of molecules. Although the limit of physical model complexity is usually given by the researcher's ambitions (or computational resources), a crucial point in the development process are reliable laboratory measurements. Without dedicated experiments, our understanding of the origin of complex molecules in the ISM would probably soon reach its limits. Laboratory measurements alone cannot keep up with the requirements of astrochemistry. Advancements in theoretical models are equally needed. These usually come hand in hand with original experimental research. Theory and experiment both inspire and build on each other.

After this introduction of the motivation behind the research presented in this thesis, the attention will be focused on small (three atoms or less) hydrogen containing molecular ions. A special place is reserved in this category for one of the key molecules of astrochemistry, the trihydrogen cation H_3^+. Whenever the importance of DR in astrochemistry is mentioned H_3^+ is waiting close by as the most famous example, the subject of extensive scientific research that goes back to the beginning of the 20th century. Experimental evidence of its existence was abundant but even after the advent of quantum mechanics it took several decades until its stability and triangular configuration was generally accepted. H_3^+, the simplest polyatomic molecule, often serves as benchmark for theoretical calculations. More about the history of H_3^+ and its importance in astrophysics can be found in a review by Oka 2013.

---

[1] The Cologne Database for Molecular Spectroscopy, `https://cdms.astro.uni-koeln.de/cdms/portal/` (October 26, 2018)

Given the experimental orientation of this thesis it is also important to mention the contemporary techniques employed in DR research. These can be divided into two categories: beam and swarm experiments (in alphabetical order). The former is based on the acceleration and manipulation of beams of charged particles in external electric and magnetic fields. In merged-beams experiments the relative energy of the interacting particles can be as low as a few millielectronvolts, only limited by the beam monochromaticity. In the second case, swarms are the collections of particles preferably characterised by a common temperature. A working example is the afterglow plasma where, in the absence of heating sources, the electrons can reach temperatures close to the temperature of the ions as a result of buffer gas cooling.

This thesis describes the advancements made in Stationary Afterglow (SA) instrumentation and in DR research conducted during my doctoral studies. I contributed to several experimental campaigns with a focus on the molecular systems of H_3^+ and N_2H^+. I was also involved in the design and commissioning of a novel cryogenic SA apparatus. The layout of this thesis follows the chronological order of the underlying experimental and technical work.

Part I of the thesis is devoted to a general introduction into the motivation of this thesis, the theoretical background of DR research and to the state of the art knowledge about the molecular systems of interest.

Part II focuses on experimental techniques and diagnostic methods used in the work described by this thesis. This technical introductions is followed by the analysis of two experimental campaigns conducted using a Stationary Afterglow with Cavity Ring-down Spectroscopy (SA-CRDS) apparatus. Part of the data analysis consists of a partial re-evaluation of results published in scientific articles of Dohnal et al. 2016; Plašil et al. 2017 and Kálosi et al. 2017.

Part III presents the advancements in SA instrumentation and the first experiments conducted using the novel cryogenic apparatus. The presented data analysis shares some of the results published in the scientific articles of Plašil et al. 2018 and Dohnal et al. 2019. The current approach combines all the available experimental data with plasma modelling efforts to discuss interpretation of the scientific results. The final chapter of the thesis summarizes the presented results and perspectives on future work.

2

THEORY

In this chapter we will explore the theoretical background of several key topics of this thesis excluding those that are only necessary for the employed experimental techniques and data analysis. Examples of these topics are DR, ion-molecule reactions, three body reactions, ro-vibrational and electronic transitions in molecules. The covered topics provide the basis for an introductory understanding of the DR mechanism and its theoretical and experimental investigations. They are interlinked at least indirectly through quantum mechanics from which their properties are derived. After the introduction to the basic principles of how the listed processes are usually characterised, a brief overview of their relevance for this thesis and application in laboratory experiments or astrophysics is given.

2.1 DISSOCIATIVE RECOMBINATION

It has already been mentioned in the general introduction that DR is a complex molecular collision process of at least two nuclei with all their bound electrons forming a molecular ion and a free electron. Collisional processes are generally characterised by cross sections, i. e., the likelihood of a scattering event as a function of the relative velocity or energy of the colliding particles. The basic ingredient of the calculation of collisional cross sections is the representation of the potential energy of the molecule as a function of its geometrical coordinates, a so called Potential Energy Surface (PES). Applying the Born-Oppenheimer approximation[1] we end up with the adiabatic representation of the PES. When confronted with the problem of graphical representation, the usual approach is to use certain projections of the full PES that is called a Potential Energy Curve (PEC). In the case of diatomic molecules the problem is naturally reduced to a PEC. In the following examples and explanations we will employ the simplified case of diatomic molecules.

The traditional view of the DR mechanism advanced by Bates 1950 is made up of several steps: the incoming electron is captured into an antibonding configuration in which the ionic cores repel each other. This state lies above the ionisation potential of the ground neutral state. As the nuclei move apart they gain kinetic energy and the potential energy of the state drops below the ionisation limit. Thus the system is stabilised against autoionisation. A schematic representation of the process is as follows:

---

[1] Separation of the nuclear and the electronic motion of the molecule due to the large difference in time scales.

$$\mathrm{AB}^{+} + \mathrm{e}^{-} \rightleftharpoons \mathrm{AB}^{**} \longrightarrow \mathrm{A} + \mathrm{B}\,\cdot \tag{1}$$

This so called 'direct' mechanism is the most effective when a suitable crossing of the ionic ground state and a repulsive state exists. The aforementioned crossing does not violate the non-crossing rule since the repulsive state is diabatic in form. The cross section that arises from this mechanism has a $1/E$ energy dependence, where E is the kinetic energy of the interacting particles (Mitchell 1990).

Further complications arise from the fact that there is an infinite series of Rydberg states[2] that converges to the ionic ground state. Vibrationally excited levels of these states lie above the ionisation potential of the neutral molecule and are accessible for electron capture. This can be followed by autoionisation or pre-dissociation into a suitable repulsive state, leading to stabilisation. This pathway was labelled the 'indirect' mechanism of recombination. The interference between both channels can lead to sharp resonances in the DR cross sections. Independent formalisms for both pathways were set down by Bardsley 1968a,b and later pioneered by the work of O'Malley 1971.

A simple graphical example of both pathways with only three PECs involved is given in Figure 1. We start from a vibrational level of the ionic state labelled AB^{+} and represented by full lines. Even though the repulsive state AB^{**} does not cross our vibrational level, the direct mechanism can still be effective at higher energies represented by the length of the arrow connecting these states. However, at a lower energy we see an accessible vibrational level of a Rydberg state of the neutral molecule labelled AB^{R} and represented by dashed lines. When the incoming electron's energy equals the difference between the two vibrational levels the electron can be captured and the molecules can pre-dissociate following the same repulsive curve leading to the products A and $\mathrm{B}(nl)$. Here we introduce the symbol (nl) indicating that the products of DR often end up in excited electronic states.

Following even the simplest explanation of the DR pathways it is evident that fully *ab initio* quantum mechanical calculations are computationally demanding. Not only the accurate PES of the ionic ground state is necessary, but also those of accessible repulsive neutral states and the series of Rydberg states. This is followed by an analysis of the dynamics which can result in cross sections and branching ratios for the product states. For systems without a suitable curve crossing the complexity of the calculations further increases due to the inclusion of non-adiabatic couplings. An example for this is the simple diatomic system of HeH^{+} (Čurík and Greene 2017). Rotational motion can also enrich the structure of DR cross sections.

---

[2] Electronically excited state with a high principal quantum number n.

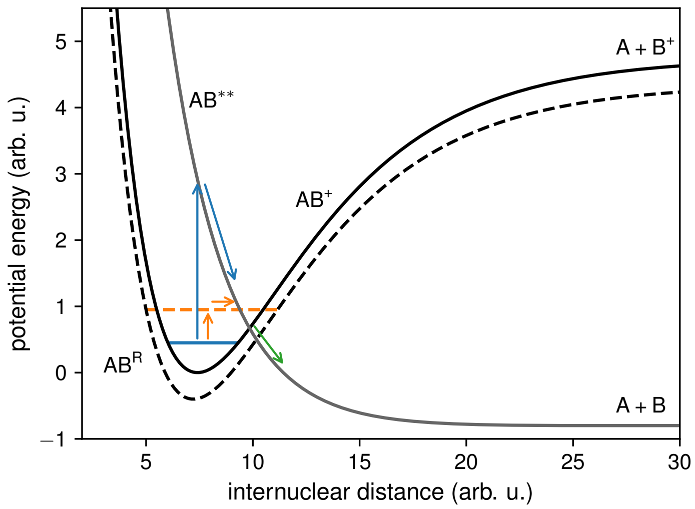

Figure 1. Potential energy curves and DR pathways for the cases of direct and indirect recombination. The vibrational energy of the initial ion is represented by the full horizontal line. Depending on the kinetic energy of the incoming electron (represented by the length of the vertical arrows), it can be captured into a vibrationally excited Rydberg state (AB^R, horizontal dashed line). At higher energies the repulsive state (AB^{**}) is directly accessible for electron capture. The direction of the arrows show the steps into dissociation. See text for further details.

When considering a polyatomic molecule, effects as the Jahn-Teller coupling play an important role in the DR mechanism. Its inclusion can result in, e. g., two orders of magnitude difference in calculated cross sections. This coupling between electronic and rotational-vibrational states leads to the distortion of the geometry of the molecule. An immediate result is the lifting of degeneracies and a difference of energies in final electronic states. An almost textbook example of the described complexity is the (misleadingly called) simplest polyatomic ion, ${H_3}^+$ (Kokoouline and Greene 2003; Kokoouline, Greene, and Esry 2001). This discovery was driven by the disagreement of theory and experiment.

After this brief overview we can attempt to summarise pieces of the DR puzzle which are needed to advance our theoretical understanding (not sorted according to importance):

1. High resolution experimental cross sections that reveal the positions and magnitude of important resonances. These can be directly linked to key pathways and the underlying PES.
2. Absolute values of measured cross sections or of their averaged counterparts the so called rate coefficients (defined later in this chapter).

3. Rotationally resolved state to state information that includes both the detection of branching ratios and also complete control over the initial rotational population of studied ions.

4. Development of novel calculations dealing with the ever increasing complexity of polyatomic molecules.

Recent experimental developments in DR research have been in great part devoted to the third point of this list, to experimental apparatuses whose purpose lies in the preparation of rotationally cold ions. Complications and solutions arise both in small and large scale experiments. Both an overview and this thesis's contributions will be discussed in the next chapters.

2.2 THREE-BODY RECOMBINATION

In the previous section we considered the ideal case of exactly two particles interacting with each other. In experiments, purely from a practical point of view, we need thousands of particles interacting with each other to produce a measurable signal. For example, when relating theory to beam experiments we consider the distribution of velocities with respect to some frame of reference when comparing cross sections or more precisely rate coefficients. The number of particles in a beam can have an influence on the final distribution of velocities but usually does not change the picture we have described by what we should call three-body interactions. As mentioned in Chapter 1, there is yet another class of experiments where charged particles are not confined by electro-magnetic fields but rather by neutral gas of intermediate pressures.

Generally, in plasma afterglow experiments the so called neutral buffer gas plays several roles: it slows down the diffusion of particles (confinement), thermalises the electrons through elastic collisions (cooling) and also influences the ion composition by ion-neutral interactions (chemistry). With an increase of the number of particles in a given volume the probability of three particles interacting with each other becomes comparable with that of two-body interactions. Practical values of when this effect becomes observable are left for the following chapters.

For the purpose of this theoretical introduction we will start with the simpler picture of atomic ions. Here the problem of tracking multiple collisions compared to molecules is generally tractable. Naturally, DR is an exclusively molecular process. Its atomic counterpart is the so called radiative recombination where capture of an electron is followed by emission of a photon. Radiative recombination is the inverse process of photo-ionisation, making it important for atomic physics. In the case of singly charged ions, radiative recombination cross sections are generally several orders of magnitude lower than those of DR. Once we include a third particle in this picture we open up an additional pathway how to redistribute the released potential energy, schematically:

$$A^+ + e^- + N \longrightarrow A + N\,. \tag{2}$$

The additional particle circumvents the involvement of photons making the process of purely collisional character. But our model is not yet complete since we are considering high number densities where such a collision is highly probable. In this scenario we need to inspect the distribution of product states that can range up to very high n, lying close to the ionisation limit. These states can decay, i. e., lose energy by emission of a photon or through another inelastic collision with our particle N, or can also be collisionally ionised. The final rate of recombination at a given set of physical conditions is given by master equations describing the interplay between collisional and radiative processes. The third particle N can be both an electron or a neutral atom or molecule. Theoretical calculations of the described mechanism for atomic ions can be found in the papers from Bates and Khare 1965 and Stevefelt, Boulmer, and Delpech 1975.

Returning to the case of molecular ions, we face the problem of replacing the radiative processes by the ability of molecules to dissociate and also to form ro-vibrationally excited states with considerable lifetime. There are only a few theoretical works and experimental measurements that describe this situation. Further references will be given in the cases relevant for this thesis.

2.3 SPECTRA OF MOLECULES

So far we have introduced the term states as in electronic, vibrational or rotational states of molecules with corresponding energy levels. This terminology is a direct consequence of the Born-Oppenheimer approximation where couplings between the different motions of electrons and nuclei are usually treated as perturbations in the theory. Following this, we define the energy of a given state as:

$$E = E_{\mathrm{el}} + E_{\mathrm{vib}} + E_{\mathrm{rot}}, \tag{3}$$

where the subscripts represent the listed states. Radiative transitions between two energy levels can be a result of the absorption of a photon in the lower state, emission of a photon from the upper state or also the stimulated emission of a photon from the upper state when interacting with a photon of the same energy. An important tool in labelling the states is the use of quantum numbers which also help to identify allowed transitions. The number of quantum numbers needed to describe the system depends on the number of degrees of freedom and also the symmetries of the molecules. Molecular spectroscopy is a strong example for the power of symmetries and a useful tool in experimental physics and astrophysics. It allows us to investigate properties of molecules also important for DR. In the following text we will highlight the most important features of molecular spectroscopy, rigorous introductions can be found in many textbooks, here we will be follow the definitions of Bernath 2015.

2.3.1 *Angular Momenta*

Selection rules in molecular spectroscopy arise from the combination of symmetries and conservation laws, namely that of the conservation of total angular momentum. Main constituents are the orbital and spin angular momenta of the electrons and the rotational angular momentum of the nuclear motion. Interactions between these momenta result in the so called fine structure splitting of electronic energy levels. Although spin-orbit coupling is also present in atoms, what makes the molecular case different is the presence of a special symmetry axis like the molecular axis in diatomic molecules. Summation of angular momenta need to take into account the projections where in certain cases only these projections result in good quantum numbers. The label 'good' means good approximation in the context of molecular spectroscopy. Similar phrases are often used to indicate the approximations involved.

Nuclei of the molecule can also posses non-zero spin which results in the so called hyperfine structure. As the name indicates the splitting of the rotational levels is orders of magnitude lower, usually not resolved in laboratory rotational spectra but nonetheless important in the detection and assignment of astrophysical spectra. Bending mode vibrations in polyatomic molecules can result in vibrational angular momenta further enriching the complexity of the systems.

2.3.2 *Rotational Transitions*

Pure rotational transitions in molecules are associated with the change of the total angular momentum quantum number J. Rotational energy levels can also be expressed as a function J, for example in the case of a diatomic molecule in an electronic state with zero orbital and spin momenta and neglecting the hyperfine structure we can use the expression:

$$F_v(J) = B_v J(J+1) - D_v\left[J(J+1)\right]^2 + H_v\left[J(J+1)\right]^3 + \dots \tag{4}$$

where the subscript v indicates a dependence on the vibrational quantum number (state) v of the so called rotational constant and its higher order correction terms in the form:

$$B_v = B_e - \alpha_e\left(v + 1/2\right) + \gamma_e\left(v + 1/2\right)^2 + \dots \tag{5}$$

Energy expressions of this type are readily used as the basis for more complex electronic states and also for polyatomic molecules with the addition of further quantum numbers. Deduction of the molecular parameters from observed spectra is one of the products of rotational spectroscopy.

In the case of electric dipole transitions the selection rules allow the change of J by one quantum. For diatomic molecules this results in the characteristic $\approx 2B_v$ spacing of rotational lines. Only molecules possessing a permanent electric dipole moment exhibit this type of spectrum. This excludes all homonuclear molecules (at least in their ground states) due to symmetry restrictions. There are higher order terms like the quadrupole electric moment where J changes by two quanta thus allowing the detection of interstellar H_2 in sufficiently warm regions (Rosenthal, Bertoldi, and Drapatz 2000).

Another showcase of the power of symmetries in H_2 is the existence of the so called *para* and *ortho* spin isomers. Protons posses a nuclear spin of $1/2$ and, following the rule of spin-statistics, are labelled as fermions obeying the Pauli exclusion principle. Its direct consequence is that the total wavefunction of the molecule must be antisymmetric upon permutation of two identical fermions. There are two possibilities how to add up the nuclear spins I: in an antisymmetric way with total $I = 0$ (*para*) and a symmetric way with total $I = 1$ (*ortho*). Only the rotational wavefunctions have alternating symmetries thus *para* states are associated with even $J = 0, 2, 4 \ldots$ values and *ortho* states odd $J = 1, 3, 5 \ldots$ values. The separation is so strong that without a suitable catalyst or a reaction the two isomers behave like different molecules. The radiative lifetime of the lowest *ortho* state is estimated to be on the order of the age of the universe (Pachucki and Komasa 2008).

2.3.3 *Vibrational Transitions*

A widely employed model to describe vibrational levels in diatomic molecules and interactions based on PECs is the analytical Morse potential. It is a convenient method to represent the potential function of an anharmonic oscillator. Energy levels and wavefunctions can be calculated analytically to be used for graphical representation. A more advanced approach is to approximate the potential by a power series expansion to arbitrary precision developed by Dunham 1932. Solving the Schrödinger equation of the ro-vibrational motion leads to another double power series energy expression:

$$E_{vJ} = \sum Y_{ij} \left(v + 1/2\right)^i \left[J\left(J+1\right)\right]^j \tag{6}$$

for an electronic state with zero orbital and spin momenta. This representation is equivalent to the customary Herzberg expression of Equation 4 with the addition of the vibrational energy power series:

$$G(v) = \omega_e (v + 1/2) - \omega_e x_e (v + 1/2)^2 + \omega_e y_e (v + 1/2)^3 + \ldots \quad (7)$$

by making the correspondences of the Dunham coefficients Y_{ij} and the rotational and vibrational molecular parameters.

Vibrational transitions (electric dipole) are not driven by the permanent dipole moment of the molecule and so the intensity of the transitions are calculated by the application of the dipole moment operator on the initial and final wavefunctions. In the Born-Oppenheimer approximation this is done by the calculation of the dipole moment function. Similar to the PES of the electronic state, the dipole moment function is the parametric dependence of the dipole moment on the nuclear coordinates. In the diatomic case a power series expansion of this function demonstrates that the constant term (the permanent dipole moment) does not contribute to the line strength because the vibrational wavefunctions are orthogonal. Due to the general anharmonicity of the PECs in diatomic molecules the vibrational selection rules are more flexible than for rotations. According to the change in the vibrational quantum number we have the fundamental transitions $\Delta v = \pm 1$ and overtone transitions $\Delta v = \pm 2, 3, \ldots$. The intensity of the transitions with increasing Δv is decreasing quickly, usually an order of magnitude at each step.

Rotational selection rules are somewhat different as opposed to purely rotational transitions. Possible values of ΔJ are $-1, 0, +1$ labelled as P-, Q-, R-branches in molecular spectroscopy. Q-branches are also special in this category, only certain vibrational transitions posses it in polyatomic molecules or electronic states with non-zero electronic angular momenta. Neglecting the coupling between rotation and vibration leads to the introduction of so called Hönl-London factors (rotational line strengths) which are for most types of transitions tabulated in the literature. Homonuclear diatomic molecules are again left with quadrupole and higher order terms resulting in O- and S-branches ($\Delta J = -2$ or $+2$).

2.3.4 *Electronic Transitions*

Electronic transitions in molecules combine all the characteristics of both vibrational and rotational transitions giving rise to rich spectra consisting of vibrational bands with rotational substructure. Assignments of spectra become complex when the electronic configuration of the involved states contributes with non-zero angular momenta. There are no simple formula to calculate the energies of low-lying electronic states. These are done in *ab initio* calculations or derived from observed spectra.

Furthermore, the intensity distribution of the vibrational bands follows a different rule. Falling back to the Born-Oppenheimer approximation, the overall intensity of the transitions is derived from the transition dipole moment of the electronic wavefunctions similar to pure vibrational transitions. This already involves two sets of PES and dipole moment functions. Selection rules generally involve the electron spin and orbital momenta and any other symmetry restrictions for the given molecule often categorized into allowed and forbidden transitions. The term forbidden is best translated as transitions with orders of magnitude lower intensities compared to allowed ones. The vibrational part of the transition strength depends solely on the overlap of the vibrational wavefunctions called the Franck-Condon principle. Considering that the PES involved may have widely different shapes and positions of minima the intensity distribution of vibrational bands is unique for each transition.

An example of electronic and vibrational transitions for a model diatomic molecule is shown in Figure 2. The length of the arrows translate into the energy of absorbed or emitted photons. For each vibrational level (horizontal lines) the amplitude of the wavefunctions is shown since this comes into the calculations of overlap and transition intensities. In this example the excited state wavefunction has a better overlap with higher vibrational states of the electronic ground state. Rotational levels are left out of the example. These obey similar selection rules as in the purely vibrational case with intensity factors depending on the type of electronic transitions.

2.4 ION-MOLECULAR REACTIONS

The driving mechanism behind the chemical evolution of the coldest areas of the ISM can be greatly attributed to ion-molecular reactions. They create complex species which can undergo DR in various ways and often represent concurrent processes to DR. A simple definition of cold molecular clouds is a gaseous environment where reactions between ions and neutral molecules are orders of magnitude more effective then those involving only neutrals. Main reasons why ion-molecular interactions are so effective at low temperatures is the general absence of potential barriers and the polarisability of molecules by an electric charge. The so called Langevin model is a simple estimate for the rate coefficient of ion-molecule reactions for non-polar molecules.

Similar behaviour can be observed in low-temperature discharge experiments with intermediate pressures that can produce a variety of complex molecules in the form of ions and radicals from simply gaseous precursors. With the right set of physical conditions we can achieve the production of the desired species. Simple chemical models can be readily tested against experimental observations thanks to

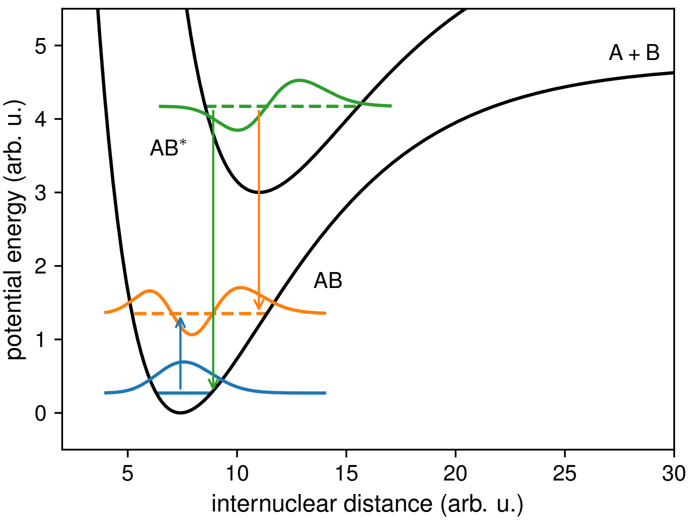

Figure 2. Vibrational and electronic transitions in molecules. The horizontal lines indicate the vibrational energy levels with respect to the electronic states. The highlighted vibrational states are chosen to represent differing quantum numbers. The amplitude of the wavefunctions indicate the possible areas of overlap. Although the upper electronic state is depicted to lie close for visualisation purposes, in case the energy difference between the lower vibrational levels is negligible compared to the electronic transition energy itself the resulting vibrational level population is governed by the Franck-Condon factors.

control over the basic reactants. Although there are much simpler ways to study individual reactions, e. g. merged beam setups or multi-pole ion traps, these sources can be readily used in molecular spectroscopy (Crabtree et al. 2012; Talicska et al. 2016).

The term intermediate pressures is referred to conditions where ion-molecular reactions are affected, similar to three-body recombination, by the presence of additional neutrals. For example, we can observe the enhancement of association processes that otherwise would proceed only through emission of radiation (Gerlich et al. 2013; Plašil et al. 2012). Furthermore, cluster formation can be also enhanced that results in loosely bound species at temperatures where collisional dissociation is still effective. Clustering processes play a dominant role with decreasing temperature (Hiraoka 1987).

In this thesis we will pay special attention to two similar cases of reactive collisions that do not change the chemical composition of the reactants, namely isotopic substitution and nuclear spin conversion. Both are recognised as a source of mystery but also provide valuable observational information on the ISM conditions.

2.4.1 *Nuclear Spin in Reactive Collisions*

As mentioned in Section 2.3.2, nuclear spin configurations in certain molecular systems lead to the existence of two or more distinct states that effectively behave as different molecules in certain cases. This is the case of H_2 and ${H_3}^+$ in the ISM. In the absence of strong interactions of the nuclear spins with intra- or extra-molecular magnetic fields, the approximation of frozen nuclear spin leads to strict selection rules in reactive collisions due to the conservation of the magnetic momenta of each nuclei (Oka 2004; Quack 1977).

In this framework the collision system of H_2 and ${H_3}^+$ can be systematically represented as:

$$
{H_3}^+ + \widetilde{H}_2 \rightleftharpoons \begin{cases} {H_3}^+ + \widetilde{H}_2 \\ \widetilde{H}_2H^+ + H_2 \\ H_2\widetilde{H}^+ + H\widetilde{H} \end{cases} \tag{8}
$$

where the rows represent identity, proton hop and proton exchange, respectively. The reaction proceeds through proton scrambling via the $({H_5}^+)^*$ collision complex. Both molecules come in two possible spin configurations (*para* and *ortho*). It is possible to calculate state-to-state reaction probabilities for given nuclear spin configurations using statistical methods (Gómez-Carrasco et al. 2012; Park and Light 2007).

The direct consequence of this mechanism is that in environments where H_2 is the dominant collision partner of ${H_3}^+$ the ratios of *para* and *ortho* states are strongly coupled in both molecules and directly linked to physical parameters such as excitation or translational temperatures. On the other hand, observed discrepancies in molecular clouds indicate that there are further mechanisms competing with this collisional thermalisation process (Albertsson et al. 2014).

2.4.2 *Isotopic Substitution*

From the electron point of view the molecules H_2 and HD in the Born-Oppenheimer approximation are identical. Further non-adiabatic corrections would change certain electronic properties but the main distinction between the isotopes for gas phase chemistry lies in the difference in thermochemical properties and the so called vibrational Zero-point Energy (ZPE)[3]. This isotopic shift in ZPE is a function of the reduced mass of the nuclei. The largest shift can be observed in light molecules but the direction of the energy shift nevertheless points to the same conclusion: isotopic substitution of heavier isotopes leads to molecules with lower energies. Combined with temperatures lower than the differences between ZPEs of different isotopes this process leads to isotopic fractionation, the enrichment of heavier isotopes relative to the most frequent one.

---

[3] The vibrational motion of molecules lead to a difference between the lowest point of the PES and the lowest vibrational level.

In this thesis we will consider the case of deuteron containing molecules, although in astrophysical plasmas isotopes of heavier atoms are also frequently observed and used as 'probes' (White 1997). The abundances of present-day elements combined with model calculations are used to trace the history of nucleosynthesis in different parts of the universe and are the basis of comparison when considering isotopic fractionation (Wilson 1999). Primordial nucleosynthesis produced light elements all the way up to ^{7}Li. Subsequent stellar processing has been producing the heavier elements where deuterium is believed to be destroyed by these processes. Nonetheless, the estimated global ISM D/H ratio based on observation is still close to the predicted primordial value of roughly 2×10^{-5} (Weinberg 2017).

When looking at the dominant constituent of the dense ISM, i. e., molecular hydrogen, deuterium substitution has a peculiar effect. The molecule HD is no longer restricted by symmetry and can be observed by its purely rotational spectrum, whereas cold H_2 can only be detected by Ultraviolet (UV) absorption of stellar radiation. The observed or predicted ratios of HD/H_2 are in the range of 10^{-2} to 10^1 times the primordial value (Gay et al. 2011; Lacour et al. 2005). Lower observed ratios can be the product of differences in molecule formation on dust grains and variation of the fraction of molecules over the sightlines where effects such as self-shielding against UV radiation is much more effective for higher abundances of H_2. On the other hand, enhancement of the deuterated forms is the preferred prediction of chemical models implying that even fully deuterated forms are indeed feasible.

Observations of molecules lying further in the chemical evolution chain are showing even higher degrees of fractionation, in some cases tens of percent (Coutens et al. 2016; Huang and Öberg 2015). These observations are still demanding interpretation in the form of chemical models. Without laboratory measurements, these rely heavily on extrapolation for the deuterated isotopologues. And again we return back to the core example of $H_3{}^+$ now showing up in its deuterated forms, from which H_2D^+ and $HD_2{}^+$ have been both detected and are believed to play an important role in the fractionation process (Millar 2005). To satisfy the demands of these modelling schemes, spin configurations for all the deuterated isotopologues have been included in recent works (Kong et al. 2015).

3

STATE OF THE ART

This chapter's purpose is to collect available literature data on all the processes studied in the course of this thesis and any other physical constants linked to the studied molecules. Where review papers are available, data are extracted from these publications without providing a fully detailed historical review. Further data were collected from publications accessible to the author covering the available literature.

3.1 TRIHYDROGEN CATION AND ITS ISOTOPOLOGUES

This section is organised according to processes and properties of the ions considered in this thesis. Isotopic effects are compared for the listed processes rather than considering each of the species by itself. As the title indicates, we are considering the system of the trihydrogen cation where some of the protons may be substituted by its neutron possessing isotope deuteron. The four possible configurations are: ${H_3}^+$, H_2D^+, ${HD_2}^+$ and ${D_3}^+$. These species differ by masses, ZPEs, rotational and vibrational energy spacing and also basic symmetries that play a major role in DR.

3.1.1 *Symmetries and Quantum Numbers*

An important convention of this thesis: when we are talking about the symmetries of a molecule we are usually considering the ground state. As we have already mentioned in Chapter 2, some of the symmetries can be broken by the motion of the molecule leading to peculiar quantum mechanical effects. The ground states of ${H_3}^+$ and ${D_3}^+$ posses D_{3h} symmetries and those of H_2D^+ and ${HD_2}^+$ posses $C_{2\nu}$ symmetries. All of the isotopologues have *para* and *ortho* nuclear spin configurations and ${D_3}^+$ has an additional *meta* configuration.

In the case of ${H_3}^+$ and ${D_3}^+$ we are adopting the rotational and vibrational state labelling of Lindsay and McCall 2001. Only the total angular momentum and parity are rigorous quantum numbers for any molecule. Due to the weak interaction of nuclear spin and nuclear motion, the quantum numbers of the individual angular momenta I and J, respectively, are considered to be good quantum numbers. In addition, at low energies we can work with additional approximately good quantum numbers ν_1 and ν_2 of the ν_1 breathing and ν_2 bending vibrational modes, as well as with the vibrational angular momentum l associated with the degenerate ν_2 mode (which takes values of $\nu_2, \nu_2 - 2, \ldots, -\nu_2 + 2, -\nu_2$). The projection of J onto the molecular symmetry axis k is usually a good quantum number for molecules. Due to the symmetry properties of ${H_3}^+$ (and ${D_3}^+$) the levels with the same $|k - l|$ are near degenerate, so it is useful to define $G \equiv |k - l|$ and use it instead to label the rotational states together with J. Additionally, when $l \neq 0$ certain combinations of k produce the same G, these rotational levels are distinguished by labels '*u*' and '*l*' for *upper* and *lower*, respectively. Each species has a different rule for pairing the rotational states with the respective nuclear spin configurations. For ${H_3}^+$, states with $G = 3n$ belong to the *ortho* spin modification and states with $G = 3n \pm 1$ belong to the *para* spin modification for any integer n. Additionally, states with even J and zero G are forbidden by the Pauli exclusion principle, which makes the lowest state of *para* configuration. For ${D_3}^+$ states with $G = 0$ and even J belong to the *meta*, states with $G = 0$ and odd J belong to the *para* spin modifications. States with $G = 3n$ belong to both *meta* and *para*, and states with $G = 3n \pm 1$ belong to the *ortho* spin modification. An example of rotational energy pattern in the case of ${H_3}^+$ with its most relevant rotational states for this thesis is shown in Figure 3.

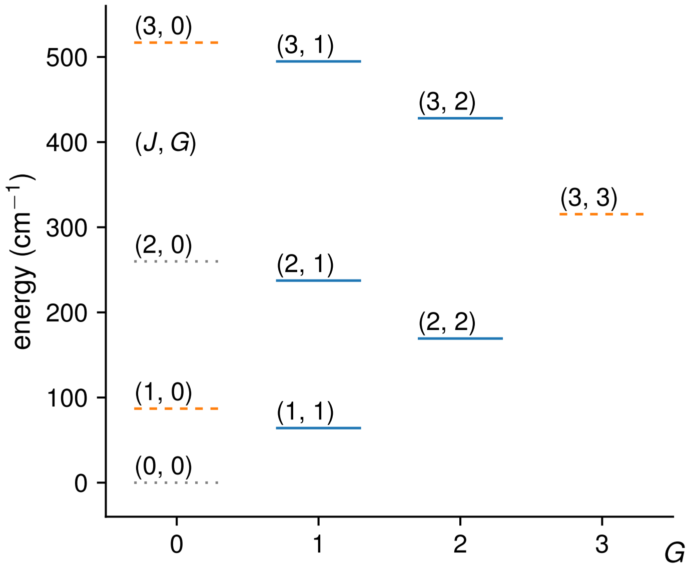

Figure 3. The lowest rotational energy levels in the ground vibrational state of ${H_3}^+$. Solid and dashed lines represent *para* and *ortho* states, respectively, labelled by the rotational quantum numbers (J, G). The dotted lines indicate states forbidden by the Pauli exclusion principle. The energy values are taken from Lindsay and McCall 2001 and are relative to the forbidden $(0, 0)$ state.

In the case of H_2D^+ and ${HD_2}^+$ the rigorous quantum numbers are also valid but there are no degenerate vibrational modes. We are adapting the level labelling of Asvany et al. 2007. Vibrational states are represented by three approximate quantum numbers $v_1 v_2 v_3$ (symmetric stretching, bending and antisymmetric stretching modes). The rotational states are represented by the combination of the nuclear angular momentum J and two approximate quantum numbers K_a and K_c which are the projection values for the limiting prolate and oblate symmetric tops. Selection rules for the spin modifications are again different for the two species. For H_2D^+ states with K_a odd belong to the *ortho* and states with K_a even belong to the *para* spin configuration. For ${HD_2}^+$ states with $K_a + K_c$ even belong to the *ortho* and states with $K_a + K_c$ odd belong to the *para* spin configuration. The listed classifications for nuclear modifications of all the isotopologues are those described by Hugo, Asvany, and Schlemmer 2009, where the convention follows: *ortho* states have the highest high-temperature statistical weights (or in the case of ${H_3}^+$ the highest nuclear spin degeneracy), followed by *meta* and *para*. For a complete list of symmetry representations and degeneracy factors of the full isotopic system of ${H_3}^+$ and H_2 see the cited publication.

3.1.2 *Vibrational Transitions*

The vibrational transitions of the isotopologues probed in the experiments presented in this thesis are either second overtone or combination band transitions. For all the molecules the strongest transitions are coupled to the ν_2 mode which is also considered infrared active. Pure vibrational transitions for the ν_1 mode are forbidden by symmetry restrictions. It can become allowed through rotation-vibration interactions but still is the weakest of the observable bands. In the case of the H_2D^+ and ${HD_2}^+$ the ν_2 and ν_3 modes can couple strongly due to strong rotation interactions. Since in the experiments we were not attempting to measure previously unobserved or unpredicted transitions, the rotational selection rules are not discussed here in detail, for further information see the above cited publications.

The full list of transitions used in this thesis is given in Table 1. The listed transition wavenumbers $\tilde{\nu}$ are split into two categories: experimentally observed values are taken from Lindsay and McCall 2001; Asvany et al. 2007 and Dohnal et al. 2016, theoretically calculated values are taken from Sochi and Tennyson 2010; Mizus et al. 2017 and private sources, as explained further. The transitions are labelled separately for the rotational and vibrational part. For ${H_3}^+$ and ${D_3}^+$ the labels are J_G for the rotational states (the ambiguous states are further labelled by a superscript $\{u|l\}$, as previously explained) and $(\nu_1, \nu_2^{|l|})$ of the upper state for the vibrational band. For H_2D^+ and ${HD_2}^+$ the labels are $J_{K_a K_c}$ for the rotational states and (ν_1, ν_2, ν_3) for the vibrational band. The lower state of all transitions is the respective ground vibrational state of the molecules. The Einstein coefficients A are taken from the same sources as the calculated transition wavenumbers. Since the ground state energy levels and Einstein coefficients of spontaneous emission used in this thesis are taken from a combina-

ION	$\tilde{\nu}$ (cm^{-1})		TRANSITION		A (s^{-1})
	OBS.	CALC.	ROT.	VIB.	
$H_3{}^+$	6807.297^a	6807.335^d	$2_3 \leftarrow 3_3$	$(0, 3^1)$	17.81
	6877.546^a	6877.553^d	$1_2 \leftarrow 2_2$	$(0, 3^1)$	17.18
	7234.957^a	7235.007^d	$4^l_3 \leftarrow 3_3$	$(0, 3^1)$	10.08
	7237.285^a	7237.304^d	$2^u_1 \leftarrow 1_1$	$(0, 3^1)$	5.05
	7241.245^a	7241.239^d	$2_0 \leftarrow 1_0$	$(0, 3^1)$	9.08
H_2D^+	6459.036^b	6458.794^e	$2_{02} \leftarrow 1_{11}$	$(0, 2, 1)$	2.47
	6466.532^b	6466.300^e	$1_{11} \leftarrow 0_{00}$	$(0, 2, 1)$	4.10
	6491.349^b	6491.124^e	$2_{12} \leftarrow 1_{01}$	$(0, 2, 1)$	4.49
$HD_2{}^+$	6466.936^b	6466.916^b	$1_{01} \leftarrow 1_{10}$	$(1, 2, 0)$	2.41
	6535.953^b	6535.943^b	$2_{12} \leftarrow 1_{01}$	$(1, 2, 0)$	2.28
	6536.319^b	6536.301^b	$1_{11} \leftarrow 0_{00}$	$(1, 0, 2)$	1.68
$D_3{}^+$	6848.505^c	6848.712^f	$3_2 \leftarrow 2_2$	$(0, 3^1)$	0.37

Table 1. A complete list of transitions of the $H_3{}^+$ isotopologues used in the various experiments presented in this thesis. For a description of the transition labelling and used sources see the text. The wavenumbers $\tilde{\nu}$ are given with the precision of the experimentally observed values. [a]Lindsay and McCall 2001; [b]Asvany et al. 2007; [c]Dohnal et al. 2016; [d]Mizus et al. 2017; [e]Sochi and Tennyson 2010; [f]Private sources.

tion of theoretical predictions and experimental measurements, in the following, the sources and reliability of the calculations are discussed for each molecule.

For $H_3{}^+$ the energy level values are taken from Furtenbacher et al. 2013. These are the result of a combined evaluation of experimental data taking into account an extensive list of measured transitions. In this reference the energy difference between the *para* and *ortho* spin manifolds is determined using a series expansion of the rotational energy expression taken from Lindsay and McCall 2001. The precision for the involved states is on the order of the error of the experimental transition measurements. The Einstein A coefficients are taken from the theoretical work of Mizus et al. 2017, based on a fully *ab initio* model. Values used in our previous publications were taken from Neale, Miller, and Tennyson 1996, here the PES involved in the calculation of the energy levels and transition strengths was spectroscopically adjusted to experimental measurements. The relevant Einstein coefficients are believed to be reliable within five percent.

From a literature point of view the case of $H_3{}^+$ has been studied most extensively compared to its deuterated isotopologues. Experimentally determined energy level values for H_2D^+ and $HD_2{}^+$ can be

ION	STATE	SPIN	E (cm^{-1})	
			EXP.	CALC.
$H_3{}^+$	1_1	*para*	64.121[a]	64.123[d]
	1_0	*ortho*	86.960[a]	86.966[d]
	2_2	*para*	169.294[a]	–
	3_3	*ortho*	315.354[a]	315.316[d]
H_2D^+	0_{00}	*para*	0	0
	1_{01}	*para*	45.703[b]	45.697[e]
	1_{11}	*ortho*	60.034[b]	60.026[e]
$HD_2{}^+$	0_{00}	*ortho*	0	0
	1_{01}	*para*	34.917[c]	34.918[f]
	1_{10}	*para*	57.989[c]	57.989[f]
$D_3{}^+$	2_2	*ortho*	–	85.628[f]

Table 2. A complete list of ground vibrational state rotational energy levels of the $H_3{}^+$ isotopologues probed in the various experiments presented in this thesis. The rotational states are labelled the same as in Table 1, see text for explanation. The spin configurations for each state are also given. The lower state energy values E are given with the precision of the experimentally observed values, see text for a discussion of the chosen sources.
[a]Furtenbacher et al. 2013; [b]Foster et al. 1986; [c]Polyansky and McKellar 1990; [d]Mizus et al. 2017; [e]Sochi and Tennyson 2010; [f]Private sources.

found in Foster et al. 1986 and Polyansky and McKellar 1990. These are the results of similar procedures as in the case of $H_3{}^+$. Experimental energy values for $D_3{}^+$ are not tabulated in the literature, only the spectroscopically adjusted PES is available (Amano et al. 1994). Only recently have theoretical calculations been published for H_2D^+ (Sochi and Tennyson 2010), providing necessary details about the theoretical model that was used to produce the Einstein coefficients appearing in Asvany et al. 2007. The transition strengths for $HD_2{}^+$ and $D_3{}^+$ used in this thesis are the products of similar high accuracy *ab initio* quantum mechanical calculations, even though a full list has never been published[1]. The stated precision of the Einstein coefficients is similar to that of the $H_3{}^+$ values as it can be seen from the comparison of predicted energy values with experimental works.

---

[1] The full electronic lists of $HD_2{}^+$ and $D_3{}^+$ transitions are not published. Values for $D_3{}^+$ have been obtained from Jonathan Tennyson, University College London (September 14, 2004). Values for $HD_2{}^+$ were also published in Asvany et al. 2007. For $H_3{}^+$ and H_2D^+ the line lists are alternatively available from `http://exomol.com/` (December 12, 2018).

The full list of ground vibrational state rotational levels probed in the experiments presented in this thesis can be found in Table 2. Both experimentally determined energy values, taken from Foster et al. 1986; Polyansky and McKellar 1990 and Furtenbacher et al. 2013, and theoretically calculated energy values, taken from Sochi and Tennyson 2010[1] and Mizus et al. 2017, are given for comparison. The energy values are relative to the respective $J = 0$ states.

Partition functions for all the molecules are determined by direct summation. This technique is computationally quite inexpensive for below room temperature experiments and can be done to high precision without including a large amount of levels. Partition functions fitted to polynomials are available in the literature and were used for comparison to eliminate any errors. This approach is justified by the possible non-thermal spin configuration distribution encountered in certain experiments, for which literature partition functions are not always available.

3.1.3 *Conversion Reactions*

Isotopic substitution, as previously explained, is driven by the differences in ZPEs of the initial and product molecules. In the case of the $H_3{}^+$ + H_2 isotopic system these processes have to also obey nuclear spin selection rules. As an example we can take the reaction between the lowest rotational states of *para*—$H_3{}^+$ and *ortho*—D_2

$$\text{p-H}_3{}^+ + \text{o-D}_2 \rightleftharpoons \begin{cases} \text{p-H}_3{}^+ + \text{o-D}_2, \ \Delta E = 0\,\text{K} \\ \text{o-H}_2\text{D}^+ + \text{HD}, \ \Delta E = 66\,\text{K} \\ \text{p-H}_2\text{D}^+ + \text{HD}, \ \Delta E = 152\,\text{K} \\ \text{o-HD}_2{}^+ + \text{o-H}_2, \ \Delta E = 169\,\text{K} \\ \text{o-HD}_2{}^+ + \text{p-H}_2, \ \Delta E = 339\,\text{K} \end{cases} \tag{9}$$

with channels ranked by the energy released in the reactions (the products are also in the respective lowest rotational states) in customary units of energy divided by the Boltzmann constant (E/k_B).

Several models are available in the literature that deal with either the *para/ortho* conversion reaction or the isotopic substitution separately. A comprehensive work was done by Hugo, Asvany, and Schlemmer 2009 uniting both approaches to derive state to state specific reaction rate coefficients for the individual spin configurations in the isotopic system. Motivated by astrochemical models, these rate coefficients were derived for temperatures up to 50 K and shown to be consistent with the detailed balance and thermodynamic equilibrium constants. Experimental data are also available for some of the thermally averaged rate coefficients, the good overall agreement between these data and the theoretical predictions encourages its use for modelling purposes.

A second thermally averaged model that we consider in this thesis was applied by Fárník et al. 2002 to a slit supersonic expansion discharge source to derive ion number densities depending on the relative D_2 number density

$$F_{D_2} \equiv [D_2] \,/\, \big([H_2] + [D_2]\big) \tag{10}$$

in the source gas mixture. The conditions for which the model was applied are similar to those in our experiments, but they adjusted two of the rate coefficients to fit the measured data. A comparison of both models is shown in Figure 4. In both cases only the conversion reactions are considered leading to a steady state between the isotopologues depending only on the relative D_2 ratio (F_{D_2}) and independent of the absolute number densities.

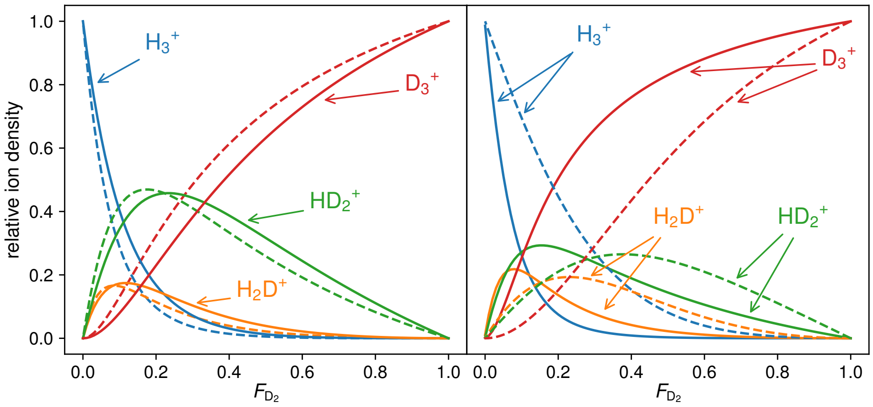

Figure 4. Relative ion number densities of the deuterated H_3^+ isotopologues as a function of relative D_2 number density (F_{D_2}). Each line is labelled by the corresponding species. The left panel shows the model of Hugo, Asvany, and Schlemmer 2009. Dashed lines represent the calculated rate coefficients at the highest directly investigated temperature of 50 K. The full lines are based on extrapolated values for 70 K derived from the published temperature dependences. The right panel shows the model of Fárník et al. 2002. Full lines are calculated from the '71 K' rate coefficients and the dashed lines from the 300 K values.

The model of Hugo, Asvany, and Schlemmer 2009 can be also employed to predict the *para*—H_3^+ fraction

$$p_3 \equiv \left[p\text{-}H_3^+\right] / \left[H_3^+\right] \tag{11}$$

as a function of the *para*—H_2 fraction

$$p_2 \equiv \left[p\text{-}H_2\right] / [H_2] \tag{12}$$

for an ensemble in steady state. Calculated predictions in the translational (collisional) temperature range of 30 K to 60 K are shown in Figure 5. Direct comparison of the predicted values with those calculated from the respective partition functions in equilibrium of translational and excitation temperatures shows us the consistency of the employed model. At temperatures higher than 50 K a possible loss in accuracy can account for the difference.

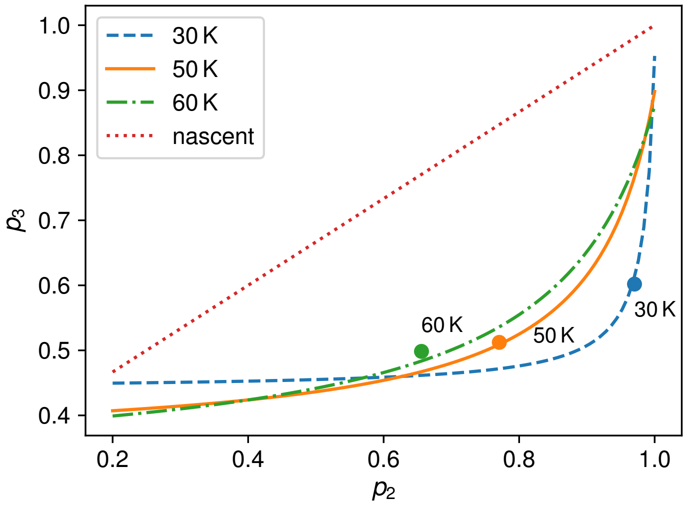

Figure 5. Prediction of the *para*—$H_3{}^+$ fraction as a function of the *para*—H_2 fraction calculated by employing the model of Hugo, Asvany, and Schlemmer 2009. Each line is labelled by the corresponding translational (collisional) temperature. The plotted filled circles show the corresponding values for the equilibrium of translational and excitation temperatures. The *para*—$H_3{}^+$ fraction in the case of pure nascent production is also shown for comparison.

Now considering the production of $H_3{}^+$, the simplest approach is to assume that the molecules are formed purely in the reaction of $H_2{}^+ + H_2$. Adopting the statistical branching ratios of Oka 2004, we can derive the so called nascent distribution

$$p_3 = 1/3 + 2/3 p_2. \tag{13}$$

of $H_3{}^+$ production. This is also shown for comparison in Figure 5. In a collisional environment, such as a discharge or even a molecular cloud, we would expect to find the measured values lying in between the plotted lines depending on the ratio of the production, thermalisation and destruction reactions. A peculiarity of laboratory experiments is that hydrogen gas is usually stored at room temperature and has a p_2 fraction characteristic for high temperature statistical mixtures, i. e., the product of statistical weights and densities of states. For translational temperatures below 200 K this so called normal hydrogen represents a non-thermal mixture of *para*—H_2 and *ortho*—H_2.

The last point where these conversion reactions play a role in H_3^+ oriented experiments is the distribution of vibrational excitation. The highly exothermic production reaction $H_2^+ + H_2$ leads to a release of 1.71 eV internal energy[2] that is sufficient to populate several vibrational states of the product H_3^+ molecule. On the other hand, scrambling of the atoms in the $(H_5^+)^*$ reaction complex can lead to the apparent transfer of the vibrational energy to the H_2 molecule. These vibrationally excited states represent a small fraction of all the H_2 molecules. The final vibrational distribution is a product of production and thermalisation reactions similarly to the p_3 fraction.

3.1.4 *DR Rate Coefficients*

The highlight of this section and the basis of all future DR experiments is the collection of literature data on experimental and theoretical DR rate coefficients. Plasma afterglow and storage ring data are directly compared only when thermal rate coefficients are available, otherwise the reader is referred to the respective publications without reproducing the cross section data in graphical form.

The process of DR can be schematically represented for H_3^+ as

$$H_3^+ + e^- \longrightarrow \begin{cases} H_2 + H, \ \Delta E = 9.2\,\text{eV} \\ H + H + H, \ \Delta E = 4.7\,\text{eV} \end{cases} \tag{14}$$

with two possible breakup channels where the product neutrals, as might be expected from the amount of energy available, can end up in excited states. The branching fractions between the channels was studied by Datz et al. 1995 in a wide range of collision energies. Below 0.3 eV roughly 75 % of the product states end up as three separate hydrogen atoms. Although not an important H atom production mechanism in our experiments, nonetheless an interesting fact that the low energy DR of H_3^+ partly slows down the process of molecular H_2 formation.

As stated in Section 2.1, one of the principal goals of DR research is to supply chemical models with state to state rate coefficients. In the case of H_3^+ this can be experimentally realised by reaching temperatures where only the lowest two *para* and *ortho* states are populated and controlling the *para* fraction via reactive collisions with H_2. There were numerous storage ring experiments conducted at CRYRING and TSR (and also at other facilities) dedicated to the measurement of DR cross sections for *para*–H_3^+ and *ortho*–H_3^+, summarised in a recent review by Kreckel et al. 2012. Attempts were made to produce and maintain rotationally cold ion beams in these experiments. The rate coefficients published in several papers are claimed to be measured in such conditions that the ion beams can be characterised with rotational temperatures on the order of tens of kelvins, as measured in the employed ion sources (McCall et al. 2003, 2004). Subsequent systematic studies, both theoretical and experimental, showed that the pre-cooled ions in the ring are heated up to room temperature (Kreckel et al. 2010; Petrignani et al. 2011). These studies were conducted utilising a set of different ion sources and techniques such as supersonic expansion and ion trapping, also producing rotationally hot (several thousand kelvins) ion beams to further advance the comparison with theoretical predictions. Awareness to the probably higher than stated rotational temperatures was raised by a highly advanced, fully *ab initio* theoretical publication by Fonseca dos Santos, Kokoouline, and Greene 2007, who calculated rotationally resolved DR cross sections. An independent analytical approach was also developed by Jungen and Pratt 2009 that agrees well with both experiment and complex theory.

---

[2] Calculated as the difference of proton affinities according to the NIST Chemistry Webbook, `http://dx.doi.org/10.18434/T4D303`, (November 29, 2018).

In the meantime, afterglow measurements were struggling to come up with a single value and, producing various values in different experiments, kept filling the range between $10^{-9}\,\mathrm{cm}^3\,\mathrm{s}^{-1}$ and several times $10^{-7}\,\mathrm{cm}^3\,\mathrm{s}^{-1}$. Some views favoured the possibility of an extremely low DR rate coefficient until the storage rings became convincing enough with their precision and authority. This lead to the claimed discovery of an extremely fast (compared with theoretical predictions for atoms) helium-assisted three-body recombination channel by Glosík et al. 2008. The proposed mechanism and experimental evidence will be discussed separately. Thanks to this interpretation, afterglow data were shown to be comparable with both theory and storage ring experiments. A final explanation was also offered for the observed H_2 dependence of the measured rate coefficients by Johnsen and Guberman 2010 which seemed to close the open questions about the afterglow experiments. More on the history of the involved experiments and theoretical work can be found in Larsson 2012.

The last phase of the experimental efforts focused on addressing the *para*/*ortho* dependence. Both storage ring and afterglow experiments used *para*-enriched H_2 gas to extract DR rate coefficients for *para*–${H_3}^+$ and *ortho*–${H_3}^+$. The final extrapolated results are shown in Figure 6. The data are grouped by technique and labelled by spin configuration. The prefixes 'p' and 'o' are short for *para* and *ortho*. 'TDE' refers to the thermally averaged values by the respective *para* and *ortho* fractions. In the case of the storage rings thermally averaged DR rate coefficients are hard to come by, partly due to the complicated procedure of data deconvolution. Tom et al. 2009 offer tabulated values at 300 K that are plotted as symbols, circle for *para* and square for *ortho*. The dotted line labelled CRYRING shows typical storage ring temperature dependence, in this case that of McCall et al. 2004. An important detail to keep in mind is that the rotational excitation probably does not correspond to the collisional temperature in these experiments and the plotted trend is dominated by the collisional temperature. The afterglow data, plotted as full lines with one sigma error bands, are taken from Hejduk et al. 2015. The 'TDE' full line is the direct fit of data that are believed to correspond to the equilibrium fractions of *para* and *ortho* states. The dashed line is the extrapolation of the individual *para* and *ortho* curves. Theoretically calculated values are taken from Pagani et al. 2009, where tabulated values of the Fonseca dos Santos, Kokoouline, and Greene 2007 theory were published. The near perfect agreement between the 'TDE' values of theory and extrapolated afterglow results might seem to be surprising, but there is in fact a slight disagreement between the *ortho* values, which are the important ones for modelling purposes, and the question is still open whether theory fails to explain the experiment or the estimated uncertainties are overly optimistic.

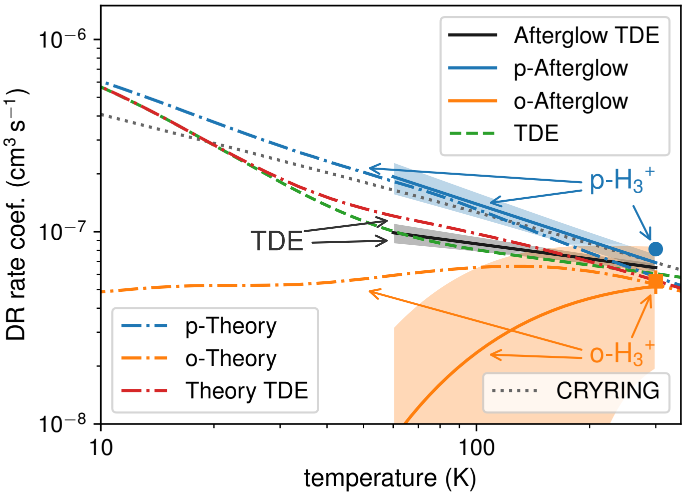

Figure 6. State of the art experimental and theoretical DR rate coefficients of *para*–H_3^+ and *ortho*–H_3^+. Data are grouped by the techniques by which they were obtained. The symbols and the dotted line represent CRYRING publications (McCall et al. 2004; Tom et al. 2009). The full and dashed lines are the product of our experimental efforts with afterglow plasmas (Hejduk et al. 2015). *Ab initio* theoretical calculations are represented by the dot-dashed lines (Fonseca dos Santos, Kokoouline, and Greene 2007; Pagani et al. 2009). See text for a thorough explanation of the used sources.

The relative ratio of the values from Tom et al. 2009 at 300 K is slightly higher than the theoretical prediction but the difference is less than two sigma of purely statistical uncertainties. There is room to improve in every experiment and hopefully the newly commissioned CSR will bring renewed energy into this research field. In the meantime, the goal of our afterglow experiments is to keep pushing the lower limits on the temperature scale.

Turning our attention to the full isotopic system of $H_3{}^+$ we can soon realise far the most complete starting point is theory. DR rate coefficients derived in a fully *ab initio* theoretical approach similar to Fonseca dos Santos, Kokoouline, and Greene 2007 are available for all nuclear spin configurations of all the deuterated isotopologues. These values, taken from Pagani et al. 2009, are show in Figure 7 for the case of thermal equilibrium fractions of spin configurations. In this same publication the calculated results are compared to the values used in earlier astrochemical models. The analytical approach of Jungen and Pratt 2009 is not reproduced here since the overall agreement between the theories is rather good and the rotational dependence in the latter theory is not shown in the publication.

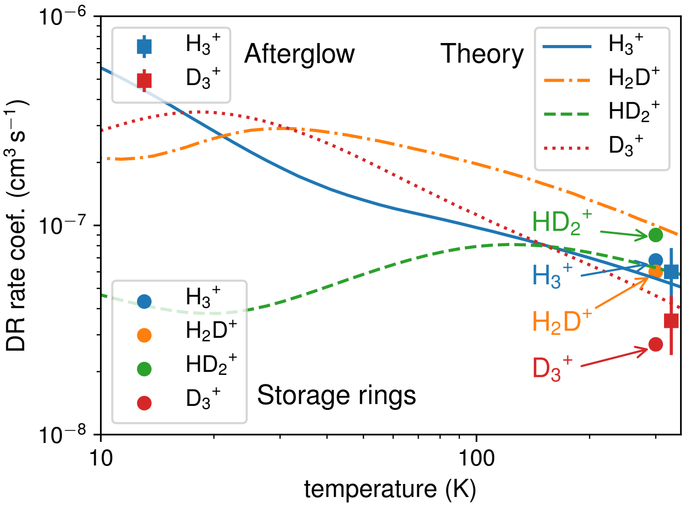

Figure 7. State of the art DR rate coefficients of the deuterated $H_3{}^+$ isotopic system for the case of thermal equilibrium fractions of spin configurations. Lines labelled by the isotopologues represent the temperature dependence of fully *ab initio* theoretical calculations (Pagani et al. 2009). Experimental results of storage rings (Larsson et al. 1996; Padellec et al. 1998; Zhaunerchyk et al. 2008 and Tom et al. 2009), circles, and afterglow experiments (Rubovič et al. 2013), squares, are shown for 300 K only. The afterglow data are shifted to higher temperatures for clarity. The sources of the data are explained in the text.

Storage ring data are shown only for 300 K since any plotted temperature dependence would probably not include the rotational state dependence of the rate coefficients. Sources of the storage ring data are Larsson et al. 1996; Padellec et al. 1998; Zhaunerchyk et al. 2008 and Tom et al. 2009. Known systematic issues with these experiments are the following. Possibility of above room temperature rotational excitation of the ions. This issue was most extensively investigated in the case of $H_3{}^+$. The $D_3{}^+$ data come before this time and may be affected by unknown rotational excitation. Both H_2D^+ and $HD_2{}^+$ posses dipole moments and can rotationally relax by emission of radiation.

In the case of H_2D^+ beams, ${D_2}^+$ ions can contaminate the beam due to the small mass difference between the ions that is generally hard to separate. In the case of ${HD_2}^+$ even sub-thermal rotational populations produced through electron cooling were observed by Lammich et al. 2003.

Up to this point no afterglow experiments attempted to study the DR rate coefficients of H_2D^+ and ${HD_2}^+$ due to the impossibility of producing these ions as the dominant species in afterglow plasmas. The answer lies in the already presented chemical models, which predict even in the best case a strongly mixed distribution of the relative ion populations. As a reference point and comparison with storage ring data, the room temperature values for ${H_3}^+$ and ${D_3}^+$ are also shown in Figure 7, taken from Rubovič et al. 2013.

3.1.5 *Three-body Recombination*

The helium-assisted three-body recombination channels of ${H_3}^+$ and ${D_3}^+$ are exclusive to the afterglow experiments. The most convincing evidence pointed out by Glosík et al. 2008 is that results obtained in different experimental setups can be united by this approach. In the proposed data analysis an effective recombination rate coefficient is extracted from the recorded ion or electron number density evolution at a given pressure. The DR (or binary) rate coefficient is extrapolated from this pressure dependence by assuming that

$$\alpha_{\mathrm{eff}} = \alpha_{\mathrm{bin}} + K_{\mathrm{He}} \times [\mathrm{He}] \,. \tag{15}$$

As already mentioned, the chemistry in afterglow plasmas has to be checked for the experimental conditions, whether the assumption of a purely recombining character is valid for the recorded ion number density evolutions. Such an effect can lead to the already observed H_2 number density dependence in SA experiments below roughly $10^{13}\,\mathrm{cm}^{-3}$. Further unification efforts of ${H_3}^+$ afterglow experiments lead to an additional proposed channel of hydrogen-assisted three-body recombination that was found to be even faster than the helium channel (Dohnal et al. 2014; Glosík et al. 2015). Furthermore, at sufficient number densities these channels seem to interfere and saturate at a common value.

The temperature dependence of the helium-assisted three-body recombination rate coefficients are relatively flat in most of the investigated temperature range for both ions. The ${D_3}^+$ data experience a drop below 100 K and approach the predictions of classical theories for atoms. These finding were summarised by Johnsen et al. 2013, also offering theoretical arguments for the overall observed behaviour. This explanation involves long-lived excited states of the ${H_3}^+ + e^-$ collision complex that are stabilised by collisions with helium atoms against auto-ionisation thus enhancing the observed recombination rate but without further interfering with the binary channel. Main source of criticism for this proposed process and the interpretation of afterglow data is the absence of an electron-assisted three-body recombination channel that is estimated to be observable at the lowest accessible temperatures. A rigorous theoretical approach is badly needed that would provide definite predictions for such a mechanism also taking into account a possible dependence on the electron number density. A similar trend is expected in the cases of H_2D^+ and ${HD_2}^+$ ions.

3.2 PROTONATED NITROGEN CATION

This section is organised in a similar manner as the one dedicated to ${H_3}^+$, but focusing more on the spectroscopy of the molecule rather than its DR. The protonated nitrogen cation N_2H^+ is almost second in importance next to ${H_3}^+$ for astronomical models and observations. Thanks to its relatively high permanent dipole moment, it is easily detected in radio-astronomical observations. in fact, several emission lines of its rotational transitions were detected in these spectra before being studied in the laboratory (Turner 1974). These lines were assigned to N_2H^+ thanks to the observed hyperfine splitting induced by the spin of the outer nitrogen nucleus (Green, Montgomery, and Thaddeus 1974).

Since the first observations N_2H^+ have been detected in various environments, e. g., dark clouds, protoplanetary disks and star-forming regions (Daniel et al. 2007; Dutrey et al. 2007; Schlingman et al. 2011). It is often used as a chemical tracer of the CO snowline (Qi et al. 2015; van 't Hoff et al. 2017), a region where CO and N_2 freeze out onto dust grains, radically changing the chemical composition of the cloud. The interpretation of these observations of N_2H^+ abundances is mediated through the use of complex astrochemical models. In denser regions, dominant formation and destruction pathways are proton transfer from ${H_3}^+$and to CO, and also DR with free electrons. For the sake of completion we should mention that the deuterated isotopologue N_2D^+ is equally important for astrochemistry and isotopic fractionation, not studied in the course of this work.

3.2.1 *Symmetries and Quantum Numbers*

The N_2H^+ molecular ion possesses a closed shell ground electronic state, isoelectronic with that of the isomer pair HCO^+ and HOC^+, which happen to be also of interest for astrochemistry. It can be characterised by a $C_{\infty v}$ symmetry group in its ground state, i. e., it is a linear molecule. Concerning isotopes, we consider only $^{14}N_2H^+$ if not stated differently. There are two possible configurations for the ^{15}N containing molecules with considerably large isotopic shifts for our experimental resolution to differentiate. Considering the low fractional abundance of $^{14}N^{15}N$ on the order of 0.7 % in the precursor nitrogen gas and the possible splitting between the two configurations, these molecules are not assumed to play a major role in the experiments. Each atom of all the possible isotopic configurations possesses nuclear spin 1 or 1/2. Since there are no symmetry restrictions for the rotational states to pair up with the spin states the only way spins manifest is the hyperfine splitting of the states that is orders of magnitude below our resolution.

Yet again the rigorous quantum numbers we can make use of are the total angular momentum J and parity of the states, where we adopt the labels 'e' and 'f'. The low lying vibrational states (below the barrier of isomerisation) can be well described by three approximate vibrational quantum numbers that correspond to the ν_1 N−H stretching (or NN···H, depending on the representation), ν_2 degenerate bending and ν_3 N−N stretching vibrational modes. Similar to ${H_3}^+$, the degenerate bending mode is associated with a vibrational angular momentum l. For $|l| \neq 0$ the degeneracy is lifted due to rotational-vibrational interactions and the rotational levels are split into states with different parity. It is important to keep in mind that J represents the total angular momentum including the vibrational one and so the lowest rotational level has $J = |l|$. Purely vibrational states are represented by $(\nu_1, \nu_2^{|l|}, \nu_3)$ where states with $|l| \neq 0$ are doubly degenerate.

3.2.2 *Spectroscopic Observations*

Due to the fact that N_2H^+ is one of the most extensively investigated molecular ion, the literature is rich in published observations of its spectra and derived molecular parameters. Thanks to rotational spectroscopy and astronomical observations, these parameters have been determined to a great precision not only for the ground state but for all three of the lowest excited states of each vibrational mode. Isotopic effects and shifts have been investigated also to a similar extent. A large number of vibrational states have been probed by infrared laser absorption spectroscopy and other methods showing the rich level structure of such a simple molecule. For an overview and revision of most existing laboratory and astronomical transition frequency determinations see the publication by Amano, Hirao, and Takano 2005, who were the first to observe pure rotational transitions of N_2H^+ in its excited vibrational states. These measurements, driven by the precision needs of astronomical detection, and revision of data were later extended by Yu et al. 2015, who determined state of the art molecular parameters, for additional isotopes too.

In this thesis we are adopting the customary labelling of rotational-vibrational transitions of linear molecules. The rotational part is labelled as $\Delta J(J'')$, where J'' is the total angular momentum of the lower state. For the vibrational part, e. g., band, we have two approaches. One is to use the general symbol

$$(v_1', v_2'^{|l'|}, v_3') \leftarrow (v_1'', v_2''^{|l''|}, v_3''),$$

where prime and double prime designate upper and lower states, respectively. The direction of the arrow signalises whether we are considering absorption or emission. For transitions originating from the ground vibrational state we can alternatively use only the upper state vibrational quantum numbers (v_i) of modes (ν_i) that change in the transition, as in $v_1\nu_1$.

The most extensive experimental study of the vibrational structure of N_2H^+ was done by Kabbadj et al. 1994. Employing an effective Hamiltonian, fundamental molecular parameters were determined in a simultaneous fit of a large amount of observed transitions. Thanks to this approach, energy levels of states not directly observed can be also predicted. Alternatively, effective molecular parameters for each vibrational state are also available that can be used to calculate the rotational energy levels in the form of Equation 4. These data are also needed to calculate partition functions of the molecule, either by direct summation of all the energetically accessible states or separately for the rotational states of any vibrational state of interest combined with a vibrational partition function. For the second approach it is sufficient to know the harmonic frequencies and degeneracies of the vibrational modes.

The literature is equally rich from a theoretical point of view. Calculations have been developing over the years at a steady rate reaching the fully three-dimensional level. Špirko, Bludský, and Kraemer 2008 calculated a fully *ab initio* PES and corresponding dipole moment surface for the ground electronic state and determined the energy levels of all bound vibrational states. The agreement with experimental values is almost at a spectroscopic level for the ν_1 mode, slightly worse for the ν_2 mode and the worse for the ν_3 mode, but even in this case the error is below the percent level. Moreover, the permanent dipole moment of the molecule (Havenith et al. 1990) and the transition dipole moment for the ν_1 fundamental band (Keim et al. 1990) have been both experimentally determined and the agreement is better than the experimental uncertainties. Another *ab initio* calculation relevant for this thesis was done by Botschwina 1984. The theoretically calculated and experimentally determined values are compared in Table 3 for selected transition types. The permanent dipole moment determines the strength of purely rotational transitions.

Generally, the strongest transitions are linked to the ν_1 mode to such an extent that the first overtone $2\nu_1$ transition has a comparable transition dipole moment to the fundamental ν_3 transition. The $2\nu_1$ band is a perfect candidate to probe the rotational ground states of N_2H^+ in our frequency range of interest. The first experiment to

TRANSITION	DIPOLE MOMENT		
	EXP.	CALC.; 2008	CALC.; 1984
Gnd. rot.	3.4(2)	3.446	3.374
$\nu_1 \rightarrow$ gnd.	0.23(2)	0.244	0.284
$2\nu_1 \rightarrow \nu_1$	–	0.357	0.412
$2\nu_1 \rightarrow$ gnd.	–	0.0167[a]	0.0136

Table 3. Comparison of theoretically calculated and experimentally determined permanent and transition dipole moments of N_2H^+ for selected transitions. The sources of the values are explained in the text. [a]Not published in the original publication, obtained through private communication from Vladimír Špirko, Charles University, Prague.

observe part of the $2\nu_1$ band of N_2H^+ was conducted by Sasada and Amano 1990 using a Distributed Feedback (DFB) laser diode. Theory also predicts that the combination band transitions between low lying states where only the ν_1 quantum number changes have roughly the same transition dipole moments independent of the other quantum numbers thanks to the small interactions between the different modes. Figure 8 shows simulated spectra of the $2\nu_1$ band of N_2H^+ for the expected ion number density in a discharge at 300 K. We used a combination of molecular parameters from Kabbadj et al. 1994 and Yu et al. 2015 to predict not yet observed transition frequencies in the $2\nu_1$ band of N_2H^+. The simulation assumes a Gaussian line profile and equal rotational and vibrational temperatures. Interestingly, already more than 7 % of the ions populate excited vibrational states at this temperature. The overlapping spectra differ only in the used value of the transition dipole moment. Since the transition strength depends on the square of the dipole moment, the impact of the difference is even larger than shown in Table 3.

3.2.3 *Production Reactions*

One of the dominant pathways of N_2H^+ production in hydrogen and nitrogen containing plasmas is the proton hop reaction

$$H_3{}^+ + N_2 \longrightarrow N_2H^+ + H_2,\ \Delta E = 0.74\,\mathrm{eV}, \tag{16}$$

also assumed to be the most important pathway in astrophysical environments. This reaction is an example of $H_3{}^+$ destruction reactions in most environments. Due to the relatively low proton affinity of H_2 most molecules readily take over one of the protons (or deuterons) earning the name universal proton donor for $H_3{}^+$. Again, we can calculate the available energy ΔE released in the reaction as the dif-

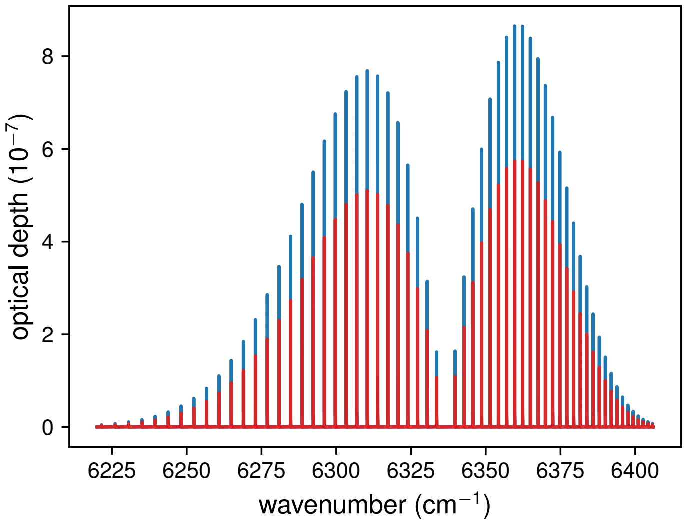

Figure 8. Simulated spectrum of the $2\nu_1$ band of N_2H^+. The lines are the sum of individual Gaussian line profiles at a temperature of 300 K. The rotational and vibrational temperatures are the same. The two overlapping spectra differ only in the value of the transition moment used, as listed in Table 3. A larger transition dipole moment leads to a larger transition strength.

ference of proton affinities[3]. This energy is still sufficient to populate several low-lying vibrational states of the molecule. A thermalisation mechanism in collisions with nitrogen is assumed to be quite effective since it can be thought of as the exchange of a proton between two nitrogen molecules.

In environments where H_2 and N_2 do not represent the majority of the gas, like in helium buffered discharges, we need to consider alternate pathways that are also driven by the differences in proton affinities and ionisation potentials. The energy released in different reactions are translated into distributions of vibrational excitation that, if not thermalised, can be a signature of the dominant production mechanism. In this thesis we consider three additional reactions next to the proton hop from ${H_3}^+$

$$
\begin{aligned}
{H_2}^+ + N_2 &\longrightarrow N_2H^+ + H, \ \Delta E = 2.45\,eV && (17a)\\
{N_2}^+ + H_2 &\longrightarrow N_2H^+ + H, \ \Delta E = 2.61\,eV && (17b)\\
HeH^+ + N_2 &\longrightarrow N_2H^+ + He, \ \Delta E = 3.28\,eV, && (17c)
\end{aligned}
$$

ordered by increasing energy differences. Compared to reaction 16, these reactions have access to a rather large amount of energy and have been suspected to be the source of observed highly excited vibrational states and respective excitation temperatures (Kabbadj et al. 1994).

---

[3] NIST Chemistry Webbook, `http://dx.doi.org/10.18434/T4D303`, (November 29, 2018).

3.2.4 *DR Rate Coefficients*

Research results on the DR of N_2H^+ has had a similar turbulent history as that of ${H_3}^+$. In this case a major role was played by the conflicting measurements of branching fractions, schematically represented as

$$N_2H^+ + e^- \longrightarrow \begin{cases} N_2 + H, \ \Delta E = 8.47\,eV \\ NH + N, \ \Delta E = 2.4\,eV. \end{cases} \tag{18}$$

The first storage ring measurements at CRYRING by Geppert et al. 2004 reported that as much as 64 % of the products end up as NH + N contrary to the early finding of afterglow experiments of Adams et al. 1991, who observed the dominance of the opposite channel. The findings of the two groups also differed in the observed temperature dependence of the thermal rate coefficient, but care must be taken when comparing the results. As we have learned, the storage ring temperature dependence is deducted from the collisional energy dependence and the possible influence of rotational temperatures should not be ignored. Follow-up afterglow experiments by Molek et al. 2007 with a different technique yet again were in agreement with the earlier results, raising questions about the storage ring findings and leading to the reassessment and reinvestigation of the experiments. Vigren et al. 2012 found that the DR of N_2H^+ is indeed dominated by the N_2 + H channel giving a branching fraction of roughly 93 %.

For a list of all experiments connected to the DR of N_2H^+ see the introduction given by Molek et al. 2007. Lawson, Osborne, and Adams 2011 extended these measurements and overview to ^{15}N and D containing isotopes. Here we only compare a chosen representative group of experiments. The observed thermal rate coefficients are plotted together in Figure 9.

From the storage ring side only the latest results are shown which are given as two power law dependences on the collisional temperature separately for low and high temperatures. Afterglow experiments can be also split into FALP and SA results. For the former, two sets of experiments are chosen from Smith and Adams 1984 and Poterya et al. 2005, the works of co-workers of N. G. Adams. Based on the earlier measurements, a temperature dependence of $\sim T^{-0.92}$ was suggested from the rate coefficient values measured at two temperatures, 'typical' for the combination of both direct and indirect mechanisms. The subsequent FALP experiments found a less prominent temperature dependence. The observed rate coefficient values in the 200 K to 500 K range are quoted to be constant in the range of uncertainties. Again on the contrary, the only experiment where the ions were spectroscopically characterised, conducted by Amano 1990, suggests a similar temperature dependence as Smith and Adams 1984 but with absolute values roughly four times larger. The last group to enter the comparison is Fonseca dos Santos et al. 2014 who theoretically calculated DR

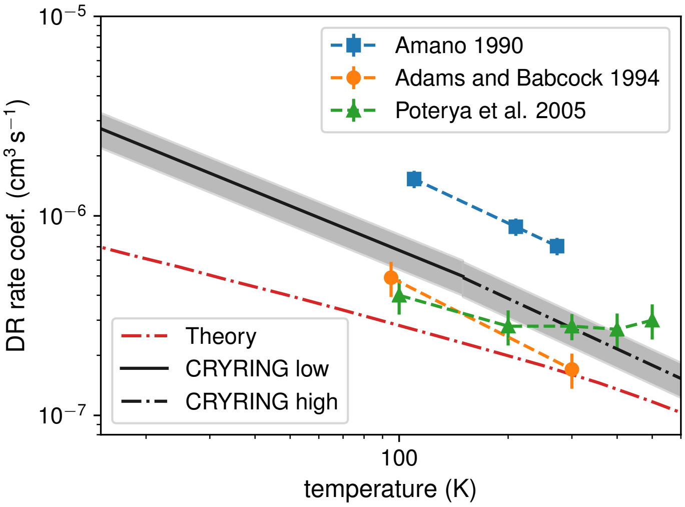

Figure 9. State of the art experimental and theoretical DR rate coefficients of N_2H^+. The data are grouped by techniques by which they were acquired. Symbols denote values measured in different afterglow experiments by Amano 1990; Poterya et al. 2005; Smith and Adams 1984, the dashed lines connecting these data values are for eye-guiding only. The dot-dashed line represents the latest *ab initio* theoretical calculations of Fonseca dos Santos et al. 2014. The CRYRING data of Vigren et al. 2012 are plotted by two lines that reproduce the two power low expressions given in the publication.

cross sections and thermal rate coefficients based on *ab initio* methods. An important part of their assumptions is that the rotational motion of the molecular target in the calculations is neglected. They justify this assumption based on the relatively high rotational temperature of the ions in the storage ring experiments that should average out the rotational resonances. This structureless cross section is not reproduced here but gives a qualitatively and quantitatively different energy dependence at low collision energies. Whether such an effect is caused by the rotational dependence of the cross section or the assumptions of the theory is yet to be seen. Nonetheless, so far theory gives the lowest values for the thermal rate coefficient.

Another appealing side of the DR of N_2H^+ for experimentalists is that the N_2 products can end up in several electronically and vibrationally excited states. Adams and Babcock 1994 observed the emission of radiation from the radiative decay of such states and also gives a scheme of energetically accessible levels from the ground vibrational state of N_2H^+. By observing the distribution of vibrationally excited states in one of the electronic states they concluded that for certain experimental conditions the contribution of vibrationally excited states of N_2H^+ was not significant, since some of the levels are only accessible from excited states. Given that suitable electronic transitions between electronically excited states of N_2 can be found, these experiments could be potentially enhanced by observing the time dependent absorption of target states.

In summary, there are still discrepancies about the DR of N_2H^+ worthy of investigation that could potentially have an impact on astrochemical models. The ultimate goal of contemporary research is to revise the afterglow data and to contribute with accurate values of thermal rate coefficients to modelling efforts. this thesis focuses on the spectroscopic characterisation of the ions of interest by seeking transitions suitable for rotational temperature measurements and also for the investigation of DR rate coefficients.

Part II

EARLY STAGES

Where we first introduce the experimental techniques and data analysis encountered in this thesis and describe some of the experiments where they have been employed.

4

EXPERIMENTAL TECHNIQUES

This chapter's purpose is both to give an overview of the experimental methods used during the course of this thesis, including technical details and formulas used in the data analysis, and a short historical comparison and review about the development in related instrumentation. Direct comparison between merged-beams and afterglow techniques without the necessary experience and involvement is rather impossible. Both approaches present unique challenges. Thanks to an internship spent at the Max-Planck-Institut für Kernphysik (MPIK), I will attempt a description of both. Naturally, the amount of pages dedicated to each technique should reflect the time and work devoted to each during the course of my work. Since the structure of the work splits up the description of the involved experimental instruments counting the length of each section is not meant to be representative.

4.1 THE MERGED-BEAM TECHNIQUE

Beam experiments have been present in experimental physics since the beginning of modern day physics of the 20th century. Such historical examples are J. J. Thompson's 'cathode rays', later renamed to electrons, or Rutherford's alpha particles passing through a thin gold film. Today's experimental setups have grown both in size and complexity spanning between countries and sustaining international collaborations such as the Large Hadron Collider at CERN. For the purpose of DR research we will settle somewhere between in size at so called storage rings.

Historically, storage rings were designed for high energy physics but later found application also in atomic and molecular physics at several facilities with devices as TSR (Baumann et al. 1988), ASTRID (Stensgaard 1988) and CRYRING (Abrahamsson et al. 1993). These were magnetic storage rings operated in the MeV range with the maximum ion mass limited by the bending magnets. Equipped with an electron target for both phase space cooling of the ion beam and merged-beams experiments, these devices played a crucial role in the advancement of Dissociative Recombination (DR) research.

To overcome the mass limitation, fully electrostatic devices have been constructed and put into operation in the recent years, beginning with the pioneering work on ELISA (Møller 1997). This is the very first electrostatic storage ring constructed in a unique racetrack layout that was later adapted in several device designs. The first of these devices that has also been equipped with an electron target had been constructed at KEK and demonstrated storage and dissociative recombination of large biomolecules (Tanabe, Noda, and Syresin 2004). While it is generally true that electrostatic devices have no mass limitation, they are also operated in the keV energy range where scattering of the ion beam on residual gas particles can be a limiting factor for the beam lifetime. Cooling down the storage ring chambers to cryogenic temperatures enhances orders of magnitude the vacuum conditions and also reduces the temperature of the thermal radiation field. At these conditions molecular ions can radiatively relax to their lowest rotational states and large clusters can be stored that otherwise would be destroyed by room temperature radiation. Up to now there have been three cryogenic devices constructed. They are either operational or in an early experimental phase. These are: DESIREE, a double racetrack layout ring designed especially for cation-anion interactions (Thomas et al. 2011) and RICE, the smallest of the three with a 2.9 m circumference (Nakano et al. 2017). Thanks to their relatively small size both devices deploy liquid-helium-free cryocoolers to achieve chamber temperatures around 10 K. And last but not least comes the Cryogenic Storage Ring (CSR) at MPIK, the main topic of the upcoming section.

4.1.1 *The Cryogenic Storage Ring*

CSR is an ambitious project both in size and purpose. It is designed to serve as an experimental platform for several research areas in atomic, molecular and cluster physics. Its lattice is optimised for meter long straight sections dedicated to the following experimental setups: ion-neutral experiments in both merged- and crossed-beams configurations, ion-laser interaction regions in similar configurations and, most relevant for this thesis, an electron target for both phase space cooling of the ion beam and electron-ion interaction studies. One of the first electron-ion interaction processes proposed to be studied is DR. In this section we are going to highlight the parts of CSR relevant for this research field and how DR cross sections are measured utilising this complex machine. For more technical details see the report on the commissioning by the CSR collaboration (von Hahn et al. 2016).

As mentioned above, the CSR layout was designed to facilitate four straight sections for experimental setups, each 2.6 m long, thus achieving its quadratic shape with a 35 m circumference. In each corner the ion beam is bent by two pairs of 6° and 39° deflectors accompanied by quadrupole focusing electrodes. The purpose of the deflector splitting is to allow the collection of neutral particles after the straight sections and the analysis of charged fragments different from that of the parent ion beam. This setup also allows for single turn injection of the ion beam by fast switching of the 6° deflector next to the injection beamline. The injected beam can have kinetic energies up to 300 keV per charge unit.

Similar to any cryogenic device the vacuum system of CSR consists of an inner experimental vacuum chamber where the ion beam circulates and an outer insulating vacuum chamber to minimise conductive thermal losses. The experimental chamber can reach temperatures below 10 K and is surrounded by two layers of thermal radiation shields all housed in the insulation chamber. This cryogenic system is cooled by a closed cycle liquid helium refrigerator. So far these were fairly standard methods of cryogenic instrumentation. The unique demands of a cryogenic storage ring come in the form of the alignment of the ion optics system which is independently supported from both the experimental and insulation vacuum chambers. This way thermal shrinking does not affect the alignment. Cryogenic operation has also a positive effect on vacuum conditions. With the support of cryosorption pumps, pressures (room temperature equivalent) below 10^{-11} Pa can be achieved.

The main experimental reason for cooling down an electrostatic storage ring is not just the improvement in beam lifetime but also the possibility of radiative rotational de-excitation of the molecular ions in the low temperature thermal radiation field of the chambers. First experiments at CSR followed this cooling process during the storage of both diatomic cations and anions. Pulsed laser experiments with CH^+ ions revealed Feshbach-type near-threshold photodissociation resonances comparable with theoretical predictions allowing to extract time-dependent rotational level populations (O'Connor et al. 2016). Photodetachment of OH^- ions confirmed the low temperature of the thermal radiation field in cryogenic operation where relative cross sections, rotational radiative lifetimes and the dipole moment of the ion were determined (Meyer et al. 2017). Experiments with photodetachment of OH^- were performed at DESIREE showing similar cooling behaviour (Schmidt et al. 2017).

Turning our gaze to future prospects, successful electron-ion interaction experiments can be simplified to three main ingredients. First of them is the full control over the stored ion beam and extraction of its properties using diagnostic tools. One of the straight sections of CSR is designated to non-destructive diagnostic methods. These measure the ion beam current which is necessary for the determination of absolute cross sections. Position pickups can be used to determine the shift of the closed orbit of the beam ensuring good overlap in the experimental sections.

Next in turn are particle detectors whose purpose is to gather the neutral or charged fragments of electron-ion interactions. Although the products of DR are by definition neutral, at higher interaction energies dissociation of the molecular ions is also a probable, sometimes a dominant process. Neutral imaging and coincidence detection can eliminate this uncertainty. Furthermore, measurement of the neutral fragment distance distribution leads to product state identification and gives further information about the nature of the breakup process. A mass sensitive detector is currently in development for detection of heavy fragments and large molecules (Gamer et al. 2016). A movable particle counter ensures the detection of charge states differing from the state of the parent beam and other charged fragments (Krantz et al. 2017), for example in atomic recombination of highly charged ions.

At the heart of the experiments lies the electron target serving two purposes. It is a source of a cold electron beam for both phase space cooling of the ion beam and serving as an interaction partner. A step by step examination of each part of the CSR electron cooler will shed light on the complexity of this device.

First of all a source of cold electrons is needed. As it turns out, photo-electron sources are both stable and can provide continuous electron currents of several tens of microamperes. In a basic setup a photo-cathode is illuminated by laser radiation and emits electrons which are extracted by an electrostatic field. In the right electrode configuration, it is possible to achieve a flat-top shape spatial profile of the beam and an electron energy distribution that is different from that of the thermal distribution given by the cathode temperature. In the actual setup the electron source is sitting in the high field region of a guiding magnetic field. When talking about electron energy or velocity distributions, we have to distinguish between the components that are parallel and perpendicular to the magnetic field lines. It is the longitudinal energy distribution that is affected by the electrostatic acceleration during extraction and the space charge of the electrons in front of the photo-cathode. It would take another section to explain the working principle of similar cold electron sources, for details see, e. g., (Shornikov et al. 2014).

In the next step the electrons are adiabatically transported to a lower magnetic field which results in adiabatic expansion of the beam area and also the transfer of the transverse electron energy into the longitudinal motion. We assume Maxwellian distributions in both longitudinal and transverse directions. Even after this adiabatic expansion the longitudinal temperature is orders of magnitude lower than the transverse. The CSR electron cooler is designed to have two regions of adiabatic expansion before the merging section. Due to technical reasons, the electron gun (highest magnetic fields) and the photo-cathode preparation chamber are both situated at room temperature. The first expansion is taken place in this room temperature part of the cooler where it is easier to maintain higher currents using conventional water cooled solenoids. Up to now, this description could be applied to any electron cooler setup used all over the storage rings. It is the next step where the uniqueness of the CSR electron cooler is revealed, transfer of the electron beam to the cryogenic experimental chamber.

Technically, the experimental and the electron cooler vacuum chambers are part of one, almost continuous vacuum system separated by gate valves and the transition regions from room temperature to cryogenic conditions. In this construction we are faced by the thermal decoupling of the vacuum chambers at the same time where we require to maintain a continuous magnetic guiding field. The solution for this problem came from years of design and tests done by numerous experts. Thermal decoupling is realised in a fairly standard way, by vacuum bellows. The real complications arise at the meeting point of the room temperature and the cryogenic magnets. This region has to be already surrounded by a thermal radiation shield. High Temperature Superconductor (HTS) windings were used in the construction of all cryogenic magnets to minimise the heat load onto the cooling system. The meeting point of the HTS and room temperature magnets was designed for optimal magnetic field homogeneity and heat load distribution.

The merging and interaction section itself is a collection of various HTS magnets in all shapes and types that surround the experimental chamber. Next to the standard guiding field, we have additional correction coils for the ion beam and several coils to manipulate the electron beam position in vertical and horizontal direction, and the interaction angle of the merged-beams. The second adiabatic expansion of the electron beam takes place in this cryogenic environment. Mechanical scrapers are positioned at both ends of the interaction region that help find the optimal overlap of the beams.

And finally we have arrived at our destination: phase space cooling of an ion beam with a cold, velocity matched electron beam. At zero relative beam velocities, Coulombic interactions between a stored ion beam and a continuously renewing electron beam prompt the ions with velocities differing from that of the electron beam to gradually loose energy in the co-moving electron frame of reference. This can also be thought as a friction force experienced by the ions. The injected ion beam occupies a certain volume in the phase space that characterises the ion velocity spread with respect to the so called synchronous particle. Electrostatic fields cannot change the volume only the shape of the occupied phase space. On the other hand, a friction force can lead to the shrinking of the occupied volume.

In storage ring terminology, the kinetic energy difference of the two beams is called the detuning energy. Basically, there are two options how to control the electron beam energy. Either set the final value in the acceleration region of the gun and have the rest of the setup at a common ground potential or install a so called drift tube in the interaction region. A drift tube is a simple cylindrical electrode with a homogeneous potential in its inner volume. Charged particles entering it exchange part of their kinetic energy with the potential energy of the field inside the electrodes. While the first option is simpler to realise, only the second method enables to achieve electron beam energies as low as 1 eV in the lab frame of reference. A similar value is needed to electron cool a 300 keV ion beam of mass 160 u.

Phase space cooling of the ions can be detected several ways. The most straightforward method is to observe the Schottky noise spectra in the so called bunched mode. CSR is equipped with both a Radio Frequency (RF) bunching electrode and a Schottky pick-up unit. Continuous RF excitation at a harmonic of the beam revolution frequency results in a periodic time structure along the longitudinal direction of the ion beam. The width of these bunches is determined by the amplitude of the bunching field and the longitudinal momentum spread of the ions. Electron cooling manifests as the shrinking of the bunch width due to the reduction of the momentum spread. We can record this temporal evolution in the time domain as waveforms or we can use a spectrum analyser and observe the effects in the frequency domain. The latter approach is based on the following principle. A Schottky noise spectrum of a coasting beam consists of several peaks at the harmonics of the revolution frequency, each containing the same power. During bunching, this spectrum is altered by the RF frequency and the power at each harmonic depends on the bunch width. Recording the temporal evolution at one of the RF harmonics we can observe longitudinal electron cooling. An alternative method is to use neutral imaging and measure the centre of weight distribution of the ion beam revealing translational cooling. This is a more time consuming method due to particle counting statistics and coincidence detection efficiency.

Due to the sensitivity of electron cooling to relative velocity differences, velocity-matching can be achieved to a high precision. Slight detuning of the electron energy can result in effects such as dragging of the ion beam, the friction force witnessed by the ions strongly changes the ion beam velocity. The nominal interaction energy can be as low as a few microelectronvolt, the limiting factor in energy resolution is the transverse electron temperature. At this point we should also address the absolute kinetic energy calibration. Both the contact potential of the photo-cathode and the space charge of the electron beam affect the final kinetic energy when accelerating or decelerating the electron beam. The beam energy has to be independently determined or its approximate value corrected for the named effects. Basic calculations rely on the accurate value of the electron beam current.

Exiting the interaction region the electrons are guided out of the experimental vacuum chamber into the electron collector. Its geometry is similar to the gun configuration with a difference in the final magnetic field. Further diagnostic tools are located here that can be used to measure the spatial profile of the electron beam or the longitudinal energy distribution with a retarding field analyser.

This summary and overview of how electron-ion interactions are studied at CSR is just an extract from the knowledge and work dedicated to this project. Years of design and several doctoral theses are behind the contemporary state of the operational CSR electron cooler, not to mention the undergraduate students taking share of the work. More technical details and extensive theoretical explanations can be found in the theses of Krantz 2009; Vogel 2016 and Becker 2016. The first operation of the electron cooler during the 2017 and 2018 experimental campaigns will be presented in the doctoral theses of Patrick Wilhelm and Sunny Saurabh, focusing on electron cooling and DR experiments, respectively.

4.2 AFTERGLOW TECHNIQUES

The history of afterglow techniques can be traced back to the rapid development of microwave techniques and fast electronics in the period following the Second World War. Stationary Afterglow (SA) conquered the experimental research of DR by providing an environment of thermally excited ions (both for vibrational and rotational excitation) and cold electrons that is not limited to small molecules. For a thorough historical review of the early developments see Biondi 2003. A basic description of the simplicity of this configuration is as follows. A discharge is ignited in a mixture of gases where electrons ionise the gas and the reactants form the desired species. When the active discharge is terminated the afterglow sets in. It is a period of rapid relaxation and cooling of the electrons in elastic collision with the buffer gas. Once ion-neutral interactions reach equilibrium, thermal DR rate coefficients can be inferred from the measured time decay of the electron or ion number density, given that the ion composition is known. Diagnostic tools frequently used in this setup were Langmuir probes, mass spectrometry, optical methods and microwave techniques.

The next step in the evolution of the afterglow instrumentation came with the development of the first Flowing Afterglow (FA) apparatus for studies of ion-molecule reactions by Ferguson, Fehsenfeld, and Schmeltekopf 1969. An ingenious solution to the separation of the ion source and the measurement region. A substantial flow of the buffer gas flowing through a drift or flow tube (with and without electric field, respectively) transforms the temporal evolution into a spatial one along the tube. Soon this configuration was adapted to electron-ion recombination experiments by Mahdavi, Hasted, and Nakshbandi 1971. Deploying a similar set of diagnostic tools, this technique developed into specialised instruments like the widely used Selected Ion Flow Tube (SIFT) for ion-neutral reactions (Španěl and Smith 2017) and the Flowing Afterglow with Langmuir Probe (FALP) for electron-ion interactions (Alge, Adams, and Smith 1983).

The laboratory where the work described in this thesis was conducted has a long history with various designs of afterglow instruments. The developments have always been pointing in the direction of below room temperatures. The latest advancements in afterglow instrumentation was constructed and put into operation during the course of this thesis. Up to this point, the record holder in lowest temperature afterglow plasma in our laboratory was the apparatus bearing the name cryo-FALP II. Its flow tube is cooled by a single-stage cryo-cooler and lacks a thermal shield. Experimental temperatures can be reached around 50 K in this setup (Dohnal et al. 2013). This limitation is also due to the large amount of flowing gas required for this setup. Concerning the design of our latest apparatus, a different approach was chosen. A SA configuration can easily satisfy the ion number density requirement that needs to be high enough for laser absorption spectroscopy. Having in mind the need for spectroscopic characterisation of the recombining ions, a new cryogenic SA instrument was designed utilising years of experience with its ancestor: Stationary Afterglow with Cavity Ring-down Spectroscopy (SA-CRDS). The majority of the scientific experiments presented in this thesis were conducted on the SA-CRDS instrument. In the following section a summarising description is given of this apparatus leaving the construction and commissioning of our novel instrument for its own Chapter 7.

4.2.1 *Stationary Afterglow with CRDS*

As the name indicates, the described apparatus combines the SA technique with a sensitive laser absorption spectrometer. The main purpose of the employed diagnostic method is to track individual rotational states of the recombining ions *in situ* by determining the time dependent ion number density and relative populations of several states. How this diagnostic method works and what else we can learn from the measured absorption spectra is explained in Section 4.3. In this part of the text we focus on the technical details of the SA part. Detailed description of the original apparatus and some additional modifications can be found in the paper by Macko et al. 2004 and doctoral thesis of Rubovič 2014. Its schematic representation is shown in Figure 10.

Starting at the middle of the apparatus the working gas is contained in a fused silica discharge tube that is located inside a rectangular microwave resonator. Both ends of the discharge tube are connected to compact stainless steel Ultra High Vacuum (UHV) elements which lead to the mirror holders of the spectrometer. The mirrors are located inside the experimental vacuum chambers. The whole system is modular in nature, the glass to metal transitions are not fixed but sealed by elastomer O-rings. The whole system can be pumped by a turbomolecular pump to reach vacuum pressures on the 10^{-5} Pa level.

The majority of the working gas is the so called buffer gas. Its purpose is to cool the electrons in elastic collisions and slow down the

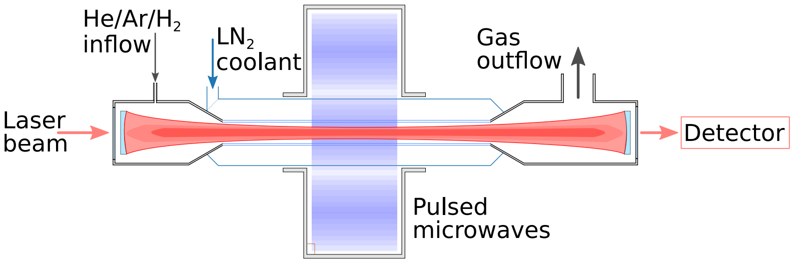

Figure 10. Schematic representation of the Stationary Afterglow apparatus with Cavity Ring-down Spectroscopy. In this example a gas mixture of He/Ar/H_2 is continuously flowing through the microwave region. The discharge tube is cooled by liquid nitrogen in its full length exceeding the discharge region. A near-infrared laser beam excites the optical cavity and interacts with the ions of interest. The repetitive microwave pulses serve as the time reference for temporally resolved measurements. See text for further details.

diffusion of charged particles towards the walls of the container. The overall pressure during the experiments is in the range of 10^2 Pa to 10^4 Pa. Depending on the desired species to be studied, further reactant gases are added usually in the $10^{13}\,\mathrm{cm^{-3}}$ to $10^{15}\,\mathrm{cm^{-3}}$ number density range. A common practice in afterglow techniques is to use helium as the buffer gas with an admixture of argon similar to the reactant number densities. Helium is the most effective electron coolant and argon helps to eliminate helium metastable states that are populated in the active discharge. Although the microwave field excited discharge region is stationary in space, the working gas itself is flowing through this region to maintain gas purity. With the support of a well prepared gas handling and purifying system, impurities on the ppm level can be regularly achieved even at room temperature.

The discharge tube is additionally surrounded by another glass insulation tube that can be closed off from both ends to form a cooling bath. By using liquid nitrogen or pre-cooled nitrogen vapours, the temperature of the discharge tube can be regulated in the 77 K to 300 K range.

The timing electronics system consists of a pair of pulse generators, one for the timing and control of the microwave source and one for the synchronisation of the discharge timing with the data acquisition system of the absorption spectrometer. The repetitive microwave pulses are supplied by a modified magnetron type power source. The termination of the input microwave power is achieved by switching off the power supply of the magnetron with a fast high voltage switch.

4.2.2 *Afterglow Analysis*

Recombination rate coefficients in afterglow experiments are extracted from the measured temporally resolved ion or electron number density.

There are quite a few assumptions behind this method. Here we summarise and derive the formulas necessary for this analysis.

The most important assumption is the quasi-neutrality of plasmas. This is one of the main defining characters of plasmas and so we can safely assume this for the bulk of the gas, carefully avoiding the sheath region. From this it is evident how we can interlink the measurement of ion and electron number densities. In plasmas containing only singly charged cations the electron number density equals the overall ion number density. When there is no single dominant species we have to track all the major constituents of the ion chemistry.

Up next we assume that the diffusion of charge carriers is governed by ambipolar diffusion, a typical mode for non-magnetised plasmas. This assumption is roughly valid for plasma parameters in the same region as quasi-neutrality, although we have to be careful about not to go too low with the charged particle number densities.

And last there is the assumption that the ions and electrons posses Maxwellian velocity distributions and collisions are governed by thermal rate coefficients. This is the part where experimentalists have to be the most careful. Rotational and vibrational excitation of the ions can be traced using spectroscopic methods. Same can be said about the ion translational temperature T_i. But the case of the electrons is severalfold more complicated. For afterglow plasmas, where we expect the electron temperature T_e to be close to that of the buffer gas temperature, direct measurement of the electron temperature is limited by physical phenomena. Taking a step back and examining how thermal rate coefficients are related to the underlying cross sections we can easily derive that for the case of $T_e < T_i$ the thermal rate coefficients reflect only the electron temperature to a high precision. For now, we will work with T_e and T_i to derive useful formulas. The question of the electron temperature is examined in an upcoming subsection.

Our master equation for both ion n_i and electron n_e number densities is the time averaged Boltzmann equation. As an example, we will assemble one for a given ionic species including three reactions: electron-ion recombination, reaction of the ions with species X and ambipolar diffusion

$$\frac{\partial n_i(\mathbf{r}, t)}{\partial t} = -\alpha_{\mathrm{eff}} n_e n_i - k_X [X] n_i + \nabla \cdot (D_A \nabla n_i) . \tag{19}$$

In the first part α_{eff} stands for an effective recombination rate coefficient that can be the result of, e. g., a possible pressure dependence, as observed in certain experiments, or rotationally averaged rate coefficients with the ions having a non-thermal rotational distribution. An effective rate coefficient treats these effects as stationary in time. The next constituent can be thought of as a parasitic reaction with impurities of number density [X] characterised by a rate coefficient k_X. These impurities turn the initial ions into a different species by direct charge transfer or in ion-molecular reactions. If the amount of created ions is small compared to the initial species, we can treat this as a perturbation, as assumed in the following. The last element containing spatial derivative of the ion number density accounts for ambipolar diffusion with a coefficient D_A.

Careful analysis of this differential equation would reveal that its solution has no analytical form but certain approximate formulas can be derived that are helpful for experimental applications. This can be done on a step by step basis. Considering the purely recombination case and also assuming $n_i \cong n_e$ (dropping the index) leads to the solution

$$n(t) = \frac{n_0}{1 + \alpha_{\text{eff}} n_0 t}, \tag{20}$$

where n_0 is the plasma number density at $t = t_0$. This solution is naturally independent of the spatial coordinates. The reciprocal number density versus time plot, a historical technique, is a straight line in recombination dominated environments.

Focusing on the next part of the equation with a typical form of n/τ_X, where $1/\tau_X = k_X [X]$ in this particular case, leads to a frequently used exponential solution

$$n(t) = n_0 \exp\left(-(t - t_0)/\tau_X\right), \tag{21}$$

where we assumed that [X] is constant in time. In other words, this is a typical time dependence for ion-molecular reactions where the neutral number density is orders of magnitude larger than the ion number density or has a constant and relatively fast source.

The combination of these two right hand side parts still leads to an analytical solution

$$n(t) = \frac{n_0 \exp\left(-(t - t_0)/\tau_X\right)}{1 + \alpha_{\text{eff}} n_0 \tau_X \left[1 - \exp\left(-(t - t_0)/\tau_X\right)\right]}. \tag{22}$$

Shifting our attention to the last right hand side part of Equation 19 we see that the spatial and temporal derivatives are separated indicating that the solution can be found in separate spatial and temporal domains. Assuming that the time dependent part has the form of Equation 21 we obtain an ordinary differential equation for the spatial part

$$D_A \nabla^2 n(\mathbf{r}) + n(\mathbf{r})/\tau_A = 0. \tag{23}$$

The transformation of this equation to cylindrical symmetry, which is the case of the plasma containers considered in this thesis, leads to

$$D_A \left[\frac{1}{r}\frac{\partial}{\partial r}\left(r\frac{\partial n}{\partial r}\right) + \frac{\partial^2 n}{\partial z^2}\right] + n(r,z)/\tau_A = 0. \tag{24}$$

Assuming absorbing boundary conditions, i. e., charged particle number densities equal to approximately zero at the walls of the container

($z = \pm L/2$ and $r = R$), we can obtain an analytical solution for the lowest mode of ambipolar diffusion

$$n\left(r, z, t\right) = n_0 \exp\left(-\left(t - t_0\right)/\tau_A\right) \cos\left(\frac{\pi z}{L}\right) J_0\left(\frac{J_0^r r}{R}\right), \tag{25}$$

where r and z are the radial and longitudinal coordinates, respectively, L is the length and R is the radius of the cylindrical container, and $J_0(x)$ and J_0^r are the zero order Bessel function of the first kind and its first root, respectively. Substituting this solution back into Equation 24 we finally obtain the relation between the container size, diffusion coefficient and time dependent part of the solution

$$1/\tau_A = \frac{D_A}{\Lambda^2} \tag{26}$$

with the characteristic spatial scale defined as

$$\frac{1}{\Lambda^2} \equiv \left(\frac{\pi}{L}\right)^2 + \left(\frac{J_0^r}{R}\right)^2. \tag{27}$$

As we can see, even in the case of one order of magnitude larger longitudinal than radial spatial scale the diffusion time scale is fully governed by the radial size. In a practical case when the particle source, i. e., a discharge, is localised in a relatively small part of a cylindrical container the longitudinal shape will not reach the exact ground mode of a closed container. In this case termination of the discharge starts a temporal evolution in the longitudinal direction. The solution can be found by propagating the initial shape at the time of discharge termination. An analytical solution can be expressed as an infinite sum of a cosine series with coefficients determined from the series expansion of the initial condition into the cosine base functions.

The set of analytical tools at our disposal ends here. If we can assume that recombination is a small perturbation in Equation 19, it is possible to find an approximate solution by assuming a spatial distribution of charged particles in the form of the ground diffusion mode. The higher modes by definition decay faster. Following an initial period the diffusion decay rate will be governed by the ground radial mode. The exponential part time constant will consist of a sum of the individual parts, as in

$$1/\tau = 1/\tau_A + 1/\tau_X. \tag{28}$$

To find out what happens in recombination dominated or intermediate cases we turn to computer simulations and numerically solve the set of non-linear equations. From the functional dependence of recombination we expect that it affects regions of higher number density and leads to a flattening of the spatial distribution. A 2D plasma model in cylindrical geometry is the topic of Section 8.1.

4.2.3 *Ambipolar Diffusion*

A few more practical formulas regarding ambipolar diffusion can come handy in afterglow analysis and also in discharge modelling. First of all we need to define the charged particle mobility and the diffusion coefficient as

$$\mu \equiv |q| / m\nu \tag{29}$$

and

$$D \equiv k_B T / m\nu, \tag{30}$$

where q is the charge, m the mass, T the temperature and ν the collision frequency of the charged particles.

Ambipolar diffusion occurs in order to maintain quasi-neutrality in plasmas. Due to the differences in thermal velocities and diffusion coefficients electrons would escape the plasma generating a positive space charge. The ions in response generate a so called ambipolar electric field that slows down the electron diffusion. The resulting condition of equal charged particles fluxes leads to a common diffusion coefficient

$$D_A = \frac{\mu_i D_e + \mu_e D_i}{\mu_i + \mu_e}. \tag{31}$$

Assuming that $\mu_i \ll \mu_e$ and substituting the definitions of D and μ we can estimate the value of the ambipolar diffusion coefficient

$$D_A \approx \left(1 + \frac{T_e}{T_i}\right) D_i. \tag{32}$$

The practical usefulness of this result is the dependence on both electron and ion temperatures. It can be used as a probe of temperature in thermal equilibrium conditions. Alternatively, if we have another source of information on the ion temperature, it can serve as a verification of the electron thermalisation.

4.2.4 *Chemistry and Temperatures*

The desired ion composition in afterglow experiments is achieved by changing the reactant partial pressures and the overall pressure of the buffer gas. One of the most versatile methods that can track all ionic species is mass spectrometry. This is technically complicated to realise in SA setups where the goal is to reach relatively high ion number densities ($>10^{11}\,\mathrm{cm}^{-3}$). On the other hand, emission and absorption spectroscopy techniques allow to track excited species (both neutral and charged). A complete diagnostic system would need to cover a wide spectral range to include both atomic and molecular species, and even so symmetric diatomic molecules would pose a challenge in their ground states. Considering the technical difficulties the most feasible technique is to partly rely on measurements on FA setups with mass spectrometers and make use of available rate coefficient data on atomic and molecular processes to model plasma chemistry in the afterglow.

The discharge region itself is a much harder nut to crack. A self consistent model would need to include the time dependent electromagnetic field affected by the shielding effect of the charged particles, evolution of the electron velocity distribution function and all the energetically accessible excited states of most atoms and molecules. Collisional radiative models of this scale are challenging to realise in 0D (models considering only the time dependence). Promoting the model to a 2D cylindrical grid is even more difficult. Major issues with plasma modelling are a lack of complete, state to state cross section data on electron impact processes, unknown rates of surface interactions and computational complexity of a, by definition, iterative process. This thesis contributes to prospective ongoing modelling efforts by studying the discharge and afterglow 2D number density distributions of key charged species. Complementary efforts by students in our laboratory contribute to the construction of collisional radiative models.

And the answer to the question of what use of collisional radiative models have for the present afterglow studies of electron-ion recombination is the estimation of electron and excitation temperatures. Each cycle of a repetitive SA experiment is composed of an ionisation phase where the electrons are accelerated by an electric field and gradually transfer their energy to the atoms and molecules in form if ionisation and excitation. Meanwhile, ion chemistry is running parallel, the energy released in these reactions can be several electronvolt. Termination of the external electric field leads to the onset of rapid relaxation in the named temperatures and the parallel initiation of the recombination phase. Through each of these steps we can assign different values to the electron gas temperature (effective value in case the distribution function is not Maxwellian), to electronic, vibrational and rotational excitation temperatures, and even to the neutral gas and container wall temperatures.

A detailed assessment of electron kinetics in afterglow plasmas can be found, e. g., in Chapter 8 of Roučka 2012. Here we focus on the overview of relevant processes affecting temperature evolutions in low-temperature afterglow plasmas. For additional discussions concerning the ion and neutral temperatures see Dohnal et al. 2012.

The source of cooling power in our experiment are the gas container, i. e., the wall of the discharge tube, and the continually renewed buffer gas. As long as the heat absorbed in the discharge can be effectively transported and dissipated at the wall of the container, we can expect the neutral gas temperature to be equal to that of the wall. Further mechanisms that can potentially increase the wall temperature are surface reactions and the flux of excited particles. The magnitude of these heat input mechanisms is governed by the microwave power and the duration of the discharge.

In a first approximation microwave frequencies are too high for the heavier ions to follow and collisions with the buffer gas are assumed to govern the ion translational temperature. Same can be said about the rotational excitation distribution. Buffer gas collisions are assumed to be an effective coolant compared to electron impact excitation.

Vibrational excitation is a different story. Buffer gas collisions are less effective and radiative lifetimes are usually on the millisecond time scale. An exception is the case of symmetric diatomic molecules for which vibrationally excited states can be considered metastable. On of the relevant decay mechanisms is quenching by collisions with the container wall. The molecules in question need to be considered on a case by case basis.

The last category includes electronic states. Those which can decay by emission of photons do it on a sub-microsecond time scale and we only need to consider the role metastable states. We also assume that the afterglow plasma is optically transparent and the emitted radiation can escape it without re-absorption and scattering. Electronic metastable states have radiative lifetimes varying from milliseconds to several hours. Helium is known for its longest atomic excited-state lifetime of roughly 8000 s (Hodgman et al. 2009), the one that is also encountered in our experiments. Diffusion of these particles and subsequent quenching at the container wall is also an important mechanism. We have an additional process to consider. When the excitation energy of a metastable state is higher than the ionisation potential of another atom or molecule, the excitation energy can, in collisions, be transferred to a bound electron and ionise the colliding partner. This process is called Penning ionisation.

On purpose, the question of the electron temperature is left for the last part. Here we need to consider the balance between heating and cooling mechanisms. The dominant energy loss for electrons is momentum transfer in collisions with the buffer gas, referred to as elastic scattering. Due to the difference in electron and neutral masses, a relatively high number density of the buffer gas is needed to compensate for the reduced effectiveness of these collisions compared to particles with a closer mass to the neutrals. On the heating side of the balance equation, electrons are the most effective in transforming electronic or vibrational excitation of atoms and molecules back into kinetic energy in so called super-elastic collisions. These are the inverse process of electron impact excitation which are usually labelled as inelastic collisions. As long as there is a sufficient number of excited particles in the afterglow the electrons cannot reach the buffer gas temperature. This temperature difference is proportional to the number densities of excited species. Study of the population and decay rate of excited states in the afterglow is directly linked to the fundamental question: are electrons thermalised at the experimental conditions?

4.3 LASER-AIDED PLASMA DIAGNOSTICS

The primary diagnostic tool used in our SA experiments is a Continuous Wave Cavity Ring-down Spectrometer (cw-CRDS). It is a cavity enhanced laser absorption spectrometer that allows probing of the translational and rotational temperatures of molecular ions and most importantly determination of absolute ion number densities without any calibration requirements for the optical power detector. Technically speaking, it is the absolute line-of-sight integrated absorption coefficient, also called the optical depth, that can be measured using this tool. A theoretical and technical introduction to laser absorption spectroscopy and cavity enhanced methods is given in the following parts of this section.

4.3.1 *Laser Absorption Spectroscopy*

Laser absorption spectroscopy is the study of the interaction of an atom or molecule with a monochromatic electromagnetic wave which results in a transition from a lower to an upper level of the absorbing species. This method is restricted to low fields without any non-linear effects. In our case we are considering only single-photon absorption. Since some of the customary symbols used in absorption spectroscopy are overlapping with those used in other parts of this thesis, we are adopting the subscript ‘a’, as in absorption, to differentiate between the different physical quantities.

The mathematical description of this phenomenon can be found in many modern textbooks, in this introductory account we are adapting the definitions found in the book from Yariv 1997 and giving detailed derivations only when needed. A plane wave of intensity I and frequency ν propagating through a medium of atoms or molecules with an energy difference of $h\nu$ between some levels of the ensemble experiences change in its intensity

$$\frac{\partial I\left(\nu,z\right)}{\partial z}=-\alpha_a\left(\nu,z\right)I\left(\nu,z\right),\tag{33}$$

where z is the direction of the wave propagation and $\alpha_a\left(\nu,z\right)$ has been explicitly defined as the absorption coefficient. Dropping the minus sign in Equation 33 we would arrive to a general form for both amplification and attenuation of the wave. At standard conditions, i. e., where the population of the levels is described by the Boltzmann distribution, the propagating wave is always attenuated. Non-standard conditions refer to population inversion, also observable in active discharges. Solving Equation 33 in a non-homogeneous environment leads to an integral form

$$I\left(\nu, z\right) = I_0 \exp\left[-\int_{z_0}^{z} \alpha_a\left(\nu, z'\right) dz'\right], \tag{34}$$

where I_0 is the wave intensity at z_0. This form is of practical importance when performing advanced data analysis. For the purpose of simplicity and reduction in space for further derivations we should also derive the solution in a homogeneous medium

$$I\left(\nu, z\right) = I_0 \exp\left[-\alpha_a\left(\nu\right)\left(z - z_0\right)\right]. \tag{35}$$

The origin of the absorption coefficient and its frequency dependence is both governed by quantum mechanics and other statistical physical phenomena. We can define additional useful physical quantities such as the photo-absorption cross section $\sigma_a\left(\nu\right)$

$$\alpha_a\left(\nu\right) = [X]\,\sigma_a\left(\nu\right), \tag{36}$$

where [X] is the volume number density of species X whose level population is governed by the Boltzmann distribution. In the literature this quantity is sometimes identified as the absorption coefficient although it does have the units of a cross section. The reader is advised to check the units involved when comparing textbook definitions. Dividing up the photo-absorption cross section into purely frequency and species dependent parts we get

$$\sigma_a\left(\nu\right) = S_a f\left(\nu\right), \tag{37}$$

where S_a is the spectral line intensity and $f\left(\nu\right)$ is the normalised spectral line shape function. Following subsections are dedicated to both of these quantities. In the remaining part we focus on definitions frequent in absorption spectroscopy like the dimensionless optical depth τ_a (previously introduced as the line-of-sight integrated absorption coefficient)

$$\tau_a\left(\nu, z\right) = \ln\left[\frac{I_0}{I\left(\nu, z\right)}\right] = \int_{z_0}^{z} \sigma_a\left(\nu, z'\right)[X]\left(z'\right) dz', \tag{38}$$

also related to the spectral absorbance A_a

$$A_a\left(\nu, z\right) = \tau_a\left(\nu, z\right) / \ln 10. \tag{39}$$

Here we reintroduced the possibility of a non-homogeneous volume number density and photo-absorption cross section along the propagation path. If the absorption properties of the medium are homogeneous along the path of light propagation, this integral represents the column number density which is the actual physical quantity determined in most experiments. This way we do not need to introduce further assumptions about the absorption path. These definitions are of practical use when considering applications like single- or multi-pass absorption experiments.

Laser absorption spectroscopy has a few more customary conventions concerning units and quantities used. Some authors may prefer the usage of angular instead of linear frequency which are related only by a simple factor $\omega = 2\pi\nu$. Next in line are the units. Hertz is a simple enough unit, mostly used to characterise optical instruments, but not especially useful when considering most infrared or higher energy transitions. The spectroscopist's choice of quantity is the wavenumber $\tilde{\nu} = \nu/c$ in units of cm^{-1}, where c is the speed of light in vacuum. This unit is customarily used to express the energy levels of a quantum system since the difference in energies (also in cm^{-1}) between two levels equals the transition wavenumber. As a powerful practical system, it is also adopted in this thesis.

4.3.2 *Spectral Line Intensity*

The physical origin of the intensity of transitions between different states of molecules and atoms have been explored in Chapter 2. Here we focus on practical formulas that help us extract useful plasma parameters out of measured absorption spectra. First of all, we need a few more statistical definitions to be able to work with the already mentioned Boltzmann distribution.

Maxwell-Boltzmann statistics governs the occupation of states of distinguishable but identical particles, such as a gas of ions or neutral molecules where temperatures are high enough so that we do not need to consider quantum effects. Energy levels are considered to be static in this case and same for all particles. We are going to further assume that there is a fixed number of particles N in the ensemble in equilibrium at temperature T. The probability of finding n_s number of particles having energy E_s is expressed by

$$P_s = \frac{g_s}{Q\left(T\right)} \exp\left(\frac{-E_s}{k_B T}\right), \tag{40}$$

where g_s is the multiplicity of the energy level and $Q\left(T\right)$ is the partition sum of all states. Multiplicity (also called statistical weight) of an energy level is the number of states with identical energies. Such a level is identified as degenerate. Multiplicity can be also used when levels are not resolved in the experiment. Caution must be exercised since statistics demands that all the states are included in the partition sum, not just the different energy levels

$$Q\left(T\right) = \sum_s g_s \exp\left(\frac{-E_s}{k_B T}\right). \tag{41}$$

The next step towards a formula of spectral line intensity would involve the quantum theory of the electromagnetic radiation. Since most of the Einstein coefficients are not used in this thesis, the various definitions of the energy density of the field and similar quantities are skipped. These can be also found in the textbook from Yariv 1997. The final formula for the integral intensity of an absorption line of a transition between initial lower energy level E_i and final higher energy level E_j for a medium in thermal equilibrium is

$$S_{ij}\left(T\right) = \frac{g_j}{Q\left(T\right)} \frac{c}{8\pi {\nu_0}^2} A_{ij} \left[\exp\left(\frac{-E_i}{k_B T}\right) - \exp\left(\frac{-E_j}{k_B T}\right) \right], \tag{42}$$

where A_{ij} is the Einstein coefficient of spontaneous emission and

$$\nu_0 = \left(E_j - E_i\right)/h. \tag{43}$$

The real power of this expression is its independence of the type of the transition involved. On the other hand, it demands state to state theoretical A_{ij} coefficients when no measured intensities are available. For example, when the transition involves different degrees of freedom, e. g., rotational and vibrational, combination of individual transition intensities is possible, but yet again caution must be taken to incorporate proper summation rules (Hansson and Watson 2005).

4.3.3 *Spectral Line Shape*

In low temperature plasmas and other gaseous media two types of line shapes are dominant. The most fundamental of all that would even affect a particle isolated in an otherwise empty space is called natural broadening. A direct consequence of the Heisenberg uncertainty principle of quantum mechanics. The broadening is proportional to the lifetime of the levels involved in the transition and the shape is a Lorentzian function

$$f(\nu)_L = \frac{1}{\pi} \frac{\Delta\nu/2}{\left(\nu - \nu_0\right)^2 + \left(\Delta\nu/2\right)^2}. \tag{44}$$

The Full Width at Half Maximum (FWHM) of the natural broadening equals

$$\Delta\nu_N = \frac{1}{2\pi}\left(\frac{1}{\tau_i} + \frac{1}{\tau_j}\right), \tag{45}$$

where τ, in this context, stands for the lifetime of a state. The radiative lifetime of a state j can be calculated as

$$\frac{1}{\tau_j} = \sum_{i<j} A_{ij} \tag{46}$$

summing over all lower levels for a fixed j.

Another example of homogeneous broadening mechanisms is the collisional or sometimes called pressure broadening. Collisions between molecules perturb the wavefunctions of the states involved.

Analogous of the radiative lifetime in the natural broadening, the determining quantity is the collisional frequency.

The most frequent inhomogeneous broadening mechanism is due to the Doppler shift of the radiation frequency experienced by a moving particle in the laboratory frame of reference. The radiation source and the detector are usually part of the laboratory frame of reference. Particles having a Maxwell-Boltzmann distribution of velocities produce a Gaussian line shape

$$f(\nu)_G = \frac{2\sqrt{\ln 2}}{\sqrt{\pi}\Delta\nu_D} \exp\left[-\left(\frac{2\sqrt{\ln 2}}{\Delta\nu_D}(\nu-\nu_0)\right)^2\right]. \tag{47}$$

The Doppler FWHM equals

$$\Delta\nu_D = 2\sqrt{\frac{2k_B T \ln 2}{mc^2}}\nu_0, \tag{48}$$

where m is the mass of the particle.

Assuming that the listed effects are decoupled from each other, we can calculate the spectral line shape for intermediate cases where neither the homogeneous or inhomogeneous mechanism dominates. The result is the convolution of both functions called the Voigt line shape. A comparison between the different line shapes is shown in Figure 11.

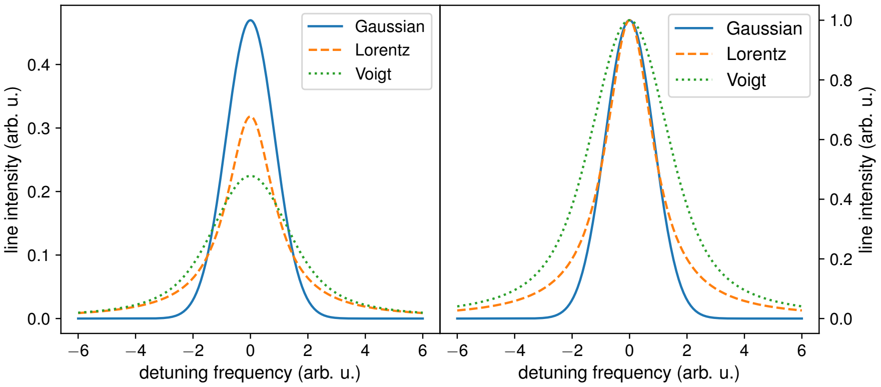

Figure 11. Comparison between the three major line shapes encountered in this thesis. The Gaussian and Lorentz lines have the same FWHM while the Voigt line is a convolution of the shown lines having double the FWHM. They are plotted as a function of normalised detuning frequency. Left and right panels show the same lines, each normalised to have unity area or maximum, respectively.

Further sources of broadening of absorption lines are instrumental effects, e. g., laser line width in absorption experiments or spectrometer resolution in emission measurements, and, in plasmas, the Stark broadening caused by the perturbing effect of electrical fields of particles.

High sensitivity measurements must also take into account some additional mechanisms such as pressure narrowing and speed-dependent effects.

4.3.4 *Optical Cavities*

In this subsection we will introduce the theory behind cavity enhanced methods, such as Cavity Ring-down Spectroscopy (CRDS). We will derive the basic formulas for the design of spectrometers and leave the technicalities of our applied method for the following subsection. As the name indicates, the heart of the method is a cavity, this time an optical one. Compared with its microwave counterpart an optical cavity is essentially an open resonator formed by a pair of opposing reflectors. A textbook example of such a resonator is the Fabry–Perot etalon, also called interferometer. It consists of a plane-parallel plate of thickness L and refractive index n with reflective surfaces[1]. The standard way to inspect the transmission characteristic of a resonator is to consider a monochromatic incident plane wave (for simplicity the case of normal incidence), calculate the phase difference between two successive reflections in the cavity and then sum up the infinite series of partial waves that interfere with each other. The phase difference is a function of the cavity length and refractive index, and the vacuum wavelength of the incident wave. For lossless reflectors the conversation of energy implies that the sum of mirror reflectance $\mathcal{R}$ and transmittance $\mathcal{T}$ equals to one. In this case the transmission characteristics of the resonator display resonance frequencies with unity transmission as shown in Figure 12. These are separated by the so called Free Spectral Range (FSR)

$$\nu_{\mathrm{FSR}} = \frac{c}{2nL}. \tag{49}$$

We can further define the etalon finesse as

$$\mathcal{F} \equiv \frac{\pi\sqrt{\mathcal{R}}}{1-\mathcal{R}} \tag{50}$$

which is used to characterise the etalon resolution. Both of these defined quantities depend only on the physical properties of the resonator. When the width of the high-transmission region is small compared to the separation between the peaks, these parameters can be used to estimate the FWHM of the transmission peaks

$$\nu_{\mathrm{FWHM}} \simeq \frac{\nu_{\mathrm{FSR}}}{\mathcal{F}}. \tag{51}$$

These parameters play an important role in the design of optical cavities, but we have not yet considered the stability criteria and

---

[1] This is actually a common form made out of a transparent solid with dielectric surfaces.

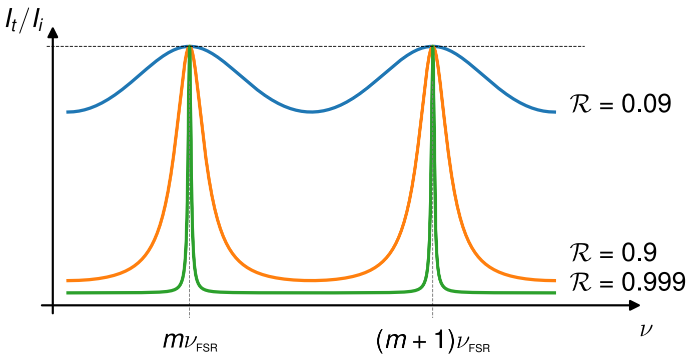

Figure 12. Transmission characteristics, ratio of incident and transmitted intensity, of Fabry-Perot etalon with different mirror reflectance as a function of light frequency. The two resonances are spaced by the Free Spectral Range, where m is the index of the longitudinal mode.

the cavity modes. Since one of our goals in CRDS is to effectively prolong the absorption length, or equivalently the photon lifetime in the cavity, we are seeking to excite modes with low losses. The above defined quantities strictly hold in the case of plane waves and real cavities have mirrors of finite extent. By considering curved mirrors (flat mirrors are a limiting case of infinite curvature) it can be shown that a cylindrical cavity supports a set of trapped normal modes of the electromagnetic field, known as Laguerre-Gaussian modes. They are labelled by TEM_{kl}, where k and l are integers labelling the radial and angular modes, respectively. Together with the longitudinal modes m they represent the possible standing waves in a cylindrical cavity. The practically most useful is the TEM_{00} mode which has a simple Gaussian radial beam profile concentrated close to the cavity axis. The higher modes can posses different resonant frequencies for the same longitudinal index depending on the configuration of the mirrors.

Using ray optics, it is possible to derive the stability criterion of a cylindrical cavity with concave mirrors of curvature R_1 and R_2, and mirror separation L as

$$0 < (1 - \frac{L}{R_1})(1 - \frac{L}{R_2}) < 1. \tag{52}$$

A pair of convex mirrors always forms unstable cavities and we only consider symmetrical resonators ($R = R_1 = R_2$), so the value of the curvature is given without a sign (as opposed to paraxial matrix-optics). It is evident that plane-parallel, symmetric confocal ($L = R$) and concentric ($L = 2R$) resonators lie on the verge of instability. Small deviations in the parameters lead to lossy cavities. Since our goal is to design a cavity that would function as an absorption spectrometer we limit our choices for $L < R$ where the trapped beam is focused minimally compared to the strongly focusing concentric case. For a given cavity length we can always find a suitable mirror curvature and the last parameter we need to consider is the focusing of the laser beam in terms of changes in beam width of the Gaussian radial profile.

The last technical parameter of an open optical resonator is the size of the mirrors which gives an acceptable upper limit for the so called spot size, an alternate technical term used for the beam width. The minimum spot size in a resonator with a pair of symmetrical concave mirrors occurs by symmetry in the centre. The spot size at any position inside the resonator is a function of the minimum spot size given by

$$\omega_0 = \left(\frac{\lambda}{\pi n}\right)^{1/2} \left(\frac{L}{2}\right)^{1/4} \left(R - \frac{L}{2}\right)^{1/4} \tag{53}$$

and the coordinate of the longitudinal position z. In the case of $R \gg L$, the bream spread, the change in ratio between the spot size at the mirrors and the minimal spot size, inside the resonator is negligible. For the other corner case of a confocal resonator ($R = L$) the spot size at the mirrors is $\sqrt{2}$ times larger than the minimal. For a fixed mirror curvature, the confocal configuration has the largest minimal spot size and beam spread inside the cavity.

The interrelatedness of all resonator parameters has consequences for both radial resolution of the system and the efficiency of the so called mode matching. The above mentioned relations were derived for the fundamental mode of the resonator, the one used most frequently in practical applications. Coupling efficiency of the incident beam into the resonator and subsequent excitation of its modes depends on the similarity of the input beam and excited modes. The incident beam has to possesses the same transverse modes, spot size and curvature as the mode to be excited and also the right frequency for the longitudinal resonance for efficient coupling.

4.3.5 *Cavity Ring-down Spectroscopy*

Cavity Ring-down Spectroscopy (CRDS) is one of the most widely developed and applied cavity enhanced methods available. There are several advantages when this method is applied to laser absorption experiments. A typical absorption setup would consist of a source of radiation, e. g., a laser, a container filled with the studied medium and a detector. In the aforementioned setup, study of systems with low number of absorbing particles or low intensity transitions becomes increasingly difficult. The useful signal, the absorbed power, is only a fraction of the laser power and detectors with high dynamic range are needed. An alternative solution is to prolong the absorption path in multi-pass configurations, but even those methods have their limitations. Furthermore, the precision measurement of relative intensities greatly depend on the laser output stability. For absolute measurements the detector also needs to be calibrated. CRDS overcomes all of these limitation by introducing a pair of highly-reflective mirrors into the basic configuration.

The expressions derived in the previous subsection are sufficient to design a functioning spectrometer based on the CRDS principle. The last missing piece of the puzzle is the derivation of the time dependent Ring-down (RD) signal that is the intensity leaking out of the finite reflectance cavity. For this purpose we are going to follow the original derivations applied in the case of a pulse-excited spectrometer derived by Lehmann and Romanini 1996. We can also apply this approach to the case of a cw-CRDS. The applicability of these two subtypes of cavity-enhanced spectrometers and their differences will be explained in the following text.

To avoid confusion in frequently used symbols and differences in terminology, we are starting this subsection with a short summary of the physical quantities and their symbols introduced so far. In optics the propagation of light is given by either the electric field, a generally complex field, or its intensity, where the second quantity are in units of power. The latter describes the light interaction with detectors and its practical application is evident. The mirror reflectance $\mathcal{R}$ and transmittance $\mathcal{T}$ introduced in this thesis are sometimes referred to as intensity reflectivity and transmittivity in the literature. These are derived as the square of the absolute value of the electric field reflectivity and transmittivity which are also complex quantities. For an infinitely thin reflector the sum of these complex quantities also equals one, derived from the continuity of the electric field. Multiple surfaces can be also combined to give single effective parameters as long as the dielectric coatings are avoided, otherwise the continuity of the electric field would break down. A common approach to differentiate between these quantities is to use the calligraphic symbols for the electric field and Latin letters of the intensity. However, this would lead to a confusion in the case of the mirror curvature R, also introduced in this thesis. Since it is not the goal of this subsection to give a thorough derivation of the needed equations we are going to use the already introduced nomenclature.

Now we are ready to commence the actual derivation of practical equations. First of all we define the round trip time in the optical cavity

$$t_r \equiv \frac{2nL}{c}. \tag{54}$$

The FSR of the cavity is nothing else than the reciprocal of the round trip time. Next, we assume that the cavity is excited by an electric field matched to the TEM_{00} mode of the cavity. This simplifies the calculations since the transverse beam profile is stationary and we only need to consider the problem in one dimension. For a cavity filled with a non-absorbing medium the electric field leaving the cavity is simply calculated by multiplying the input field by the square of the transmittivity (input and output) and the reflectivity depending on the number of passes through it. Each round trip changes the electric field amplitude by the square of the reflectivity and leads to a retardation of t_r. The output electric field is the sum of the possibly infinite number of passes through the cavity, which leads to an exponential temporal decay.

In this derivation the mirror reflectance and transmittance do not need to be frequency independent and so the decay lifetime (also called photon lifetime) of the measured output intensity equals

$$t_p = \frac{t_r \mathcal{R}}{2\left(1-\mathcal{R}\right)} = \frac{nL\mathcal{R}}{c\left(1-\mathcal{R}\right)}. \tag{55}$$

Absorption by molecules inside the cavity can be introduced by an effective reflectance

$$\mathcal{R}_{\text{eff}}\left(\nu\right) = \mathcal{R}\left(\nu\right)\exp\left(-\tau_a\left(\nu\right)\right) = \mathcal{R}\left(\nu\right)\exp\left(-\alpha_a\left(\nu\right)d_a\right), \tag{56}$$

where the exponential part containing d_a, an absorption length, holds for the case of a constant absorber along the beam propagation. Substituting the effective reflectance of Equation 56 into Equation 55 and taking its reciprocal, i. e., the decay rate, we get

$$1/t_c = \frac{c\left(1-\mathcal{R}_{\text{eff}}\right)}{nL\mathcal{R}_{\text{eff}}}. \tag{57}$$

From this we can derive the change in the photon lifetime compared to the empty cavity introduced by the absorbing medium as

$$1/t_a = \frac{c}{nL}\left(\frac{1-\exp\left(-\tau_a\right)}{\mathcal{R}\exp\left(-\tau_a\right)}\right) \approx \frac{c\tau_a}{nL\mathcal{R}}, \tag{58}$$

where for the approximation we only used the 1st term of the Taylor expansion of the exponential parts. The error introduced in this approximation is on the order of τ_a^2. Typical values of τ_a in cw-CRDS are well bellow 10^{-5} and its square can be safely omitted. The final photon decay rate in the cavity can be also written as the sum of the contributions from Equation 55 and Equation 58

$$1/t_c = 1/t_p + 1/t_a \approx \frac{c\left(1-\mathcal{R}\right)}{nL\mathcal{R}} + \frac{c\tau_a}{nL\mathcal{R}}. \tag{59}$$

Up to now the optical cavity has been excited by a theoretical electric field. In practice we can either use a pulsed laser setup which leads to the excitation of several longitudinal modes due to the broader spectral density of pulsed lasers (a consequence of the finite pulse length) compared to single mode continuous-wave lasers or use a method that allows fast optical switching of a continuous-wave laser. As shown by Lehmann and Romanini 1996, the requirement on the input source to observe a cavity RD is not a short pulse width compared to t_r, but rather the falling edge of the input pulse must be short compared to t_c for the excited modes. The above adapted derivation shows the principle of a continuous-wave excitation method that was first demonstrated by Romanini et al. 1997. The group used a fast Acousto-optic Modulator (AOM) to interrupt the laser beam after the intensity build up reached a sufficient threshold in the cavity.

Continuous lasers can posses orders of magnitude narrower line-widths than the pulsed counterparts. With the right set of parameters, it is possible to excite a single longitudinal mode of an optical cavity. This is usually done by fixing the central lasing frequency and modulating the cavity length. For precision spectroscopy, this needs to be done in a controlled manner. Romanini et al. 1997 solved the problem by introducing a piezo-transducer attached to the entry mirror and mechanically isolating the rest of the setup from surrounding mechanical vibrations. Modern high precision setups implement active stabilisation of both the laser and the cavity itself.

In this thesis, we are not attempting to implement ultra-hight sensitivity CRDS or precision molecular spectroscopy. The only parameters we need to concern ourselves with for the final spectrometer design are the laser line-width, FSR and finesse of the cavity, and the length of the AOM falling edge. These parameters will be given for a quantitative description of the spectrometers used in this thesis.

Following the previous theoretical parts we are left with the assessment of further, sometimes parasitic, systematic effects. A key assumption of the derivations is the mechanical stability of the cavity on the timescale of t_c. The frequency of characteristic vibrations (in all directions) must be much lower than the photon decay rate. This assumption determines the shape of the RD signal. The overall mechanical stability also determines the precision of the deduced optical depth. The sensitivity of the spectrometer is proportional to the finesse and the FSR of the cavity, as can be seen from Equation 59. The higher the sensitivity the less signal integration needed, and so the comparably long-term variations in the length of the cavity will introduce a lower minimal achievable sensitivity. Thus the mechanical nature of the cavity needs to be considered in two different aspects of the implemented spectrometers. An interesting aspect of CRDS is that for a cavity filled with a homogeneous absorber the optical depth, in a 1^{st} approximation, does not depend on the length of the cavity ($\tau_a = \alpha_a L$) and so the smaller the spectrometer is constructed the higher its sensitivity gets.

4.3.6 *Temporally Resolved CRDS*

In the previous subsection we considered a cw-CRDS filled with an absorber of arbitrary properties and distribution along the line-of-sight of the probing laser beam. This absorber was stationary in time.

Our next goal is to apply this method for the probing of temporally changing absorption signals (the photon lifetime itself). This is not a trivial matter, considering the possible effects on the optical field.

The primary approximation used here is specifically chosen for the case of our experiments and assumes that the characteristic changes in time of the absorption signal are happening on a much longer timescale than t_r, i. e., during each round trip τ_a is quasi-stationary. The shape of the resulting RD signal is derived by considering the differential equation governing the temporal evolution of the light intensity leaking out of the cavity

$$\frac{dI(t)}{dt} = -1/t_c(t)\, I(t)\,. \tag{60}$$

Identical to Equation 33, the solution arrives in an integral form where the exponent of the exponential-like decay is given by the temporal integral

$$-\int_{t_0}^{t} 1/t_c\left(t'\right) dt' / \left(t - t_0\right). \tag{61}$$

As implied from the applied assumptions, this approach is valid in the case of small perturbations. A direct consequence of this solution is that even though the RD signal contains the full information about the temporal evolution of the absorption signal, it is encoded in an integral form and necessitates the consideration of advanced data reduction procedures. The practical importance of this, is that suddenly we are interested in determining a larger number of parameters from the same 'noisy' signal and so the valuable data and gathered statistics is split between a higher number of potentially determined parameters.

The analysis of temporally resolved CRDS systems will be discussed in Section 8.3 by considering the validity and precision of several data reduction methods applied in the course of this work.

4.3.7 *A cw-Cavity Ring-down Spectrometer*

In the final subsection of this chapter we describe the major components of an actual cw-CRDS. Parameters of specific implementations, e. g., mirror reflectance and its spectral range, and many more, are omitted in this description and will be given in the respective experimental chapters.

The optical setups used in the experiments presented in this thesis were designed to accommodate both fibre-coupled and free-space lasers. This way we can consider the start of the mode matching optics at an equivalent point that is practically either a fibre-output collimator or the actual output of a free-space laser. This is usually followed by an additional optical filter to minimise feedback from the high reflectance input mirror of the cavity and the rest of the optical setup.

The laser beam switch, in the from of a free-space AOM, is always situated right after the light source of the setup. The two models used in the simultaneous setup of two laser types are driven by RF drivers at a frequency of 80 MHz and controlled by digital signals. The 1st order diffracted beam, which is also frequency shifted due to the acousto-optic diffraction, is separated from the main beam and propagated to the next stage of the mode matching optics. Its frequency shift approximately equals the drive frequency of the modulator which was also experimentally determined by a wavemeter (see last paragraph of this subsection).

The rest of the optics setup consists of a pair of lenses and several mirrors that transform the spot size and the collimation properties of the laser beam to match them to the cavity. Optionally, a precision pinhole can be included in the setup which transform the transverse shape of the beam into a fundamental TEM_{00} mode. The main deviations from this shape can be caused by the AOM itself or the quality of the output beam collimation of different laser systems.

After successful mode matching and spatial filtering of the incident laser beam, and also the mutual alignment of the cavity mirrors we are ready to observe RD signals. On the detector side we require a linear response to the detected light intensity (in units of power) with a bandwidth that is sufficiently high to cover the fastest decaying signals. A compact and powerful choice is the combination of an Avalanche Photodiode (APD) with a high bandwidth, transimpedance amplifier. This signal is split between a digitaliser and an analogue triggering circuit.

When the mechanical vibrations of the optical cavity are too low amplitude to be able to modulate its length and cover the resonances, the alternative choice is controlled modulation by a piezo-transducer attached to one of the cavity mirrors. The longitudinal resonances can be excited either by applying a single frequency triangle voltage wave or a waveform consisting of a small amplitude sine-like wave and a servo-system driven offset value on the piezo-transducer. The second method is used to enhance the number of RD events for a given time period and its frequency is limited by the assumption of a stationary cavity during a RD event.

The analogue trigger circuit controls the AOM drivers and the piezo-waveform. Once the cavity mode frequency matches with the laser, intensity builds up fast in the cavity. The outgoing power is monitored continuously and once a given threshold is exceeded the AOM driver receives an 'OFF' digital signal. The falling edge of the optical field is given by the combination of the driver and optical crystal characteristics. There is usually a delay in the response of a driver. These parameters together determine a part of the RD signal that is still under the influence of the incident laser power and should be skipped by the data recording or processing suites. A pre-determined part of the RD waveform is digitalised by a linear Analogue-to-Digital Converter (ADC) at a sampling rate of 1.25 MHz. These waveforms have a fixed length and can be processed on-line. They are stored and re-processed off-line using one of the data reduction methods presented in Section 8.3.

The last instrument needed to finish the spectrometer is an absolute wavemeter. In our setup this role is played by a scanning Michelson interferometer-based wavemeter with a guaranteed absolute accuracy of ±0.3 pm and displayed resolution 0.1 pm. The input laser power is taken either directly from the fibre-coupled beam or recycled from the 0^{th} order diffracted beam. The wavemeter displays the not yet shifted laser wavelength in vacuum.

5

DEUTERATED ISOTOPOLOGUES OF H_3^+

This chapter is the very first one where experimental data gathered during the course of my work and studies are presented. The key topic of this chapter is the examination of isotope effects in ion-neutral and electron-ion elementary processes that are linked to the isotopic fractionation observed in many cold environments. We are not revisiting the fundamental motivation of this research but rather present the obtained results in the context of future work on DR studies.

The present experiments were conducted on the experimental apparatus described in Chapter 4 employing a combination of the SA and CRDS techniques. During this experimental campaign I played a largely technical role and was responsible for data gathering and on site technical support. Some of the raw data serving as the base of this chapter were already processed and published in two research articles by Dohnal et al. 2016 and Plašil et al. 2017. The main topic of these articles were binary and ternary recombination of the observed H_3^+ isotopologues. Here I will present a follow-up rigorous data processing approach enhanced by new measurements and insight into possible systematic uncertainties regarding the experiments some of which were not yet available during the preparation of the cited articles.

Here I will also present the technical and statistical methods that play a central role in data evaluation and interpretation, and are used throughout the upcoming experimental chapters. The chemical models introduced in Section 3.1.3 will be also compared with available experimental data.

5.1 STATISTICAL TOOLS

In Section 4.3.7 we have defined and described what is a working cw-CRDS. In Section 8.3 we will examine the methods how to handle individual RD signals when some of the assumptions of the basic data processing method are not valid any more. Here we take the already evaluated photon decay rate and its statistical uncertainty and assume that each of these events can be assigned a unique time parameter relative to the periodic discharge cycle. The basic statistical uncertainty of the photon decay rate is simply due to electric noise of the measured RD signal. Its evaluation can result in additional systematic errors due to approximate models. And finally, there are further fundamental effects that limit the sensitivity in terms of absorption strength and precision of wavelength determination of a cw-CRDS.

PARAMETER	VALUE
Reflectance	>0.9999
FSR	200 MHz
Finesse	44 000
Photon lifetime	35 µs
Length	750 mm
Mir. curvature	1000 mm
Mir. diameter	7.75 mm

Table 4. Typical parameters of the employed cw-CRDS.

We can perform pure spectrometry on neutral species or simply determine the quality of the empty cavity without the temporally resolved rates to examine some of the effects that limit the sensitivity and precision of our spectrometer. Our primary purpose in this chapter is to use our spectrometer to retrieve absolute ion number densities, so our focus is on sensitivity. The other key feature of a cw-CRDS, precision of wavelength determination, will be examined in Chapter 6.

In this section we will present the statistical tools at our disposal and test them on actual experimental data documenting the procedure of how to extract physical quantities just from a couple of thousand RD signals. This analysis will not reappear in the other experimental chapters since the basic ideas are the same and so it will be sufficient to present the differences in key physical parameters of the spectrometer system that determine its sensitivity.

5.1.1 *The Baseline*

The theory of CRDS tells us that in a first approximation we can split the rate of the measured RD signal into a part that is purely dependent on the quality of the optical cavity and into a part that is proportional to the absorption caused by molecules filling out the volume between the mirrors. The first part is often referred to as the baseline of a cavity ring-down absorption spectrum. It can be either measured directly in an evacuated cavity or determined from a recorded spectrum based on the shape of the probed absorption line and some kind of functional form of the spectral characteristics of mirror reflectance. Both methods have their drawbacks that are linked to the fundamental sensitivity of a real spectrometer.

A second examination of Equation 55, the formula for the photon lifetime in an evacuated cavity, reveals that variations in the mirror reflectance and cavity length (and also the refractive index) cause fluctuations of the photon lifetime. What is important from a practical point of view that these variations have different characteristic frequencies. At this point we are required to leave the generalised approach behind and continue with the concrete implementation. The characteristic parameters of the employed spectrometer are listed in Table 4.

The highest allowed frequencies of mechanical vibrations are limited by a combination of the duration of the waveform acquisition, which is typically shorter than 500 µs, and the photon lifetime. Anything higher will directly disrupt the RD events. On the other hand, CRDS itself is based on mechanical vibrations (or modulations) that help to match the longitudinal mode frequency to that of the laser source. We employed two types of semiconductor based laser sources to cover the chosen second overtone ro-vibrational transitions of the $H_3{}^+$ isotopologue system. The characteristic parameters of the laser sources are listed in Table 5.

The most frequently employed sources in our experiments belong to the Distributed Feedback (DFB) laser diode family. They come in a variety of standards and are frequently used for their excellent frequency stability and high quality emission spectrum. The rather limited tuning range is by definition mode-hop free. We keep the laser current stabilised at a constant value and tune the frequency by slowly changing the chip temperature. This usually results in a more stable power output compared to current tuning. Although CRDS is unaffected by power fluctuations, the number of recorded RD events per unit time depends on the average incident power. The quality of the thermo-electric stabilisation directly affects the centre lasing frequency and so it plays a major role in the precision of the wavelength determination.

The second laser type employed in the present experiments belongs to the External Cavity Diode Laser (ECDL) family. These laser sources, as the name implies, use external cavities to provide a narrower linewidth compared to DFB laser diodes. The extended tuning range is thanks to a rotatable external grating, sometimes equipped with a piezo-electric transducer for fine tuning. We keep both the laser current and temperature stabilised and vary the piezo voltage during spectral scanning.

Combining the knowledge about the laser sources with that of the optical cavity parameters we can continue to examining the possible sources of fluctuation in the CRDS absorption baseline. The orders of magnitude narrower cavity transmission peaks compared to laser line widths would only limit us in case we would like to go beyond the wavelength precision of the employed wavemeter and laser sources. The allowed fluctuation of the actual frequency of a longitudinal resonance for a fixed central lasing wavelength is on the order of the laser line width. On the other hand, the distance in length between two resonances for the same central frequency (in the wavelength

PARAMETER	DFB LD	ECDL
Wavelength	1.54 µm	1.46 µm
Tuning range	≈20 cm^{-1}	>100 nm
Linewidth (1 ms)	<10 MHz	<300 kHz
Thermal stability	–	100 MHz/°C
Frequency tuning	temperature	piezo voltage

Table 5. Typical parameters of the employed laser sources.

range of the light sources) is close to 1 µm. The maximal piezo length modulation of the optical cavity was set to roughly one and a half times this distance so that when the laser wavelength is tuned a new resonance would be always accessible. The lower amplitude but higher frequency sinusoidal modulation had a fraction of this maximal span. Purely random mechanical vibrations did not cause observable RD events and can be generally ruled out from this assessment.

Below the Hz level mechanical changes are usually caused by thermal fluctuations. Changes in room temperature are already detectable by monitoring the baseline at a constant laser wavelength. In our case this is enhanced by the cooling system of the discharge container so special care was taken during the below room temperature experiments to have stable thermal conditions. The effects were usually the most severe at liquid nitrogen temperatures. The boiling cryogenic liquid, if not handled carefully, can cause temperature fluctuations of several percent. The amplitude of maximal thermal contractions at a stable temperature were comparable to that of the piezo length modulation.

Adding up the contributions from both mechanical and thermal sources, we can estimate the maximal length variations at intermediate time scales (on the order of seconds) to roughly 3 µm. Compared to the full length of the cavity we are on the ppm level. We can reach this limit in the experiments for substantial integration times. In the upcoming section we will show how to partially avoid it for temporally changing signals.

5.1.2 *Differential Signals*

The most powerful advantage of probing temporally changing absorption features is the possibility to track both the main signal and the CRDS baseline simultaneously. Naturally, this ought to be verified on a case-to-case basis, taking into account all contributing species. The general idea is that at each step of a spectral measurement we choose two time windows in the temporally resolved signal and the final result equals the difference of the respective averages. As a consequence, we immediately filter out variations on time scales longer than the integration time at a given wavelength in the recorded spectrum. The same idea is behind the extraction of temporally resolved ion number densities where we similarly subtract the CRDS baseline. The main difference is in integration times and so first we examine the evaluation of absorption lines where the spectra are usually averaged over the nominal discharge period.

In this thesis experimental absorption profiles of temporally evolving species represent photon decay rates averaged over a given time period where each point is measured at a fixed laser wavelength. For absorption lines with a FWHM orders of magnitude greater than the laser line width the effect of wavelength uncertainty on the profile shape can be usually omitted. And so the main sources of error in shape determination are the fundamental statistical uncertainties of the RD events, the previously described, short time baseline variations and any fluctuations in the actual temporally evolving absorption signals.

At this point statistics enter the picture. For a start, we can assume that the signal we are attempting to extract is quasi-stationary. And the amplitude of any temporal changes in absorption are small enough to be negligible when fitting the RD events with a basic exponential function. The first step of data processing is to filter out potentially faulty signals caused by salt-and-pepper like noise. This is done by taking the goodness of fit parameter of each RD event which is evaluated under the assumption of a constant white noise on the digitalised signals, same for the whole recorded batch. Individual cuts operating on the goodness of fit population are assigned for each data set until only a chi-squared-like distribution remains. This method is applied whether we are interested in quasi-stationary or dynamically evolving signals and is applicable only if the deviation of the individual RD signals from a true exponential is lower than the electric noise. More on this topic will be discussed in Section 8.3.

The next step is to choose a suitable time window for averaging and display the photon decay rate population in a histogram. What we get is most likely not a Gaussian distribution due to non-linear fitting and other systematic effects that for example can only shorten the photon lifetime. Bayesian inference is also out of the question since we are looking for that one parameter that describes the quantity of light absorbed by certain amount of molecules. Since we already used some goodness of fit estimator to compare the extracted rates to each other it is logical to follow the same approach and calculate a weighted average to represent the statistical population. The weights are taken as the reciprocal square of the standard error estimate of the non-linear fitting. From the same population we can also estimate the overall error of the weighted average estimator by comparing with the standard deviation of the population or by bootstrapping. In case the absolute statistical error of the photon decay rates can be also estimated from the RD signal, we have a secondary test to distinguish between propagating statistical and systematic errors.

The discharge time window of the processed absorption spectra, when not otherwise stated, was chosen to start 200 µs after the beginning of the discharge cycle and end the same 200 µs before the termination of the microwave power. This region corresponds to the most stable part of the active discharge where the RD events see a quasi-stationary absorption signal in time. Minor instabilities of the incident microwave power can cause fluctuations in the ion number density, as explained, these effects are incorporated in the statistical data processing. We kept the full duration of the microwave pulse in the experiments below 2 ms followed by a similar but slightly longer afterglow period.

The baseline time window was chosen as roughly the last 500 µs before the end of the complete discharge/afterglow period. The exact value is a compromise between sufficient statistics and as low as possible residual absorption signal. The same approach to estimate the baseline was used when extracting temporally evolving absorption signals at a fixed frequency, e. g., at the maximum of an absorption line.

In the following text absorption lines are displayed as the evaluated optical depth versus measured wavenumber of the laser light corrected for the AOM shift. When not otherwise stated, absorption signal refers to the determined optical depth rather than the photon decay rate.

5.2 ION AIDED THERMOMETRY

A key feature of the H_3^+ isotopologue experimental campaign was the systematic study of this system in the nominal temperature range of 80 K to 150 K. The lowest accessible value was limited by the cooling system (liquid nitrogen). The upper limit was chosen due to the fact that the maximal signal-to-noise ratio of the accessible absorption lines is decreasing by increasing temperature (Doppler width and transitions strengths) and the overall ion number density, usually available for a single dominant species, was split into four parts.

We employed two kinds of coolants in the nominal temperature range. Liquid nitrogen for the lowest and its pre-cooled vapours for the higher temperatures. Liquid nitrogen provides a more homogeneous cooling power between the inlet and exhaust of the coolant bath but can produce a higher degree of thermal fluctuation. The steady flow of the pre-cooled vapours provides a mechanically more stable system but inherently results in a temperature gradient between inlet and exhaust. A temperature sensor was placed through the exhaust into the cooling bath volume in both configurations to estimate the coolant temperature.

Optimally, one would like to measure directly the neutral gas or the discharge container wall temperature. Both are near impossible to realise since the microwave resonator does not tolerate anything metallic in its inside volume, an internal sensor would most likely compromise the purity of the neutral gas and anything from the outer side would be still influenced by the surrounding coolant. Our approach consisted of monitoring the Doppler width of absorption lines and populations of several rotational states of the studied ions to determine the neutral temperature. The same approach was successfully applied in several previous experimental campaigns of H_3^+ recombination studies where the comparison of experimentally evaluated translational and rotational temperatures showed a good agreement, see, e. g., Hejduk et al. 2015.

5.2.1 *Translational Temperature*

We conducted several dedicated absorption spectrum measurements during the experimental campaign to evaluate the translational temperature of the ion ensemble in the range of experimental temperatures. During the measurements we encountered additional absorption features in the regions of interest that were identifies as transitions belonging to several vibrational bands of the $b^3\Pi_g \leftarrow a^3\Sigma_u^+$ electronic system of the He_2 molecule. These absorption spectra and the analysis of the temporal evolution of these molecules were published in a separate research article (Kálosi et al. 2016).

None of the newly observed absorption lines are directly overlapping with those belonging to H_2D^+ and $HD_2{}^+$. There was a large difference in the observed intensities, meaning that the electronic transitions of the metastable neutral molecules were orders of magnitude more intense, also depending on the experimental conditions. The amount of metastable molecules present in the experiments and its dependence on the conditions was also studied in the cited article. We note that the temporal evolution of these absorbing species closely follows the discharge cycle, i. e., they decay after the termination of the microwave power on the timescale of a few tens of microseconds.

Here we process absorption spectra that were recorded at our standard experimental conditions. We used a mixture of $He/Ar/H_2/D_2$ gas with typical number densities of $(10^{17}/10^{14}/10^{14}/10^{14})\ \mathrm{cm}^{-3}$. Only normal H_2 and D_2 gases were used, meaning that the *para/ortho* fractions of these neutral molecules are frozen at the respective high temperature statistical values. Similar to our previous studies of H_3^+ recombination in afterglow plasmas, we systematically studied the isotopologue system in the buffer gas pressure range 500 Pa to 1500 Pa. We kept $[Ar]$ and $[H_2] + [D_2]$ at a constant value of $1 \times 10^{14}\ \mathrm{cm}^{-3}$ or $2 \times 10^{14}\ \mathrm{cm}^{-3}$ in all the experiments.

ION	TRANSITION		$\tilde{\nu}$ (cm^{-1})		
	ROT.	VIB.	PRESENT	OBS.	CALC.
$H_3{}^+$	$2_3 \leftarrow 3_3$	$(0, 3^1)$	6807.2813(2)	6807.297	6807.335
H_2D^+	$2_{02} \leftarrow 1_{11}$	$(0, 2, 1)$	6459.036(3)	6458.794	6459.133
	$1_{11} \leftarrow 0_{00}$	$(0, 2, 1)$	6466.5308(6)	6466.532	6466.300
	$2_{12} \leftarrow 1_{01}$	$(0, 2, 1)$	6491.3469(3)	6491.349	6491.124
$HD_2{}^+$	$1_{01} \leftarrow 1_{10}$	$(1, 2, 0)$	6466.9342(10)	6466.936	6466.916
	$2_{12} \leftarrow 1_{01}$	$(1, 2, 0)$	6535.9527(2)	6535.953	6535.943
	$1_{11} \leftarrow 0_{00}$	$(1, 0, 2)$	6536.3165(2)	6536.319	6536.301
$D_3{}^+$	$3_2 \leftarrow 2_2$	$(0, 3^1)$	6848.5014(5)	6848.505	6848.712

Table 6. A list of transitions of the $H_3{}^+$ isotopologue system probed in the experiments presented in this thesis. Central wavenumbers $\tilde{\nu}$ labelled as 'present' and their error estimates were obtained in the current analysis. The values labelled as 'obs.' and 'calc.' are taken from Table 1. For a description of the transition labelling and used sources see Table 1.

Each recorded spectrum covers a limited wavenumber range. These pieces were analysed individually and assigned a set of central positions and spectral line shapes. It was usually unnecessary to restrict the recorded spectral regions to even smaller parts and the visible absorption features were fitted as a sum of individual line shapes and a constant background. In certain cases the contribution of absorption lines lying just outside the recorded region was approximated by a polynomial background function. Absorption lines with high enough signal-to-noise ratio were fitted with a Voigt line shape. Pressure broadening (even for $H_3{}^+$) contributes to the overall line width in the covered temperature and pressure range. An approximate approach in the form of a Gaussian line shape was applied to the more noisy spectra to deduce line positions only. The present experimentally determined transition wavenumbers of the probed $H_3{}^+$ isotopologue transitions are listed in Table 6.

Ion translational temperatures were determined exclusively from the Doppler contribution of the fitted Voigt line shapes. Due to the largely unknown pressure broadening, individual Doppler width values have a statistical error ranging from several percent to higher. Figure 13 shows an attempt to compare the measured coolant temperatures with that of the experimental ion translational temperatures. We can group the individual values by four distinct coolant temperatures and calculate a weighted average as shown in Figure 13. The actual coolant temperature assigned to the individual values in Figure 13 is not important (they are scattered in the figure for clarity). We use only the weighted averages in the upcoming analysis to estimate the neutral temperature in the experiments at nominal wall temperatures.

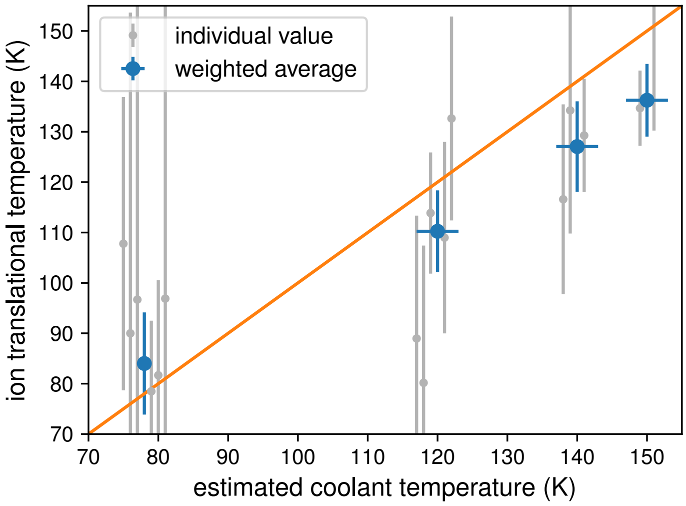

Figure 13. Ion translational temperature of H_3^+ isotopologues determined in various experiments as a function of estimated coolant temperature. All individual values are evaluated from the Doppler contribution of Voigt line profiles only. These are plotted as a function of the coolant temperature and scattered in the horizontal direction for better visibility. The weighted averaging includes only the vertical error bars. Any difference in the actual coolant temperatures is neglected in the averaging. The full line represents the case of equal ion and coolant temperatures.

As it can be seen from Figure 13, liquid nitrogen provides the most homogeneous coolant temperature based on the agreement with the average ion translational temperature. The heating power deposited in the active discharge (mediated by the electrons) could cause elevated neutral gas temperatures depending on the actual incident microwave power and duty cycle of the periodic pulses. Taking this effect into account, the liquid nitrogen temperature is used as the lower estimate of the discharge container wall temperature in the following analysis.

The same cannot be said about the experiments where we used nitrogen vapours as the coolant. The average ion translational temperatures are systematically lower than the estimated coolant temperatures. These provide an upper estimate of the discharge container wall temperature. The deviation from the behaviour at liquid nitrogen temperature can be simply explained by a temperature gradient along the coolant flow. The fused silica discharge container and the flowing gas is pre-cooled in this case. The coolant exhaust and the inserted temperature sensor were located at the outflow side of the apparatus. In these cases we need to fully rely on the experimentally deducted translational or rotational temperatures of the ions to estimate the neutral gas temperature.

5.2.2 *Rotational Temperature*

We used two approaches in the experiments to record data for ion rotational temperature evaluation. In both cases we were restricted to H_2D^+ and $HD_2{}^+$, since only these two species had several rotational states accessible in the probed range of wavenumbers. The standard approach is to record complete absorption lines originating from several rotational states of a chosen ion. This was only possible in a certain range of conditions were all lines could be recorded with sufficient signal-to-noise ratios. An example is shown in Figure 14. These lines were recorded in a mixture of He/Ar/H_2/D_2 gasses with overall pressure of 500 Pa at 80 K nominal discharge container wall temperature. Derived reactant number densities are $[\mathrm{Ar}] = 2.2 \times 10^{14}\,\mathrm{cm}^{-3}$, $[\mathrm{H_2}] = 9.4 \times 10^{13}\,\mathrm{cm}^{-3}$ and $[\mathrm{D_2}] = 9.5 \times 10^{13}\,\mathrm{cm}^{-3}$. The rotational temperature derived from the area ratios of the lines is $(70 \pm 13)\,\mathrm{K}$.

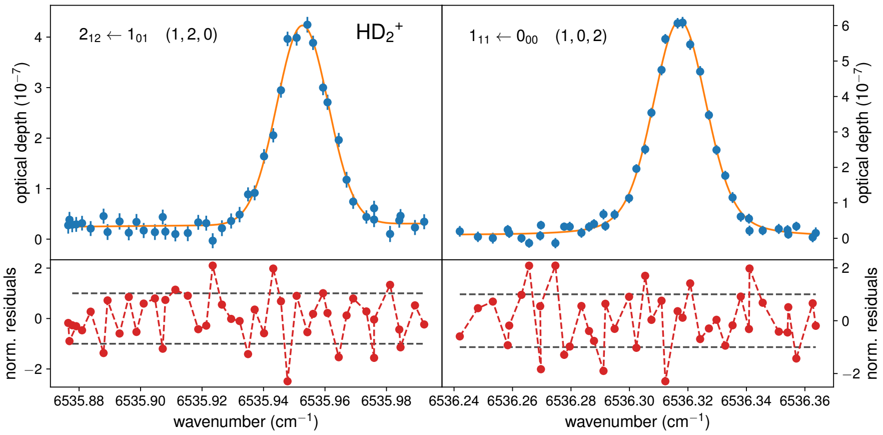

Figure 14. A pair of recorded absorption lines (symbols) of $HD_2{}^+$ suitable for rotational temperature determination recorded at 80 K nominal temperature (see text for experimental conditions). The transition labels are shown in the respective upper panels of the figure together with the Voig line profile fits (full line). The lower panels show the respective normalised residuals of the non-linear fits by a Voigt line profile, i. e., the difference between data points and fitted values divided by the estimated standard uncertainty of the data points. The dashed lines show the one sigma limits. The average translational temperature and pressure broadened FWHM determined from both lines is $(80 \pm 10)\,\mathrm{K}$ and $(4.5 \pm 1.9)\,\mathrm{cm}^{-1}$, respectively. The rotational temperature derived from the area ratios of the lines is $(70 \pm 13)\,\mathrm{K}$.

In an alternate approach, we integrated the absorption signal at the near-centre of the spectral lines, maximising the available signal strength. In each case we recorded the background contribution from neighbouring absorption features, eliminating the need for time consuming full spectral measurements. The recorded wavelength of the laser sources is available to correct for a possible difference in the set and centre frequencies. The recorded absorption signals are divided by the transition dependent parts of the respective integral intensity factors (Equation 42) to evaluate relative observed intensities of the transitions. For a Boltzmann distribution this is directly linked to the state populations and the rotational temperature, where the relative intensities are a near-exponential function of lower state energies.

The results of two sets of measurements utilising the near-centre signal integration technique are shown in Figure 15. The two measurements probed all three available HD_2^+ transitions and differed in the H_2/D_2 ratios of the He/Ar/H_2/D_2 gas mixture with an overall pressure of 920 Pa at 80 K nominal temperature. Derived reactant number densities for values plotted as circles and triangles in Figure 15 are $[Ar] = 8.7 \times 10^{13}\,cm^{-3}$, $[H_2] = 3.8 \times 10^{13}\,cm^{-3}$, and $[D_2] = 1.1 \times 10^{14}\,cm^{-3}$ and $[Ar] = 1.8 \times 10^{14}\,cm^{-3}$, $[H_2] = 7.7 \times 10^{13}\,cm^{-3}$, and $[D_2] = 5.5 \times 10^{13}\,cm^{-3}$, respectively. The relative H_2/D_2 ratios will be represented by F_{D_2} in this analysis as defined in Equation 10. The absolute number density of HD_2^+ ions in the presented experiments is reflected in the magnitude of the plotted relative intensities. The rotational temperature values are determined from the fitted exponential functions. Values determined from all the transitions are (150 ± 20) K and (59 ± 5) K, respectively.

We also monitored the intensities of two H_2D^+ transitions during the two measurements. The derived rotational temperature values are (85 ± 17) K and (89 ± 8) K, respectively. The large discrepancy between the respective rotational temperature values and also with the average translational temperature determined in other 80 K nominal temperature experiments raises suspicion about the estimated background contribution used in the analysis. Excluding the lowest state transitions due to this suspected systematic error leads to (90 ± 30) K and (100 ± 50) K, respectively.

The background contribution in these experiments was measured on a single side of the absorption lines. In subsequent measurements we regularly monitored both sides for a more reliable background estimate.

5.2.3 *Neutral Gas Temperature*

The final neutral gas and ion temperature used for absolute reactant and ion number density determination is estimated as the average of both translational and rotational ion temperature evaluations. The measured coolant temperatures are also used as upper or lower estimates, as explained previously, and also to categorise the data in the absence of a high fidelity ion temperature measurement. The final temperature estimates used in the subsequent analysis are listed in Table 7.

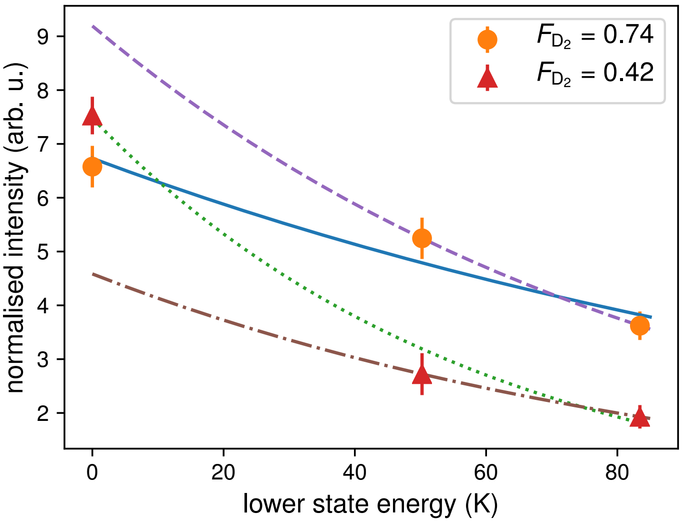

Figure 15. Observed relative intensities of HD_2^+ transitions derived from the maximum of the measured absorption signal for rotational temperature determination at 80 K nominal temperature. See text for experimental conditions. The transitions are identified by the lower state energy. The two sets of measurements were conducted at two different H_2/D_2 ratios (represented by F_{D_2} in the figure legend). The rotational temperature values are determined from the fitted exponential functions. Values determined for circles and triangles are (150 ± 20) K and (59 ± 5) K, respectively. These are represented by the full and dotted lines, respectively. Excluding the lowest state transitions due to a suspected systematic error leads to (90 ± 30) K and (100 ± 50) K, respectively. These are represented by the dashed and dot-dashed lines, respectively.

Based on previous experimental findings and data presented here we will assume for the rest of the analysis that the ion translational and rotational temperatures are a good estimator of the neutral gas temperature in the range of experimental uncertainties. This claim is supported by the good agreement with upper and lower estimates of the discharge container wall temperature. Furthermore, the values of both ion translational and rotational temperatures are determined as averages in the active discharge, where the influence of electron impact excitation could be the strongest. No statistically significant differences were observed most likely due to efficient buffer gas cooling. Also, any heat load from the microwave field to the neutral gas would eventually reach the discharge container wall leading to an increase in its temperature and some final steady state distribution due to the repetitive nature of the experiments. Heat transport due to particle diffusion is also happening on a similar time scale as the period of the experiments. Further supporting evidence is that the absorption measurements probe the near-centre of the discharge container which

TEMPERATURE (K)	
NOMINAL	ESTIMATED
80	87 ± 6
115	113 ± 7
130	127 ± 9
140	136 ± 7

Table 7. Estimated temperatures in He/Ar/H_2/D_2 experiments.

is the most sensitive to increased temperatures in the discharge. For further discussion see Section 4.2.4.

5.3 ISOTOPIC FRACTIONATION

Knowing the location, shape and strength of suitable transitions and also the rotational temperature governing the population distribution of states allows us to evaluate the absolute column number density of the H_3^+ isotopologues present in the experiments.

First of all, we are interested in relative ion densities of the individual isotopologues, determined as the ratio of the absolute column number density divided by the sum for all isotopologues. We are looking for the maximum signal to noise ratio which means averaging the discharge values as described previously. The individual ion column number densities are evaluated the same way as the alternative rotational temperature evaluation method. During each measurement we integrated the ion absorption signal at the near-centre of the spectral lines and recorded background values at one or two sides of the absorption lines.

Due to technical reasons, we repeated each experiment twice. We recorded the single point spectral values at the near-maxima of both H_2D^+ and HD_2^+ and either of H_3^+ or D_3^+ absorption lines. The difference in H_2D^+ and HD_2^+ column densities between the repeated experiments is not statistically significant and in the final evaluation the sum of column number densities is determined from the combined measurements.

Figure 16 shows two examples of evaluated relative ion densities at a nominal temperature of 115 K. In all similar experiments, we kept the overall pressure, [Ar] and $[H_2] + [D_2]$ constant and varied only the relative D_2 partial density F_{D_2}. Since F_{D_2} does not depend on the assumed temperature, it can be determined within the precision of a few percent from the respective mas flows of gases. The actual experimental conditions for Figure 16 were mixture of He/Ar/H_2/D_2 gasses with overall pressure of 500 Pa at 115 K nominal temperature. Derived reactant number densities are $[Ar] = 2.0 \times 10^{14}\,\mathrm{cm}^{-3}$, $[H_2] +$

$[D_2] = 2.1 \times 10^{14}\,\text{cm}^{-3}$. The symbols in the left panel represent relative ion number densities evaluated as described above. The error bars represent only the statistical uncertainties of the data evaluation. These are compared with simple chemical model calculations based on isotopic substitution in ion-neutral reactive collisions. The full lines in both panels represent the 300 K model of Fárník et al. 2002. Similarly, the dashed lines represent the model of Hugo, Asvany, and Schlemmer 2009. These are based on the extrapolation of the calculated rate coefficient values to 70 K.

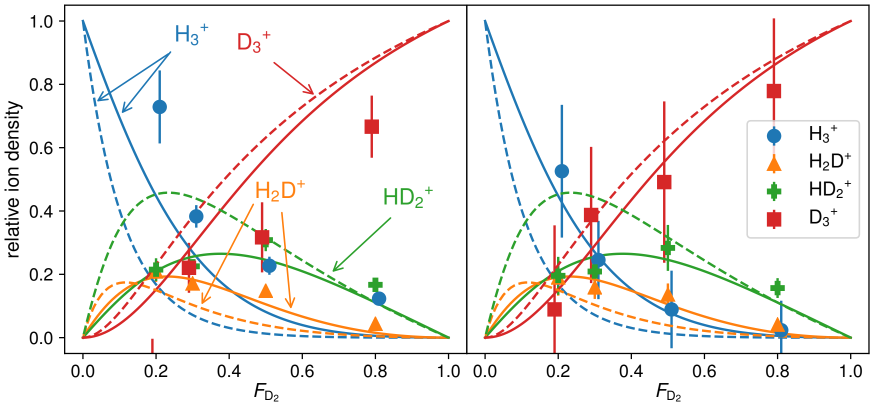

Figure 16. Derived relative densities of $H_3{}^+$ isotopologues as a function of F_{D_2}. See text for experimental conditions. Symbols in both panels represent experimentally determined values in the procedures described in the text. The left panel shows the raw values, while the right panel shows the values corrected for possible systematic background contributions. They are scattered around the actual F_{D_2} values for better visibility. The symbol labels are shared between the panels. The full lines represent the 300 K model of Fárník et al. 2002. The dashed lines represent the model of Hugo, Asvany, and Schlemmer 2009 extrapolated to 70 K. All model calculations are the same for the two panels, labels are shown only in the left panel for better visibility.

The two chemical models are chosen to demonstrate the full range of possible relative ion number densities. The rate coefficients measured or estimated for a temperature of 300 K can well represent even lower temperatures where the ions still posses a rather statistical population of rotational states and state-to-state effects play a minor role. The same is true for normal H_2 and D_2 reactant gases that at very low temperatures store additional internal energy due to the 'frozen' spins. On the other hand, the state-to-state rate coefficients of Hugo, Asvany, and Schlemmer 2009 represent an approach of the situation from the direction of low temperatures where stated rotational effect might play a larger role. We can expect to find the relative ratios in the range between the two models.

Another look at the left panel of Figure 16 reveals a significant discrepancy between the evaluated values and both models for ${H_3}^+$ and ${D_3}^+$. A possible explanation is that the background estimation is erroneous and there is a systematic contribution from an unknown absorption feature in the probed spectral region. A simple test is to assume that the model predictions are valid for our experiments. The symbols shown in the right panel represent corrected values with an additional systematic error estimate. In the case of ${H_3}^+$ we can subtract the evaluated column number density itself at $F_{D_2} = 0.8$ from all of its values, the models predict an almost zero contribution at this point. For ${D_3}^+$ we can perform a similar operation at $F_{D_2} = 0.2$ using, for example, the 300 K model value as reference. We note that at this F_{D_2} value the uncorrected relative density is slightly negative for ${D_3}^+$. The additional systematic uncertainty is added to the error budget as the value of the shift in the usual root mean square manner, shown as the increased error bars in the right panel of Figure 16.

5.4 DISCUSSION AND CONCLUSIONS

In this chapter I demonstrated the use of data evaluation methods that include a variety of statistical tools and experimental techniques.

In the first part of this chapter I have demonstrated the use of ion vibrational spectroscopy aided thermometry. The neutral gas temperature is estimated from the ion translational and rotational temperature values based on previous experiments and the current findings. This common temperature estimate, show in Table 7, is used for the rest of the analysis, e. g., to extract absolute column number densities of the present isotopologues and through them derive relative ion densities.

In the second part of this chapter I have presented an example of relative ion number density determination of the ${H_3}^+$ isotopologues present in the experiments. This represents the first step towards the experimental evaluation of isotopologue specific recombination rate coefficients in the experiments. An assessment of possible systematic uncertainties in the evaluation procedure have been proposed based on comparison of experimental observations and model predictions.

5.4.1 *Systematic Errors*

A re-examination of the recorded absorption spectra in the region of the ${H_3}^+$ and ${D_3}^+$ lines have revealed broad absorption features that could explain the systematic discrepancies highlighted in Figure 16. The near-overlap of these features with the absorption lines of interest is present in all the available experimental data. We also attempted to reproduce the experiments conducted on the novel apparatus (presented in Chapter 7) with the observations limited to ${H_3}^+$ in a different spectral regions. Assuming that the sum of ${H_3}^+$ isotopologue number densities is constant in the full range of F_{D_2}, we performed a preliminary analysis of the new data that showed significant differences in the evaluated relative H_3^+ ion densities. These findings can directly impact the error estimates of evaluated recombination rate coefficients.

The proposed systematic corrections of the evaluated ion column densities of H_3^+ and D_3^+ in the case of Figure 16 result in a 20 % to 30 % uncertainties in the estimated overall ion number density and also in the relative densities of H_2D^+ and HD_2^+ in the full range of F_{D_2} values.

Following the evaluation procedure of Dohnal et al. 2016, the final error estimate can be derived as follows. The temporal evolution of the overall ion number density is determined by scaling the temporal evolution measurements performed for a single isotopologue by its respective relative ion number density. This way the systematic correction propagates directly to the uncertainty of the determined effective recombination rate coefficient. The statistical uncertainties of fitted values of the rate coefficients are usually lower than 10 %. In the evaluation procedure, the fitted values represent the weighted averages of isotopologue specific effective recombination rate coefficients where the relative ion densities enter as weights. The values for H_3^+ and D_3^+ are determined independently and their weighted contributions are subtracted to get the residual contributions of H_2D^+ and HD_2^+. The uncertainties of relative ion densities again enter the error budget.

The fitted effective recombination rate coefficient values at various F_{D_2} values do not differ more than the individual statistical uncertainties from the mean values for pure H_3^+ and D_3^+. This leads to a combined uncertainty of roughly 90 % for the residual values in the regions with the highest sum of H_2D^+ and HD_2^+ relative densities. To further differentiate between their individual contributions, several more data points are needed at different relative densities, where the errors can exceed 100 %.

The proposed systematic correction due to its unknown error can present itself as an obstacle in the evaluation of recombination experiments. Without reliable relative ion number densities, further evaluation of individual DR rate coefficients for H_2D^+ and HD_2^+ is hindered.

Additional measurements utilising several transitions of all present isotopologues in future experiments would be able to exclude the possible systematic effects. These experiments would allow reliable re-evaluation of the present data and extraction of isotopologue specific recombination rate coefficients.

6

OVERTONE SPECTROSCOPY OF N_2H^+

In this chapter I will present my first, largely independent experimental campaign where I planned, executed and processed the experiments as the principal investigator of the scientific team. The main goal of this experimental campaign was to find a set of overtone ro-vibrational transitions of N_2H^+ suitable for subsequent DR investigations. The requirements for this set of transitions were to be applicable for ion rotational thermometry and absolute ion number density measurements in the temperature range of 77 K to 300 K. An initial analysis of the experimental findings was published in a research article by Kálosi et al. 2017.

Here I present the detailed analysis, also incorporating additional experimental findings and auxiliary measurements. All the experiments were conducted on the basic SA-CRDS apparatus described in Section 4.2.1 with minor modifications in the spectrometer compared to the one employed for the experiments of Chapter 5. This analysis builds also in a large extent on the previous chapter and so only the relevant difference will be examined.

6.1 SPECTRAL SURVEY

In the first part of the data analysis presented in this chapter we will address the question of transition frequency determination and how these data can be used to extract additional structural information about the ions of interest.

The strongest vibrational bands of N_2H^+ are linked to its ν_1 mode. The most easily accessible with our spectrometer and equipment is the ground to $(2,0^0,0)$ transition, classified as a first overtone ($2\nu_1$ band). In the absence of a vibrational angular momentum, this band exhibits a textbook P- and R-branch structure. We can use a combination of molecular parameters from Kabbadj et al. 1994 and Yu et al. 2015 to predict not yet observed transition frequencies in the $2\nu_1$ band of N_2H^+. These predictions greatly simplifies any search for typically narrow (FWHM $\simeq 10^{-2}\,\mathrm{cm}^{-1}$) absorption lines with a high resolution instrument as a cw-CRDS.

Figure 17 shows two simulated spectra of the $2\nu_1$ band that differ by the simulation temperature. These values are the limits of our temperature range of interest. Highlighted are the transitions probed in the experiments presented in this thesis. These are a suitable candidate group for ion absorption spectroscopy aided thermometry.

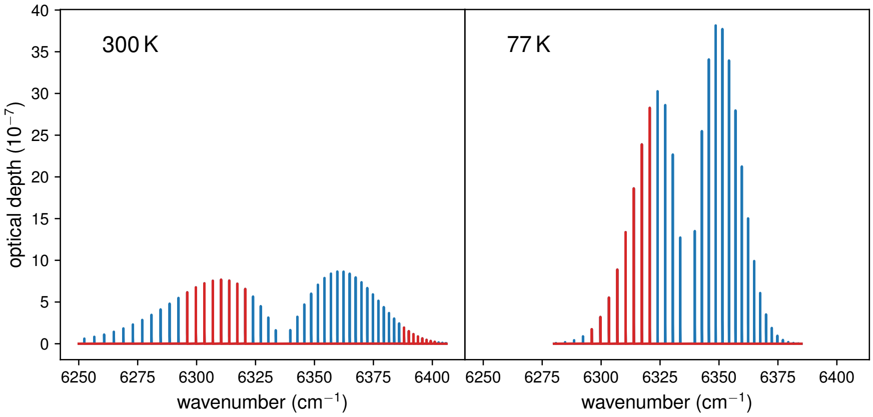

Figure 17. Comparison of N_2H^+ first overtone absorption intensities for two different temperature values. The spectra are calculated for a typical discharge ion number density. The highlighted lines are the transitions probed in the experiments presented in this thesis.

In this chapter we are using the same statistical tools as described in Chapter 5. The N_2H^+ absorption spectra presented here are the product of signal averaging over the nominal discharge period, if not otherwise stated. The actual time period is chosen according to the same rules as previously described.

6.1.1 *Wavemeter Calibration*

The guaranteed absolute accuracy of the wavemeter used in the experiments (see Section 4.3.7) is roughly $12 \times 10^{-4}\,\text{cm}^{-1}$ in the wavelength range of the probed absorption lines. With long enough integration time, we are able to reduce the statistical uncertainty of the centre frequency determination of absorption lines an order beyond this accuracy, even in the case of transient species. We recorded several, calibration grade CO absorption lines in separate experiments in order to check the absolute precision of our wavemeter.

We chose four CO absorption lines listed in the HITRAN database (Gordon et al. 2017; Mondelain et al. 2015), namely the $\text{P}\,(11)$, $\text{P}\,(8)$, $\text{R}\,(15)$ and $\text{R}\,(16)$ ro-vibrational lines of the 3ν band. An advantage of these lines is that the mass of CO is almost the same as of N_2H^+ and so the line profiles have a similar width.

We recorded these lines using the standard CRDS technique without the need for any temporal resolution. The pressure of the gas was set to avoid the accidental saturation of the data acquisition system by driving the photon lifetime too short. In the measurements we easily reached the systematic limits of the spectrometer with the chosen integration time. Only the baseline variation is visible as noise in the data, the relative frequency uncertainty did not manifest thanks to the relatively small signal magnitude. Even though the baseline noise is set by the time spent at each wavelength in this case, the noise distribution itself is still stochastic in nature. The estimated statistical uncertainty of each data point can be still used as a relative weight in the fitting procedure to factor in the actual amount of data points averaged.

The differences between our fitted centre frequencies and the database values are all single sided. The maximum observed difference is $1.5 \times 10^{-4}\,\mathrm{cm}^{-1}$. It is plausible that this value is a function of room temperature or other similar factors. We use it only as an estimate of the systematic errors present in the wavelength determination and it is not intended as a calibration value for the wavemeter measured wavelength values. It can be added to the statistical uncertainty in a standard root mean square fashion.

6.1.2 *Absorption Line Shape*

The presented data analysis closely follows the procedure of Kálosi et al. 2017. One major difference is the line shape function used to fit the recorded absorption spectra. Here we use a combination of Gaussian and Voigt line shape profiles to fit the N_2H^+ transitions with a preference for the Voigt shape when the signal-to-noise ratio is high enough. Additional measurements after the publication of the previous analysis revealed the importance of pressure broadening for the transitions of interest even at room temperature in our experiments. The dataset processed and presented in the course if this thesis is not sufficient to determine the exact pressure-broadened FWHM for a reference pressure and temperature.

Whenever experimental absorption line strengths are determined and used in subsequent data analysis, only the fits by Voigt line shapes are used. Figure 18 shows an example of a fit. Depending on the pressure-broadened FWHM, the difference between fits by Gaussian or Voigt line shapes can be several tens of percent in terms of experimental line strength. Overlapping lines can also cause further systematic errors in the transition frequency determination if the fitted line shapes are only a crude approximation of the recorded transitions. The case and reason of overlapping transitions will be examined after introducing the experimental conditions.

6.1.3 *Signal Optimisation*

Part of the present experimental campaign was to compare the absorption line strengths in different neutral gas mixtures and also to achieve the highest available wavelength precision allowed by the utilised experimental equipment. We used either helium or hydrogen buffered plasmas to generate the N_2H^+ ions. The reactant numbered densities

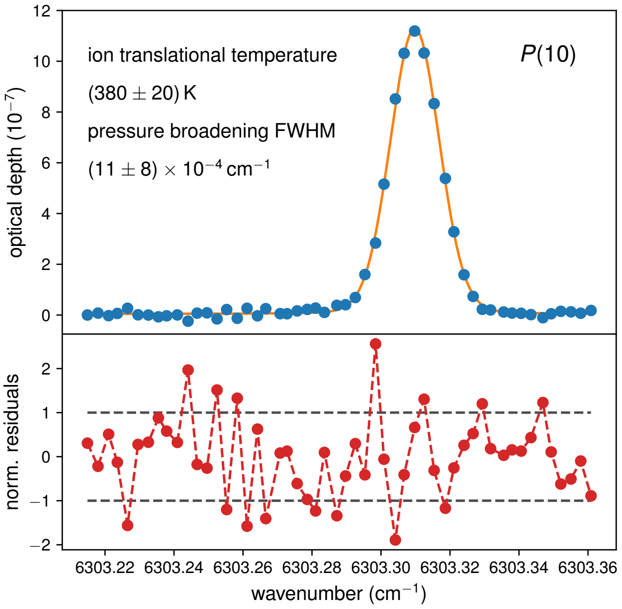

Figure 18. Experimental absorption line shape example. The recorded transition (symbols) is fitted by a Voigt line shape to determine its physical parameters (shown in the upper panel as full line). Experimental conditions were: hydrogen buffered mixture of H_2/N_2 at a total pressure of 250 Pa. The estimated N_2 number density due to the temperature uncertainty is $5 \times 10^{14}\,cm^{-3}$. The measured coolant exhaust temperature is 307 K. The pressure broadened FWHM and the ion translational temperature determined from the fit is indicated in the upper panel. Almost 10 % of the line width is due to pressure broadening. The lower panel shows the normalised residuals of the fit indicating that the estimated statistical uncertainties are consistent with a reliable absolute magnitude.

varied between experiments but the main precursor of the ions was a mixture of H_2/N_2. We also observed at certain conditions the presence of NH_3 molecules, probably a product of molecular synthesis on the surface of the discharge container wall. If unchecked, proton hop from N_2H^+ to these impurities would be able to severely reduce the number of N_2H^+ ions in the discharge. Here we examine only those measurements and conditions where impurity species could be kept well bellow $10^{11}\,cm^{-3}$.

A dominant part of the experiments was conducted in H_2 buffered plasmas at almost room temperature with a total pressure of 200 Pa. We varied the relative partial pressure of N_2 from 1 % to 4 %. We used a relatively high microwave power compared to $H_3{}^+$ experiments in the range 20 W. We filled the cooling bath with vapours of liquid nitrogen to distribute the heat load of the discharge. We also observed a slight increase in the coolant exhaust temperature during the experiments.

A possibly elevated temperature of the buffer gas was aiding us in the search for high-J lines.

Alternatively, we conducted several experiments in helium buffered $He/H_2/N_2$ mixtures. These were recombination oriented and the discharge container was cooled to below room temperatures in the range of 200 K to 300 K. The overall pressure of the neutral gas was 500 Pa with estimated number densities of the H_2/N_2 mixture $[H_2] = 3 \times 10^{14}\,\mathrm{cm}^{-3}$ and $[N_2] = 3 \times 10^{14}\,\mathrm{cm}^{-3}$.

In certain parts of the recorded spectra the absorption lines of N_2H^+ were overlapped with lines belonging to several unidentified electronic transitions of N_2. These overlapping lines were previously observed by Sasada and Amano 1990 and in our experiments had similar line strengths compared to the N_2H^+ lines of interest. Naturally, the H_2/N_2 mixtures were affected most due to the higher nitrogen partial pressure.

The $He/H_2/N_2$ mixtures were also not free from interfering lines, in this case by He_2 transitions. These affected a different region of the absorption spectra. We recorded absorption spectra in both mixture to minimise the uncertainty caused by overlapping absorption lines. The data analysis presented here is limited to the available measurements in the named mixtures.

6.1.4 *Molecular Constants*

The direct result of this spectral survey is a set of experimental transition wavenumbers consisting of 49 values. We recorded several lines multiple times at different experimental conditions. These cover both P- and R-branch transitions, namely $\mathrm{P}(5)$ through $\mathrm{P}(12)$ and $\mathrm{R}(19)$ through $\mathrm{R}(26)$.

We can determine the upper state molecular constants in a liner least squares fit thanks to the high precision ground state constants taken from Yu et al. 2015. In this approach the lower states energy levels are directly subtracted from the observed transitions frequencies. The upper state energies are expressed as a standard power series (see Equation 4) including the effective vibrational energy of the state and rotational constants up to H_{20^00}. All the observed values and their individual error estimates were included separately in the final fit. The change in the chi-square value between fits with and without the H_{20^00} parameter was significant to include it in the final fit. The improved molecular constants of the (20^00) excited vibrational state of N_2H^+ are listed in Table 8.

The determined value H_{20^00} is well in the range of values observed for the ground and higher excited vibrational states. The data collected and used in the analysis by Kabbadj et al. 1994 did not have the necessary precision to determine its value. In this analysis, it was

PARAMETER	SOURCE	
	PRESENT	Kabbadj et al. 1994
G_{20^00} (cm^{-1})	6336.681 17(7)	6336.679
B_{20^00} (cm^{-1})	1.528 373 8(13)	1.528 368(18)
D_{20^00} (10^{-6} cm^{-1})	2.883(5)	2.880(20)
H_{20^00} (10^{-9} cm^{-1})	0.014(5)	–

Table 8. Molecular constants of the (20^00) excited vibrational state of N_2H^+. The values determined in the present analysis are compared to the values of Kabbadj et al. 1994.

possible thanks to the high-J lines of the R-branch and the overall improved precision of the observed transition wavenumbers.

The improved molecular constants of the (20^00) excited vibrational state of N_2H^+ are applicable both to predict not yet observed transitions between vibrational states of this ion and to serve as a benchmark for theoretical studies that aim to calculate ro-vibrational levels of N_2H^+ to a high degree of precision.

6.1.5 *Vibrationally Excited States*

We attempted a search for N_2H^+ ions occupying excited vibrational states. According to Kabbadj et al. 1994, the lowest rotational level of the first excited vibrational state has an energy of 688.373 cm⁻¹. We can expect to have several rotational levels of this excited vibrational state to populated already at room temperature based purely on the Boltzmann distribution of rotational populations. Kabbadj et al. 1994 also reported different excitation temperatures in the thousand kelvin range for each vibrational mode in their glow discharge at similar conditions as in the present experiments. Although we do not expect similar values due to the difference between probable excitation mechanisms in our setup, an upper limit can still be estimated without observing any lines.

In the present experiments we identified several absorption lines belonging to the $(21^10) \leftarrow (01^10)$ band of N_2H^+. Interaction of rotational and vibrational angular momenta due to the degenerate ν_2 mode causes splitting of the rotational levels identified by their parity. Each transitions is additionally labelled by an upper superscript 'e' or 'f'. Figure 19 shows an example of the typical doublet structure of these lines.

No other absorption bands between vibrationally excited states were observed in the present experiments.

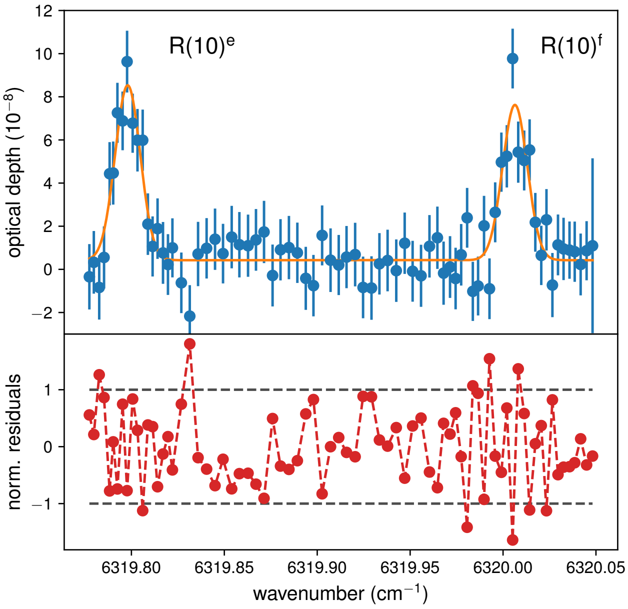

Figure 19. Doublet absorption line example (symbols) of the $(21^10) \leftarrow (01^10)$ band of N_2H^+. The experimental conditions were the same as that of Figure 18. See text for the labelling of the absorption lines. Both lines are fitted simultaneously (full line). Lower panel shows the normalised residuals of the fit.

6.2 LINE INTENSITIES

In the second part of the data analysis presented in this chapter we will once again examine how reliable are the line intensity measurements conducted with our cw-CRDS. This analysis is the first step towards absolute ion number densities and additional plasma diagnostics. Here we will examine one consistent set of measurements conducted in a hydrogen buffered H_2/N_2 mixture at a total pressure of 250 Pa and with an estimated temperature of the neutral gas exceeding room temperature. The estimated N_2 number density due to the temperature uncertainty is $5 \times 10^{14}\,\mathrm{cm}^{-3}$.

Figure 20 shows a comparison of observed and simulated line intensities in the P-branch of the $2\nu_1$ band. The simulation conditions were: temperature of 370 K (same for translational, rotational and vibrational motion), pressure broadened FWHM of $13.8 \times 10^{-4}\,\mathrm{cm}^{-1}$, maximum ion number density of $2.2 \times 10^{11}\,\mathrm{cm}^{-3}$ with a longitudinal profile width of 5 cm.

Figure 20 is an alternative method of how to visualise the rotational population distribution of the ions in the ground vibrational state. In this simulation we assume that the ion population of all the ro-vibrational states is described by one common temperature value. We

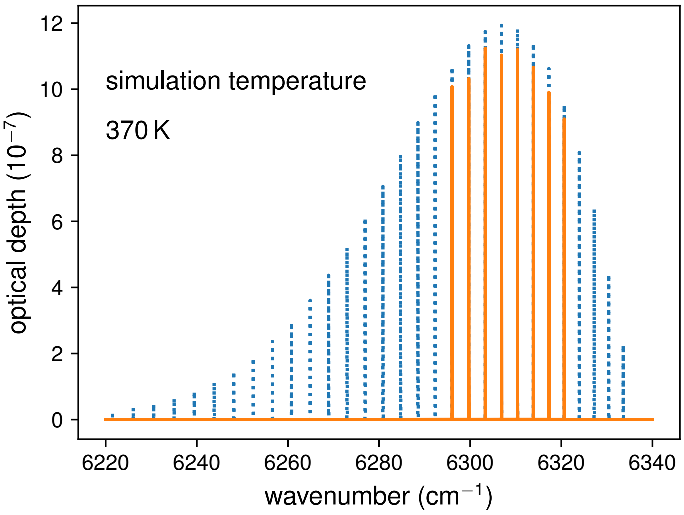

Figure 20. Set of observed absorption line intensities (full lines) compared with simulated lines (dotted lines). See text for the parameters of the simulation.

can derive the absolute number of ions in the vibrational ground state from the presented line intensity measurements but that does not necessarily mean that all the N_2H^+ ions are accounted for. The overall number of ions is the key parameter to recombination experiments. In the following we will examine the question of both rotational and vibrational temperatures in the experiments.

6.2.1 *Rotational Temperature*

In theory the rotational temperature can be estimated separately in every vibrational state. In practice, however, this is not feasible in our case for the simple reason that the observed transitions between excited vibrational states have an order of magnitude lower observed line intensities than those of the $2\nu_1$ band. What we can do instead is to test the assumptions that all probed rotational states obey the same population distribution characterised by a common temperature. All we need for this purpose is a set of Einstein coefficients for the observed transitions.

In a first approximation the rotational (Hönl-London) and vibrational intensity factors of a transition can be separately calculated. In the specific case of the $(21^10) \leftarrow (01^10)$ band we will further assume that its vibrational transition moment is approximately the same as that of the $2\nu_1$ band (shown in Table 3). The calculations of Špirko, Bludský, and Kraemer 2008 indicate that this is a good approximation when compared with similar types of combination bands.

Rotational intensity factors for linear molecules can be calculated based on angular momentum algebra. Here we use the expressions found in (Maki, Quapp, and Klee 1995), also available for transitions between states with vibrational angular momenta.

Combining both factors into the Einstein coefficient of spontaneous emission gives

$$A_{ij} = \frac{64\pi^4}{4\pi\varepsilon_0} \frac{\nu_0{}^3}{3hc^3} \frac{S_R F R_{ij}{}^2}{g_j}, \tag{62}$$

where ε_0 is the vacuum permittivity, S_R is the rotational intensity factor and R_{ij} is the vibrational transition dipole moment. The Hermann-Wallis correction term F can be also included to account for the interaction between rotational and vibrational motion. Here we neglect this term due to the limited precision of the measurements.

Figure 21 shows the observed intensities divided by the state dependent part of Equation 42. This leaves only the exponential parts of the temperature dependence. The plotted values are also normalised to unity maximum for the state with the reference energy (lowest rotational state). The normalisation value is determined in the fit by the exponential function. The rotational temperature, i. e. the fit, is evaluated only from the ground state values.

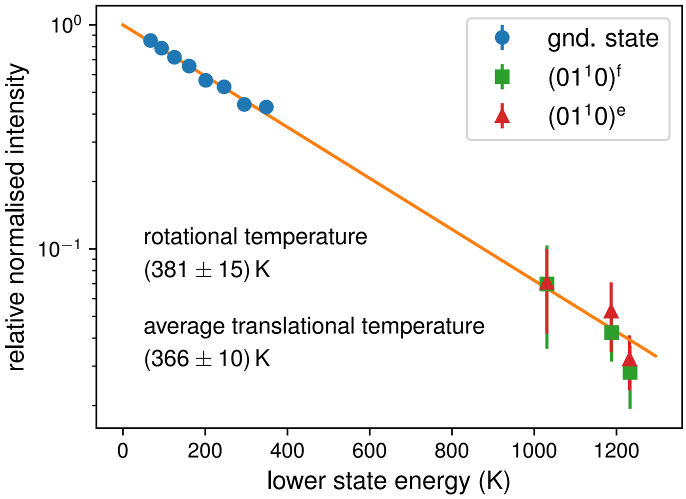

Figure 21. Observed relative intensities of N_2H^+ transitions derived from the fitted absorption lines. They are plotted as a function of lower state energy relative to the lowest ro-vibrational state. They are also normalised to unity maximum of the lowest energy state, the normalisation constant is derived from the exponential fit. The rotational temperature, i. e. the fit, is evaluated from the ground vibrational state values only. Its value is shown in the figure together with the average translational temperature evaluated from the Doppler width of the corresponding absorption lines.

As we can see in Figure 21, the excited state values do not differ significantly to falsify our assumption about a common temperature value of both the vibrational and rotational temperatures. Furthermore, the average ion translational temperature evaluated from the $2\nu_1$ transitions agrees well with the rotational temperature value within the quoted uncertainties. The difference between the measured coolant exhaust and the observed ion temperatures can be explained by the larger then usual microwave power used in the experiments. A substantial flow of excited species can lead to elevated temperatures of the discharge container wall. This difference also implies a gradient of the neutral gas temperature. The presented ion temperature values are interpreted as line-of-sight averages over the overlap of the 2D density distribution and the probing laser light in the cavity.

With a rotational temperature in hand we can estimate the ion number density. This can be done based on the assumption that both observed vibrational states are characterised by a common rotational temperature or by assuming that all the ro-vibrational states are characterised by a common excitation temperature. In the presented case the two approaches are practically the same.

6.2.2 *Vibrational Temperatures*

The fact that we did not observed any absorption lines belonging to transitions between higher excited vibrational states does not restrict us from estimating an upper limit for the population of these states. According to Kabbadj et al. 1994 the lowest ro-vibrational state having one quantum in the ν_3 mode has an energy of 2257.873 cm^{-1}. This particular vibrational mode can be characterised as an N−N stretch and has a similar fundamental frequency compared with the vibrational mode of N_2.

The $(20^01) \leftarrow (00^01)$ vibrational band of N_2H^+ has several transitions in the same spectral region as the bands probed and observed in the experiments. We performed spectral measurements in the region of predicted transition frequencies without positively observing these transitions. Given the experimental accuracy of the measurements we can estimate an upper limit of the population of several ro-vibrational states with vibrational quantum numbers (00^01).

We once again assume that the vibrational transition moment of the $(20^01) \leftarrow (00^01)$ band approximately equals that of the $2\nu_1$ band. This gives us an upper limit of 1.5 % relative to the observed number of ions. A vibrational temperature estimate from the ratio of relative populations of the ground and (00^01) states would underestimate a possible tail of vibrational state populations. Instead, the upper limit of the relative population of the (00^01) state can be used to estimate the overall systematic error in the determination of the N_2H^+ number density.

6.3 DISCUSSION AND CONCLUSIONS

In this chapter I have presented the first experimental campaign in which I planned, executed and processed the presented experiments as the principal investigator of the scientific team. The goals of this campaign were to find a suitable list of ro-vibrational transitions that can be used to estimate rotational, vibrational and translational temperature of the ions and using this information estimate the overall column number density of N_2H^+ in the experiments. These conditions were satisfied as the presented results implies. I have demonstrated a general data processing approach that can be used in successive DR experiments.

Additional results of this study include the improved molecular constants of the (20^00) excited vibrational state of N_2H^+. These are applicable both to predict not yet observed transitions between vibrational states of N_2H^+ and to serve as a benchmark of theoretical studies that aim to calculate ro-vibrational levels of N_2H^+ to a high degree of precision.

Further auxiliary studies were planned to run parallel with the presented experiments. These additional experiments aimed to systematically study the source of gas heating and the pressure broadening effects. Both play a key role in the precision of planned DR experimental campaigns. Some of these findings of auxiliary measurements have been already incorporated in the present data analysis as compared to the preliminary analysis by Kálosi et al. 2017. At the time of this thesis, these new findings have not yet been published and will probably appear as the part of a final DR experimental campaign.

Part III

CRYOGENIC CONDITIONS

Where we find out how to approximately simulate cold interstellar environments and similarly cold experimental plasmas.

7

A CRYOGENIC STATIONARY AFTERGLOW INSTRUMENT

The basic idea behind the decisions that lead to the construction of this new apparatus was to create a Stationary Afterglow (SA) configuration which can be cooled down to temperatures as low as 30 K by a single cryo-cooler and allow for temporally resolved laser absorption diagnostics of afterglow plasmas. We were able to realise this idea thank to the fact that in our laboratory there was a cryo-cooler available and the team of experts responsible for the design have had previous experiences with cryogenic instrumentation and also laser absorption spectroscopy. All in all, a direct consequence of the resources available was the limitation in size and also the type of discharge generation chosen in the final design.

To start with a short summarising description, the apparatus consists of a sapphire discharge tube surrounded by a cylindrical microwave resonator. All these parts are actively cooled by a helium cryo-cooler and are housed in a thermal insulation vacuum system. Figure 22 shows a schematic representation of the apparatus. Divided into sections, we will discuss the problems faced during the design of the subsystems of the apparatus. The employed laser absorption spectrometer is discussed at the end of this chapter. Compared with the complexity of storage rings the described setup might feel overly simplified but that is also one of the advantages of the afterglow techniques. A tabletop design should be both flexible and open for changes in the future.

7.1 INSULATION AND EXPERIMENTAL VACUUM

The overall vacuum system consists of two separate parts, an experimental gas handling and an insulation vacuum system. Working pressures of the former are hundreds of pascal with mass flows of the gas above $0.2\,\mathrm{Pa\,m^3\,s^{-1}}$, these are the typical parameters for a SA setup. We also estimated the conditions for good thermal insulation and set a goal to achieve a vacuum better than 10^{-1} Pa. As we can see, the experimental conditions set certain criteria for the vacuum tightness of the sapphire to metal transition while these parts need to handle repetitive cooling, temperatures gradients and thermal contraction of the system.

A straightforward solution was chosen for the final design of the sapphire to metal transition. The parts used on both ends of the discharge tube are identical. The stainless steel part starting from

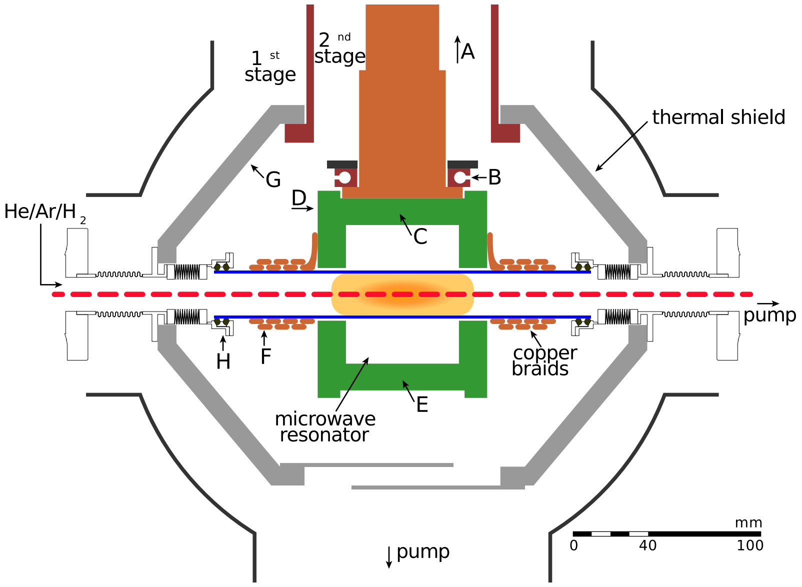

Figure 22. Technical schematics of the cryogenic SA-CRDS. Capital letters A to H denote the placement of the temperature sensors. Sensor A is placed on the 1st stage of the cold-head. Adapted from Plašil et al. 2018.

one end has a standard CF flange followed by a pair of formed and edge welded bellows (in this order) ending with a custom designed connection for the transition. Between the bellows a flat piece with clearance holes for bolts is situated that is directly connected to the thermal shield. The welded bellow inside the cryogenic region compensates for the contraction of the discharge tube and also the small misalignment between the thermal shield orientation and the tube axis. The formed bellow thermally decouples the cryogenic and room temperatures parts and offers additional flexibility to the whole system. The custom designed end of the metal part has a slightly larger inner diameter then the sapphire tube to fit in the sealing parts. These consist of a pair of fluoroelastomer (Viton®) O-rings that fit tightly on the sapphire tube and a small stainless steel ring between them, specially shaped to accommodate the form of the O-rings. A final ring piece closes the connection with the same inner shape as the fixed main part. The inner O-rings, from the perspective of the discharge container, stabilise and the outer O-rings seal the connection. During construction two additional one millimetre thick rings were added to both ends to increase the sealing force. This system turned out to provide compatibility with high vacuum conditions. During cryogenic operation the pressure in the insulation vacuum chamber routinely reaches the 10^{-5} Pa level without bake-out, thus achieving our goal set for satisfactory insulation vacuum condition.

The insulation vacuum system consists of the main chamber, a cross piece and a straight section leading to a turbomolecular pump. The main chamber houses all cryogenic parts including the cryo-cooler. Several utility and diagnostic ports are available in the upper side of this chamber. A compact FullRange™ Bayard Alpert type gauge (PBR 260) monitors the pressure in the chamber. Three electrical feedthroughs serve for temperature sensor read-out and heating elements connection. A separate SubMiniature version A (SMA) type electrical feedthrough bridges the microwave power pathway. An optical feedthrough for an optical fibre connection is also available, currently not in use. Now following the axis of the discharge tube one side of the main chamber is closed by a special flange with additional double sided CF flanges that hold one of the transition pieces. The opposite side of the chamber is connected to a large cross piece that is in turn closed by a similar flange as the main chamber. This cross houses a nipple that prolongs the inner vacuum system connecting the transition piece to the end flange. Another side of the cross leads to a butterfly valve and a small turbomolecular pump for vacuum generation of the insulation system only.

The last missing pieces of this description are all part of the room temperature experimental vacuum system. A smaller cross piece extends the main chamber side of the system. A Baratron® capacitance manometer, an angle valve, a bypass connection with the main chamber and one of the mirror holders are connected to this cross. The gas pressure during the experiments is measured exclusively at room temperature. The angle valve is used to regulate this pressure leading to a Roots type blower through a series of additional bellows and nipples. The bypass connection equipped with a ball valve is closed during experimental operation and only serves to equalise the pressure during venting of both vacuum systems. The mirror holder function will be explained in Section 7.5. Its pair lies at the other end of the experimental vacuum system past the insulation cross piece. The experimental cross piece has one additional free side reserved for the optional connection of an independent turbomolecular pump.

7.2 CRYOGENICS

The heart of the cryogenic operation is a Sumitomo RDK-408S two-stage cold-head. The first stage cools the thermal radiation shield and the second stage cools the microwave resonator and the discharge tube. A silver coated copper cylindrical interface prolongs the first stage of the cold-head and holds the upper parts of the thermal shield. A modular solution was chosen to allow for assembly of the cryogenic parts inside the main insulation chamber. The thermal shield consists of four identical supporting pieces that hold the construct together, two upper and lower parts. The sides of the shield are closed by additional flat pieces. A pumping opening is located at the bottom of the shield. The microwave resonator also consists of two identical pieces, upper and lower.

The microwave resonator has a cubic shape from outside with circular openings from two sides that expand into a cylindrical volume. More on the design of the resonator can be found in the following section. The length of the resonator cube edge is 9.6 cm and the opening is slightly larger than the discharge tube with an outer radius of 12.6 mm to accommodate for thermal contractions. Heat transfer between the resonator and the discharge tube is mediated by silver coated copper braids wrapped over several turns and anchored on the body of the resonator. The discharge tube itself is fully held in place by the metal to sapphire transition elements and the braids provide only additional mechanical support. The length of the sapphire tube is 20 cm with a wall thickness of 1.3 mm.

Cartridge heaters placed inside the body of the resonator and a copper ring around the second stage of the cold-head allow for controlled heating even at cryogenic temperatures. This method is applicable only at the lowest temperatures up to roughly 80 K. Above this temperature the heat capacity of the resonator is sufficiently high for slow, controlled heating-up and allows us to perform measurements in this higher temperature range.

Overall eight temperature sensors are placed at various key points of the cryogenic parts: three silicon diodes (DT-471-CU, absolute accuracy 1.5 K or 1.5 % of temperature, whichever is greater) and five platinum Resistance Temperature Detectors (RTDs) with values of 100 Ω or 1 kΩ. Only the diode sensors are monitored using a four-lead measurement scheme. The RTDs accuracy in our configuration is slightly worse than the Class B industry standard (DIN IEC 751). Sensor connecting wires are thermally anchored at the thermal shield.

Figure 23 shows a test record of key temperature evolutions during cool-down and warm-up of the apparatus. The thermal shield is the first to reach stable temperatures around 30 K varying slightly due to changes in the cold-head power. This is followed by the second stage of the cold-head, the coldest spot, below 10 K, of the setup. Sensor B is placed on a copper ring clamped around the cold-head body. Next follow the resonator (upper part), the discharge tube and the sealing connection of the metal to sapphire transition. Naturally the resonator body reaches the lowest temperatures of the three measurement points but overall the temperature differences are small compared to the second stage of the cold-head. The most probable reason is the decrease in thermal conductivity of the resonator alloy around 20 K. On the other hand, the almost equal temperatures at these key places point to the efficient cooling of the discharge tube. The platinum RTDs designated as F and H are used to estimate the discharge tube temperature during measurements. Sensor F is attached from the outer side to one of the copper braids and sensor H is fixed to the end piece of the tube holder element.

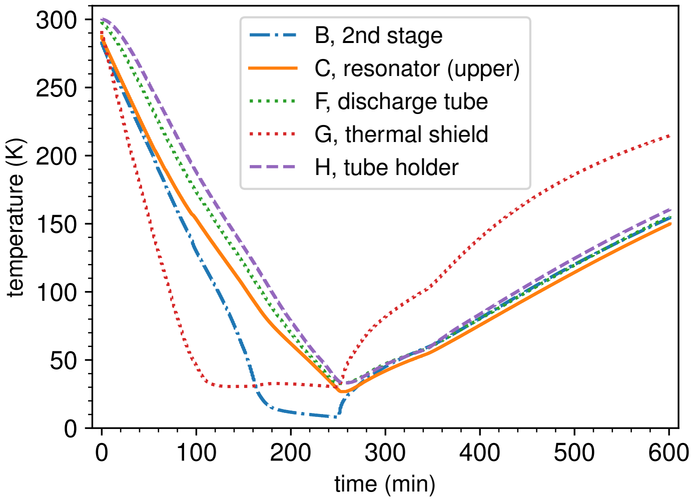

Figure 23. Temperature evolution of the apparatus during cool-down and warm-up. Only readings from key temperature sensors are shown for better visibility. See text for further explanations.

As discussed previously, the transition element has a thermal contact with the shield between the two bellows. The temperature readings further indicate that the end piece must have a thermal contact with the discharge tube. From this we can conclude that the gas flowing into the cryogenic region is pre-cooled prior entering the discharge region. Simple thermal conductivity models show that the length of the cold discharge tube is sufficient to efficiently cool the gas to the same temperature at the mass flows used in the experiments. Furthermore, the temperature increase of the gas by the heat absorbed in the active discharge also depends on the flow rate. These effects were studied during commissioning of the apparatus.

7.3 MICROWAVE CAVITY

The basic requirements for the design of the microwave cavity were the following: provide a nearly homogeneous plasma column excited by microwave power in the frequency range of 2.4 GHz to 2.6 GHz. The final dimensions of the cavity were calculated to provide a resonant frequency of roughly 2.45 GHz with the sapphire tube inserted, resulting in the inner radius of 36.8 mm and length of 60 mm and openings with a radius of 14 mm and length of 18 mm. The following text describes the details of the calculations supervised by Dr. Štěpán Roučka.

The mode of the cavity was chosen to result in the smallest possible dimensions: TM_{010}, where the ordering of the mode indices are axial, radial and azimuthal, respectively. This mode is characterised by a homogeneous electric field on the axis of the resonator and have been frequently employed for both plasma diagnostics and generation (Agdur and Enander 1962; Beenakker and Boumans 1978; Rosen 1949). The resonance frequency of a closed cavity containing a dielectric tube can be calculated analytically (Li, Akyel, and Bosisio 1981). With the additional openings on the sides of the resonator advanced numerical methods are required. We employed the equivalent circuit finite difference time domain method (Gwarek 1985; Rennings et al. 2008) as implemented in the openEMS software (Liebig et al. 2013) to calculate the resonant frequency of the cavity with an arbitrary geometry. The geometrical model included both the cavity and the discharge tube on a three-dimensional cylindrical mesh. In the assembled configuration the microwave field is excited by a loop antenna. This is approximated in the model by a Gaussian pulse with a mean frequency of 2.5 GHz and 20 dB bandwidth of 0.4 GHz applied to an area near the cavity wall. The antenna loop and the final calculated electrical field amplitude is shown in figure Figure 24. Perfectly matched layer boundary conditions were used outside the cavity. Finally, we obtained the resonant frequencies by harmonic inversion (Mandelshtam 2001; Mandelshtam and Taylor 1997) of the recorded time dependent electric field amplitude near the centre of the cavity as implemented in the Harminv software[1]. We benchmarked the time steps and the mesh spacing of the numerical calculations by comparing the values obtained for closed cavities with the analytical model to a precision of 1 MHz. Considering manufacturing tolerances the final resonant frequency could be predicted in the range of (2.475 ± 0.050) GHz at room temperature. Taking into account thermal contractions of the system and change in sapphire permittivity, the predicted resonant frequency around 30 K is in the range of (2.495 ± 0.050) GHz. The measured frequencies at the corresponding temperatures are 2.434(1) GHz and 2.458(1) GHz, respectively, in good agreement with the calculations.

All the above described calculations hold in the case of a non-absorbing dielectric medium, such as a sapphire discharge tube. On the other hand, a real plasma will have its own side effects on the frequency characteristics of the resonator, causing further shift of the resonant frequency and lowering of the quality. A fully self-consistent model of the time-dependent electric field in the resonator would need to include all these effects and many more discharge processes, such as metastable dynamics and plasma chemistry. In this thesis we consider only effective ionisation rates to model the spatial distribution of electron and ion number densities. Based on the magnitude of the resonant frequency shift caused by the electrons we estimate the maximal electron number density that can be continuously maintained in the centre of the resonator to be in the range of $10^9\,\mathrm{cm}^{-3}$ to $10^{10}\,\mathrm{cm}^{-3}$.

---

[1] Harmonic inversion implemented by S. G. Johnson, `https://github.com/stevengj/harminv` (January 8, 2018)

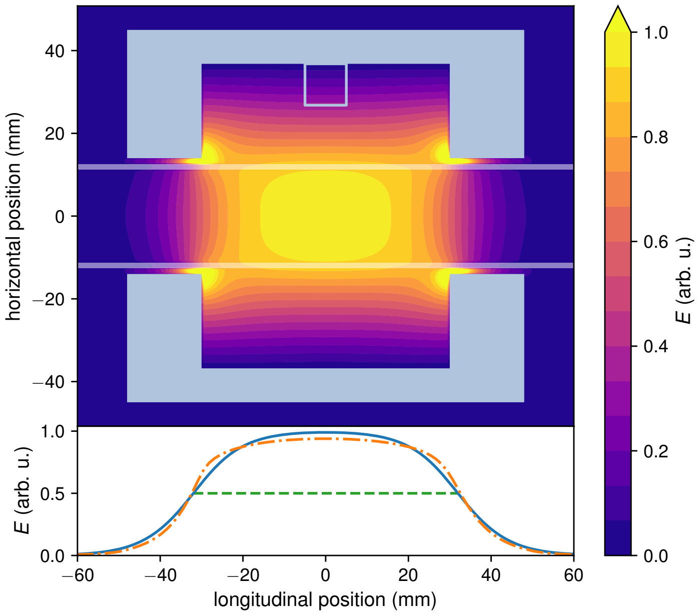

Figure 24. Calculated amplitude of the TM_{010} electric field in the microwave resonator. The upper panel shows a horizontal cut along the common z-axis of the cavity and discharge tube system. The electromagnetic field is excited by the loop highlighted in the upper part of the plot. The lower panel shows a cut along the symmetry axis (full line) and a second cut near the discharge container wall (dash-dotted line). The Full Width at Half Maximum (FWHM) of the field, highlighted by the horizontal dashed line, is close to the actual cavity length. Partially adapted from Plašil et al. 2018.

7.4 MICROWAVE POWER SOURCE

The microwave power to the cavity is delivered by a custom built source consisting of commercially available solid-state devices. Basic requirements for this source were: frequency tunability in the range of 2.4 GHz to 2.6 GHz, several watts of output power and switching functionality in a few microseconds.

The microwave power chain consists of a frequency synthesiser, an absorptive PIN-switch, a coaxial circulator and a band-specific high power amplifier. These devices have SMA connectors at their respective inputs or outputs and microwave power propagation between them is mediated by commercial cable assemblies or adapters.

The frequency synthesiser has a fixed power output level in the whole tuning range of 2.4 GHz to 2.6 GHz. It is equipped with a digital interface and the frequency change is computer controlled with a smallest step of 1 kHz. It is designed for single frequency operation and sweeping is not available.

The absorptive switch is controlled by a single digital timing signal. Switching speeds for both directions are faster than 200 ns. In the ‘OFF’ state it has an isolation of more than 80 dB.

The band-specific amplifier has a manufacturer declared working range of 2.4 GHz to 2.5 GHz. Its amplification decreases slowly above this range and can effectively cover the full range of the frequency synthesiser. With a constant amplification of roughly 40 dB it can deliver up to 40 W of continuous power in the specified range.

During standard operation the synthesiser is active at all times at a set frequency. The same is true for the band-specific amplifier. The final output power of the source can be varied by exchanging fixed coaxial attenuators placed between the synthesiser and the switch. We can estimate the maximal possible output power in the 'OFF' state of the whole amplification chain by taking into account only the active devices, this worst case estimate is roughly 1 µW. Considering the additional attenuation caused by the fixed attenuators, the losses at each inter-connection and each element, the actual narrowband power propagating from the synthesiser and reaching the amplifier results in an output power on the nanowatt level. This was also confirmed by a simple measurement of the 'OFF' state power output using a spectrum analyser which showed only a broadband power spectral density. The overall power measured by a broadband diode power detector was roughly 200 nW. Even if this full power would be absorbed by the electrons in the afterglow (typical on axis number density of 10^{10} cm^{-3}, 10^{11} electrons in total), the increase in electron temperature compared to the buffer gas would be negligible. Moreover, due to the high quality of the resonator most of the power outside the resonance frequency would be reflected to the source. This resonant system is further damped by the combination of a coaxial circulator and an ohmic load attached to the output of the power source. Alternatively, the load can be exchanged by a sensitive and time-resolved power meter. Standard 'ON' state output power of the microwave source lies in the 5 W to 25 W range.

Monitoring of the reflected power revealed us the excellent pulse-to-pulse stability of this power delivery system. Although the impedance of the microwave resonator is most likely not 50 Ω, impedance matching of the combination of the transmission line and the actual resonator to the source turned out not to be a prerequisite of successful discharge operation. It is also not a trivial task, since it is equally possible to end up with the majority of the output power absorbed in the transmission line. A simple two-stub impedance matching circuit is available as part of the transmission line if needed.

7.5 CAVITY RING-DOWN SPECTROMETER

The primary diagnostic tool of the described experimental apparatus is a laser absorption cw-CRDS, similar to the case of our previous SA-CRDS. A simple optical scheme of the setup is shown in Figure 25. Our own experience proved it to be a both reliable and relatively straightforward tool to be used for ion and transient species absorption spectroscopy. Simple estimates of the temporally-resolved absolute absorber number density can be easily extracted from the measured Ring-down (RD) decays. However, special care has to be taken when the characteristic time of the RD signal is not orders of magnitude shorter than the that of typical changes in absorber number density. This can be the case, when a relatively high sensitivity is required due to low absorption signals. The estimated maximal ion number density in the active discharge led us to a higher sensitivity design compared to our previous setup. This section describes the technical details of the spectrometer leaving the examination and the proposed processing of the expected absorption signal for Section 8.3.

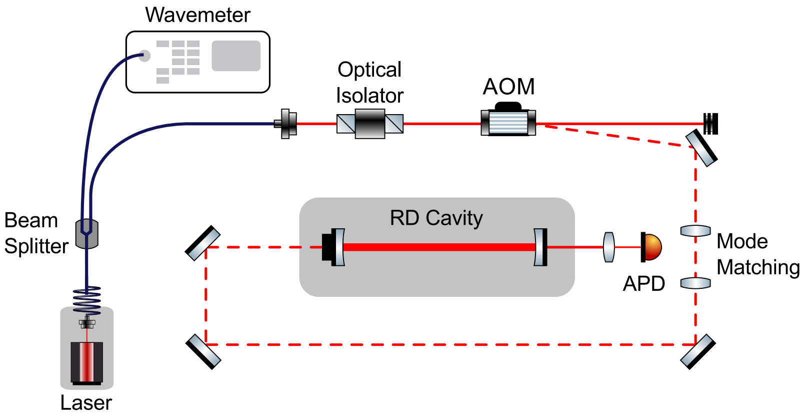

Figure 25. Optical schematics of the employed cw-CRDS. The distances are not up to scale. The mirrors forming the optical cavity are contained in the experimental vacuum, as described in the text.

Main technical parameters of the employed CRDS setup are the following. The optical cavity is formed by two identical planoconcave high-reflectivity mirrors (Layertec Laser mirror 106978) with a curvature of 1000 mm and separated by a distance of (840 ± 5) mm. The highly-reflective dielectric coating of the concave side has a reflectance, $\mathcal{R}$, higher than 0.999 98 in the spectral range of 1250 nm to 1450 nm. The planar side has an anti-reflective coating in the same spectral range. The diameter and thickness of the mirrors is 7.75 mm and 4 mm, respectively. These parameters are important for the estimation of additional power losses in the cavity due to its finite size and for the calculation of characteristic frequencies of possible parasitic optical resonators. Some CRDS designs made use of the natural mechanical vibrations of the constructions to modulate the length of the cavity. In our case, it can be additionally modulated by a linear piezo actuator mounted on one of the mirrors.

As mentioned in Section 7.1, the mirrors are located at the ends of the straight section of the apparatus. Our custom designed vacuum mirror containers allow for fine tuning of the orientation of the respective mirror planes. The actual body of the mirror containers is split by a welded bellow to a connection piece and the main holder part. This lends further flexibility to the design and provides partial vibration isolation from the main experimental chamber. One of the mirror containers has an additional electrical feedthrough on its main part for the connection of the piezo drive voltage. Both containers are shut close by vacuum viewports accommodating wedged and anti-reflective coated windows. The input gas line is connected to the piece holding the piezo mounted mirror slightly upstream from the formed below. This way the mirror is not in the direct way of the incoming gas flow. The second mirror is exposed to unwanted micro-particles that can be formed in the discharge or on the discharge container walls and carried away in the gas flow. Special care has to be taken when working with gas mixtures able to form such particles, especially carbon containing gases. The symmetrical pair of the input gas line located at the second mirror is used for an additional high pressure transducer (working range starting from several kPa).

The positions of the mirrors are not symmetric in respect to the centre of the microwave resonator, meaning that the overlap of the trapped optical field and the plasma column is in the slightly expanding region of the radial beam profile.

The remainder of the description can be split into laser source, detection and electronic signal processing. Starting in this order, we have one fibre-coupled DFB laser diode and one free space ECDL at our disposition in the spectral range of the high-reflectivity mirrors. We unified the optical setup by coupling the ECDL into a multi-mode optical fibre. We operate one laser at a time by exchanging the fibres leading to the compact optical bench. The laser power is first split between a scanning Michelson interferometer-based wavemeter (EXFO WA-1650, ±0.3 pm absolute accuracy) and an output collimator. An optical isolator can be optionally placed between the laser and the fibre splitter for additional isolation against optical feedback. The usual elements of a CRDS setup are mounted on a compact optical bench. These are an AOM for fast incident power switching, and a pair of lenses and a set of mirrors for coupling of the laser beam into the cavity. Due to the roughly twenty times narrower cavity transmission peaks of the current configuration compared with our previous setup (see Equation 51), we decided to leave out the optional pinhole to maximise the available incident laser power.

We employ the same detection scheme of the transmitted power of the cavity as in our previous setup, a negatively biased, fast InGaAs Avalanche Photodiode (APD) in combination with a low-noise transimpedance amplifier. These detectors are employed for their highly linear response. Important to mention that the dark current of an APD can result in a comparably large offset in the measured output signal. The timing, triggering and data acquisition electronics were also adapted from the earlier setup. The analogue output of the detector is split between a National Instruments data acquisition device (PCIe-6251, 1.25 MHz maximum sampling frequency) and the digital triggering circuitry. When the power signal reaches a certain threshold the RF driver of the AOM receives a switch off signal initiating the end of the power build-up in the optical cavity and the recording of a RD event. Sampling of the analogue waveform starts only after the power signal reached the second, lower threshold. The length of the acquired waveform is also fixed. The digital timing signal for the microwave power source (PIN-switch) is also counted by the data acquisition device at the same frequency and serves as the synchronisation and time reference signal, i. e., each RD event is assigned a time parameter relative to the beginning of each discharge cycle.

First operational tests of the cold-head and the spectrometer revealed us that the amplitude of the mechanical vibrations caused by the actual cold-head movement at the mirror positions is comparable with that of the piezo modulation. This turned out to be impossible and also unnecessary to damp. In the absence of a regular length modulation pattern we rely on the natural and random vibrations producing sufficient number of RD events for signal integration. Proposed improvements in the detection scheme are discussed in Section 8.3.

8

COMPUTER SIMULATED EXPERIMENTS

In this chapter I will present some of the technical details of data processing that will help us identify the sources of possible systematic effects and errors, examine the validity of key assumptions and give an estimate of the overall systematic uncertainty of the employed diagnostic method. Although, it may seem to be confusing first why this chapter is placed after two other chapters already dealing with processed data. The answer lies in the challenges presented by our novel experimental instrument described in Chapter 7. In other words, most findings of this chapter have a considerably larger effect on future experiments conducted using the presented apparatus but nevertheless are applicable retrospectively for previously obtained data. In this sense, this chapter is the collection of valuable data processing experiences and a guide for future experimentalists looking for a systematic approach. We tend to forget what can be directly measured is, in best cases, some electrical signal and it is thanks to a mathematical model that we can interpret the results as scientific findings. Some of the topics covered here are plasma modelling on a 2D spatial grid, simulation of CRDS data acquisition and numerical methods of data extraction.

8.1 PLASMA IN CODE

The purpose of plasma modelling is simple, we use some diagnostic techniques to observe important physical properties in plasma experiments and are looking for a way how to interpret these findings in terms of other physical quantities, e. g., DR rate coefficients in our specific case. In this section we focus on the very core of the experiments, i. e., the plasma, where it all actually comes to life.

Throughout Chapter 3 we introduced several partial plasma chemical models, e. g., the isotopic collision system of $H_3^+ + H_2$. The results shown there, as in Figure 4, are actually a solution of the underlying system of differential equations. We assumed steady state of the collision system, i. e., where the time derivatives equal zero. Finding a solution for this (generally stiff) non-linear equation system is the core numerical task in chemical modelling. One further simplifying assumption made in those calculations was that the p_2 fraction is just a parameter in the calculations. This is actually a frequently applied assumption. The neutral reactant number densities are assumed not to be affected by the chemical processes.

In this section we will focus mainly on a plasma chemical model solved on a 2D spatial grid. Its purpose is to predict the longitudinal profile of the plasma column density in various experiments, i. e., its dependence on physical parameters. The proposed model includes both major chemical processes and calculation of ambipolar diffusion independent of analytical approximations. The chemical part can be always enhanced by adding more and more processes and species but this leads to computationally demanding simulations. For an advanced chemical approach, purely time dependent models can be considered by approximating the temporal effects of ambipolar diffusion.

8.1.1 *A Spatial Approach*

First we examine the tools at our disposal, i. e., how to solve a non-linear Partial Differential Equation (PDE) similar to Equation 19. Our initial approach may be to drop any chemical reaction from the system of equations and instead solve Equation 24.

What we are mathematically dealing with in our 2D modelling efforts is nothing else than solving mostly non-linear PDEs with zero Dirichlet boundary conditions[1] for a given set of initial conditions. Thanks to the actual periodic nature of the discharge/afterglow cycles the initial value problem can be turned into a condition of self consistency, keeping in mind that most models employed here should be considered crude approximations to reality and self consistency is relevant in terms of the model only.

Turning our gaze back to the simplified PDE and following the discussion in Section 4.2.2 we can demonstrate the effect of longitudinal diffusion by considering a typical experimental case. The parameters of the exemplary model are listed in Table 9, divided into two sets. The first three are the fixed geometrical parameters of all models, the radius and length of the discharge container and the width of the microwave resonator that can be used to derive, e. g., the FWHM of some initial longitudinal profile. The second set consists of variables of the model, like the typical experimental values of He buffer gas pressure and temperature. The ambipolar diffusion coefficient D_A is calculated using Equation 32 for ions of mass 3 u with a temperature-independent elastic collisional rate coefficient ($4 \times 10^{-10}\,\mathrm{cm}^3\,\mathrm{s}^{-1}$) and the case that the ion and electron temperatures equal the buffer gas temperature.

In fact these parameters are listed for future reference only. The purely diffusion equation for a constant ion and electron temperature is linear and does not depend on the absolute values of the parameters listed. Radial profiles are also not needed to be considered thanks to this linear behaviour, the two directions are independent of each other. The calculated longitudinal profiles of plasma density are normalised

---

[1] Values of the calculated quantity fixed to zero at the boundaries.

PARAMETER	VALUE
Radius	11.3 mm
Length	200 mm
Width	60 mm
Temperature	50 K
Pressure	350 Pa
D_A	$14\,\mathrm{cm^2 s^{-1}}$

Table 9. Major parameters of the longitudinal diffusion model.

by the maximum and time is calculated in units of the characteristic time of the ground mode ambipolar diffusion τ_A (Equation 26). The longitudinal position could be also normalised by, e. g., some equivalent width, but we give an exception in this case. Figure 26 shows these calculated longitudinal profiles for two different initial conditions with the same integral area and for three different times each, at the initial time, and after one and ten times τ_A, respectively. The initial profiles are flat-top and Gaussian for the left and right panels, respectively. Why these two cases are considered will be discussed later in the chapter.

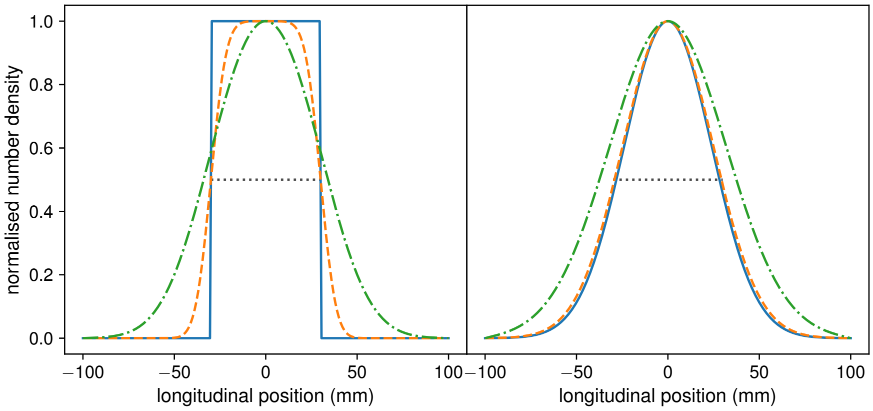

Figure 26. Calculated evolutions of the longitudinal profiles of normalised plasma number density for flat-top and Gaussian initial profiles. The initial profiles (solid line) are propagated in time by considering pure ambipolar diffusion only. This is done by numerical decomposition of the initial profile into the cosine base functions of the analytical solution. The time cuts are one τ_A (dashed line) and ten times τ_A (dot-dashed line) of the ground mode. The horizontal dotted line shows the width of the microwave resonator.

The flat-top profile experiences the largest change in shape while the Gaussian one is already a good approximation for the seemingly infinitely long longitudinal space. Even though we are calculating the time dependent profiles in terms of the solutions of a finite space with boundaries, unless the particles reach those boundaries, the particular solutions behave similar to that in the infinitely long case. One could argue that even if the particles reach the boundaries of the simulation, the change in geometry of the actual experimental configuration, e. g., an increase in radius after the end sections of the discharge container, can be well approximated by zero Dirichlet boundary conditions. Furthermore, in this case we also neglect the breakdown of the modelled plasma at critically low number densities. The validity of quasi-neutrality in the full model is discussed later. This analytical approach is used only to introduce and benchmark the final model.

Our next step in order to connect the profiles to our laser absorption diagnostic technique is to evaluate the line-of-sight integrated column number density, or more specifically how to reverse this process. We could have started with integrating over the longitudinal direction before solving Equation 24 thanks to the linearity of this equation, but there are certain preferences to interpret the measured column number densities in terms of volume number densities, e. g., at the maximum of the profile. The actual reason for this will be explained once we include recombination in our models.

One could also argue that in the afterglow, especially at low temperatures, ambipolar diffusion plays a minor role on the time-scales of the observable electron-ion recombination, but such an argument has actually a major impact on the estimated profiles in the afterglow. This will be again demonstrated once we include recombination in our models. And the answer to why should we consider ambipolar diffusion at all in the role of profile shaping is simply the discharge, where hot electrons promote this process to be a dominant player.

For most reasonable analytical profiles the relation between the maximum and the area is well defined. In case of an ideally flat-top profile the FWHM or simply the width is the only definable parameter, but for a Gaussian with the same area and maximum the FWHM is already slightly smaller. As we have seen in Figure 26, homogeneous diffusion tends to smooth out the edges giving the profiles, in a first approximation, a Gaussian-like shape until the profiles reach the ground mode. To be able to compare general symmetric profiles we can define an equivalent width parameter as the ratio of the area and the maximum.

Modelling the discharge phase of our experiments allows us to estimate the initial profiles before the onset of the recombination phase, these estimates are linked to the physical dimensions of the resonator itself. Based on the estimated initial profiles we can evaluate the range of systematic errors introduced by the unknown profiles in the experiments and choose an optimal width parameter for data processing that is also dependent on the physical properties of the microwave resonator and the discharge container.

8.1.2 *Hot Electrons in the Discharge*

The active discharge is a tough nut to crack. First, we recapitulate its characteristics and the approximations used for low to medium pressure microwave discharges. The electric field accelerates only the electrons, ions are considered too heavy to react to the frequency of the field. Electrons posses a non-Maxwellian energy distribution with a characteristic cut at the excitation or ionisation energy of the buffer gas. The electron temperature is approximated by an effective value T_e that can be calculated from the mean energy of the distribution function. This value is used to derive the ambipolar diffusion coefficient and electron-ion recombination rate coefficient in the discharge. In the initial breakdown phase the ionisation rate is proportional to the electric field until the Debye shielding by the plasma reaches a considerable effect forcing out the external electric field from the most dense region of the discharge. In our case we have to further consider the effective blocking of the incoming microwave power due to the shift in the resonant frequency of the relatively high quality microwave cavity. This effect can practically prevent the full microwave power from entering the cavity which could result in an order of magnitude drop in electron number density.

The list of processes to include in a completely self-consistent 2D model seems quite threatening and so the approach chosen for this work is to use several approximate 2D distributions of the effective electron temperature and through it derive the ionisation rate $\zeta(\mathbf{r}) = k_e(\mathbf{r})\,[\mathrm{He}]$ by electron impact ionisation without calculating the instantaneous microwave field in the resonator. Thus the final outcome of the model is a range of possible initial conditions for the recombination dominated phase. The electron-ion recombination rate coefficient α will be discussed in the next subsection. Mathematically speaking we are extending the master equation by non-linear production and destruction terms dependent on the electron number density

$$\frac{\partial n_e(r,z,t)}{\partial t} = \zeta(r,z)\,n_e - \alpha(r,z)\,n_e^2 + \nabla\cdot\left(D_A(r,z)\,\nabla n_e\right). \qquad (63)$$

The parameters ζ, α and D_A are considered independent of time, i. e., the electron temperature does not change significantly in the modelled discharge region. This approximation is necessary to be able to effectively solve the diffusion part of the equation for substantial simulation times and will be examined together with the assumed electron energy distribution.

From this point on there are little or no analytical tools at our disposal and we apply finite difference numerical methods to solve the arising non-linear systems of equations. We use an equidistant rectangular grid to represent the modelled number densities. The ζ, α and D_A are represented on the same grid and are purely input parameters of the model. The diffusion and chemical parts are solved separately at each time step. This approach is called Strang splitting. The initial number density is first advanced by a half step of the chemical kinetics followed by a full step of diffusion and another half step chemical kinetics. This way the full problem is separated into well defined parts that can be solved using higher order implicit methods. Complex chemical models are usually represented by so called stiff systems of equations where implicit numerical schemes are frequently chosen to avoid unnecessarily costly computational time and numerical instabilities.

For the spatial integration of the diffusion equation we make use of the Crank-Nicolson algorithm and the finite differences diffusion operator is constructed including the already mentioned zero Dirichlet boundary conditions and the spatial dependent ambipolar diffusion coefficient. Since this operator is independent of time we are required to invert the arising sparse matrix only at the start of the calculations, making the individual time steps fast. All sparse matrix and vector operations are handled by the Eigen template library[2], matrix inversion is done by LU decomposition as implemented in this library. The numerical solution of the diffusion equation is benchmarked against the presented analytical approach. The numerical error introduced by the finite differentiating scheme is proportional to the actual gradient of the surfaces, i. e., the steeper a curve is in one of the directions the higher the error. This behaviour is by far the worst for 2D step functions (which would imply discontinuities of the modelled plasma) and instead smoothed surfaces are used to approximate flat-top electron temperatures or initial number densities.

The right hand side of chemical kinetic equations for elementary processes are built up from simple multiplication of reactant number densities and a parameter of proportionality. In this thesis we are ignoring any reaction driven temperature evolution of the modelled plasmas for two reasons. First of all, to simplify the calculations. As earlier mentioned, we have no ambitions to build up completely self-consistent models. Second of all, to represent the experimental situation, where we expect to retrieve the studied reaction coefficients in the afterglow at a constant temperature. As a consequence, the chemical part of the plasma models can be represented by a set of symbolic reactions together with their parameters of proportionality. The equations are derived from this set for each modelled species. Implicit solvers need to evaluate both the right hand side of the equation system and its Jacobian matrix at each time step. Both can be algorithmically computed from the explained basic rules of chemical kinetics. Matrix inversion is done using the same tools as for the spatial part.

---

[2] Available from `http://eigen.tuxfamily.org/index.php?title=Main_Page` (November 26, 2018).

We consider three cases of the spatial dependent effective electron temperature, as shown in Figure 27. The first one is proportional to the amplitude of the electric field shape in the microwave resonator, as calculated in Section 7.3. This case represents the very early breakdown phase and probably is a poor approximation at relatively higher number densities. The second is a flat-top distribution inside the microwave resonator, the edges are smoothed out by convolution with a Gaussian profile (FWHM of 10 mm). The third one is a modification of the electric field approach. We combine the approximation of a nearly homogeneous electron temperature and the actual calculated field by making the top flattened and including the parts of the field leaking out of the resonator. These three types of effective electron temperature distributions differ mostly in their longitudinal profile and the radial dependence is nearly flat in all cases.

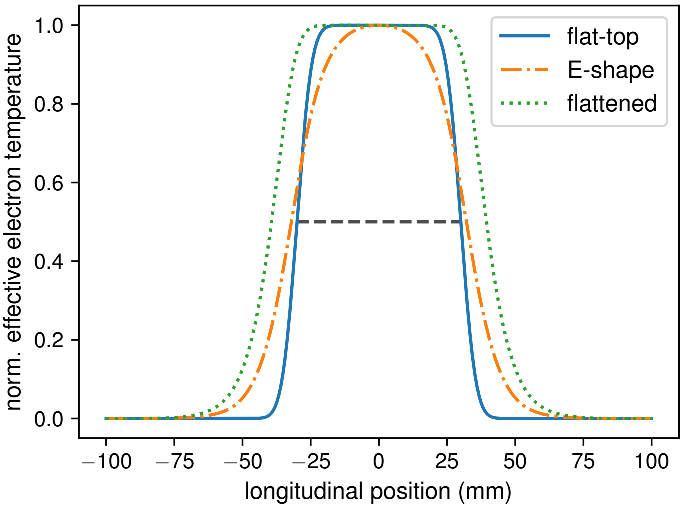

Figure 27. Normalised longitudinal profiles of effective electron temperature considered in the models. The labels correspond to the description of the profiles, see text for details. The horizontal dashed line corresponds to a FWHM of 60 mm.

Now, that we presented all the practical sides of the considered model we can continue discussing the physical background. The electron energy distribution is a function of the actual electric field. Both the ionisation rate and the elastic collision frequency of the electrons equal the buffer gas number density times the respective cross sections averaged over the same energy distribution function that is shaped by the reduced field strength. The ionisation fraction of our typical discharge plasma is too low for electron-electron Coulomb collisions to be an effective energy distribution shaping force meaning that only electrons accelerated by the field will be responsible for ionisation and excitation and the bulk can be characterised by an effective temperature of a few eV. The most problematic parts of this model are the regions outside the gradually decreasing influence of the microwave field. Momentum transfer in elastic collisions of the electrons with the buffer gas is the dominant cooling force in this type of discharge. A pure electron gas would be able to effectively transfer its energy out from the reach of the external field. Electron diffusion is inversely proportional to the elastic collision frequency but energy transfer is slower compared to diffusion due to the relatively large mass difference of the colliding particles. In a plasma, ambipolar diffusion can reverse this situation since its coefficient is now inversely proportional to the ion collision frequency (Equation 32). A continuation of the same problem is the breakdown of the plasma in the longitudinal direction. Radially, the interaction of the container walls and the plasma forms the sheath region, but its spatial scales are small compared to the modelled region and its influence can be neglected. In the longitudinal direction the plasma will never reach the edges of the discharge container before the ambipolar field gets too weak to trap fast electrons. The plasma number density where electrons decouple from ions gives us one of the limits of the physical model. Fortunately, this error is much lower than those introduced by the assumption of a quasi-steady state effective electron temperature.

8.1.3 *What Comes After the Discharge*

If this were a question, most experts would say the afterglow. Only that we have two kinds of this afterglow. One that directly follows the discharge and can be described as a period of rapid energy dissipation in the form of radiation and heat transport to the container walls. And one that is sought after by experimentalists for its near ideal thermal equilibrium (the possible equality of excitation and translational temperatures between electrons, ions and neutrals). In this subsection we will examine the first kind. We adapt the cooling model of Roučka 2012 to characterise the temporal evolution of the electron temperature. In this part of the model we assume that the electron energy distribution is already Maxwellian. The initial value is that of the effective temperature in the discharge with the same 2D distribution. We furthermore neglect any heating effects, whether it is caused by electrons released in super-elastic collisions with metastable atoms or molecules, or Penning ionisation of neutrals.

At this point electron-ion recombination enters the picture. With the rapidly decreasing temperature, the recombination rate coefficient increases quickly. As always, our exact knowledge about the rate coefficient in this matter is limited for two reasons. We require separately both the electron and rotational temperature dependence of the DR rate coefficient, and also the same for the quantification of third body processes. In this part we circumvent this problem by considering a distribution of effective values $\alpha_{\mathrm{eff}}(p, T_{\mathrm{rot}})$ at the set pressure and rotational temperature of the simulation, and a range of exponents γ in a power law type electron temperature dependence in the form of

$$\alpha(p, T_{\mathrm{rot}}, T_e) = \alpha_{\mathrm{eff}}(p, T_{\mathrm{rot}}) \left(\frac{T_e}{300\,\mathrm{K}}\right)^{-\gamma}. \tag{64}$$

This formula arises from the typical, theoretically expected energy dependence of the DR cross section (see Section 2.1 and references therein) and is often adapted in various forms in astrochemical databases (Wakelam et al. 2012) to approximate measured rate coefficients in a certain range of temperatures.

In the previous subsection we were mainly focusing on ambipolar diffusion and its role in shaping the hot plasma. In low temperature discharges, recombination can play an equally important role in regions outside the active discharge. Here the electron temperature can drop rapidly while the plasma number density is similar to the active region due to the outflow from the active discharge. This way electron-ion recombination can be a substantial contribution in shaping these regions if the absolute number density is relatively high enough. Simply said, we are solving the same equation with temperature dependent rate coefficients whether we are considering the active discharge or the thermal afterglow.

Now that we have defined the task at hand and all its ingredients we can again examine the limiting assumptions of this model. The answer is simply temperature. In the adapted cooling model we assume that momentum transfer to the buffer gas dominates the energy balance and cooling rate of electrons. The cross section of electron-helium elastic collisions is quite flat in the low energy region and can be approximated by a constant value which means that the cooling rate gets lower by decreasing temperature (due to the decrease in mean velocity). On the other had, electron-ion recombination can rise fast thanks to its typical power law dependence. This independent temperature evolution model is valid for cooling rates exceeding those of electron-ion recombination by orders of magnitude. This is a consequence of the kinetic nature of the presented model.

8.1.4 *An Afterglow in Equilibrium*

This very last phase of a typical discharge/afterglow cycle is taken in the model as the region where the electron temperature is within a few percent of its final value defined by the buffer gas temperature. An intuitive approach for our experiments is to define the border between the cooling and afterglow phases when the electron temperature dependent recombination rate coefficient differs less than the experimental precision from the final possible value at the buffer gas temperature.

So far, we have examined the role of the electrons in shaping the plasma. They drive ambipolar diffusion and recombine with ions. They can also influence ion chemistry by destroying ionic species with the highest recombination rate coefficients in a mixture of ions. In the afterglow phase of the model we shift our attention to this ion chemistry, the determining factor for experiments which aim at studying DR of concrete species or even ions in well defined quantum states.

At this point we have arrived at a splitting point of the introduced model. With each additional part of the model we are increasing its complexity. Employing certain approximations, we may smooth out the roughness of the 2D spatial grid or extend the covered time range to higher values. With the additional complexity of ion chemistry, we are reaching the practical limits of the 2D model in terms of computational time. The main goal of the development of the model was to provide a practical tool with both predictive power and flexibility. From this point on we consider two approaches for afterglow modelling: a limited (in terms of species) 2D model and a complex chemical model. Both approaches represent the same underlying situation, i. e., where the collisional (translational) temperatures of all species have reached an equilibrium represented by a common value and the chemical evolution is well represented by a set of kinetic equations. In the former we focus on the impact of ion chemistry on the 2D number density distributions of a limited number of species. While in the latter we set up a chemical network to track key species at the maximum of the underlying spatial distribution. Only the former approached is discussed in this chapter.

8.2 CRYOGENIC PLASMAS

In this section we will examine a 2D model constructed to simulate one of the lowest temperature experiments analysed in this thesis. We limit the number of charged species which are considered in the model to electrons, $H_3{}^+$ ions and $H_5{}^+$ clusters. The neutral gas mixture acts as a time independent reactant. The experimental procedure and details will be described in Chapter 9. Here we focus on the details of the simulation and the 2D number density distributions at various key time steps in the model. The final results of the simulation, as in time dependent number densities, will be compared with that of the experiments in the next section due to the additional distortion effect of the enhanced sensitivity cw-CRDS setup.

The complete model incorporates the previously described parts of a discharge/afterglow cycle in the following way. The temporal evolution is split into four phases with distinct characteristics. The initial breakdown phase is characterised by a dominant ionisation rate which is also constant for the duration of this phase. The next step represents

GROUP	PARAMETER	VALUE AND UNCERTAINTY
Exp.	Pressure	$(350 \pm 10)\,\mathrm{Pa}$
	Temperature	$(50 \pm 5)\,\mathrm{K}$
	$[H_2]$	$(1.4 \pm 0.1) \times 10^{14}\,\mathrm{cm}^{-3}$
Phase I	Ionisation rate coef.	$(1.58 \pm 0.05) \times 10^{-13}\,\mathrm{cm}^3\,\mathrm{s}^{-1}$
	Effective electron temp.	$(2.2 \pm 0.3)\,\mathrm{eV}$
Phase II	Ionisation rate coef.	$(8 \pm 2) \times 10^{-15}\,\mathrm{cm}^3\,\mathrm{s}^{-1}$
	Effective electron temp.	$(1.5 \pm 0.3)\,\mathrm{eV}$
e^-	Mom. trans. cross section	$(5.0 \pm 0.3) \times 10^{-16}\,\mathrm{cm}^2$
${H_3}^+$	Recomb. rate coef. (α_{eff})	$(1.0 \pm 0.2) \times 10^{-7}\,\mathrm{cm}^3\,\mathrm{s}^{-1}$
	Temperature exponent	-0.5 ± 0.2
${H_5}^+$	Recomb. rate coef. (α_{eff})	$(1.8 \pm 0.3) \times 10^{-6}\,\mathrm{cm}^3\,\mathrm{s}^{-1}$
	Temperature exponent	-0.7 ± 0.1
	Clustering rate coef.	$(5 \pm 1) \times 10^{-29}\,\mathrm{cm}^6\ /\mathrm{s}$

Table 10. Parameters of the 2D plasma model. Only phases I and II include electron impact ionisation. The cooling phase initial electron temperature profile and its values are the same as for discharge phase II.

the effective blocking of the incident microwave field translated as a sudden drop in ionisation rate. Here the key parameter is the effective temperature of the bulk of the electrons and the derived ambipolar diffusion coefficient. The last two steps include the electron temperature cooling, as discussed earlier, and the equilibrated afterglow evolution with constant electron, neutral and ion temperatures.

The full list of physical parameters and their assumed uncertainties are listed in Table 10. Each parameter is randomly sampled from a normal distribution with the listed mean and standard deviation values for a given calculation. The ionisation rate coefficient and effective electron temperature profiles are derived from the normalised profiles shown in Figure 26. The values listed in Table 10 correspond to the maximum of the profiles. The initial helium ions created in electron impact ionisation are assumed to be efficiently converted to ${H_3}^+$ ions that can be safely assumed for the second part of the discharge phase. We neglect the difference between the ambipolar diffusion coefficients of ${H_3}^+$ and ${H_5}^+$ ions since it plays a role only in the discharge phase where an unknown electron impact dissociation mechanism could further influence the ${H_5}^+$ relative number densities.

The experimental parameters correspond to the chosen set of measurements which will be used for comparison in the following section.

The momentum transfer cross section is taken as a lower estimate in the energy range of <10 eV (Saha 1993). The ${H_3}^+$ parameters are estimated, for the current experimental parameters, based on the results of Hejduk et al. 2015. The ${H_5}^+$ recombination parameters are taken from Macdonald, Biondi, and Johnsen 1984 and the clustering three-body rate coefficient is interpolated from the values given by Paul et al. 1995. We note that the clustering three-body rate coefficient was measured only for ${H_3}^+ + 2\,H_2$ while in our experiments the dominant channel is assumed to be ${H_3}^+ + H_2 + He$. The 'unknown' parameters of the discharge phases were adjusted to be in a rough qualitative agreement with the experimental observations. The choice of the parameters will be discussed after a summary of the results.

The timing scheme of the model corresponds to the experimental configuration. The microwave power pulse duration is 200 µs. This is split between the discharge phases I (90 µs) and II (110 µs). These values are adjusted to again get a qualitative agreement with the experimental observations. An additional uncertainty parameter is introduced for the transition time between these two phases that accounts for the uncertainty of the maximum reachable electron number density. This parameter is also sampled from a Gaussian distribution (2 µs standard deviation centred around zero) added with opposite signs to the stated lengths of phases I and II. The cooling phase is always calculated until the maximum electron temperature reaches a certain threshold difference from the neutral gas temperature. The recombination phase duration as chosen to cover the experimental repetition period of the discharge/afterglow cycle.

The results can be split into two groups. The first consists of the centre volume and line-of-sight integrated number densities of the three species are printed out at chosen time steps during the simulation. These represent the temporal evolution of the modelled plasma with two further parameters deduced from this set of data. The ratio of the integrated and maximal number densities characterises the underlying longitudinal distribution and provides a conversion parameter for line-of-sight integrated measurements of the ion density. The ratio of the electron and ion column number densities serves as a guiding parameter for recombination rate coefficient evaluation by identifying the dominant ions. The second group of results are the full 2D number density distributions of all species printed out at key time steps of the simulation.

8.2.1 *Plasma Density Profiles*

In this subsection we examine the modelled longitudinal profiles of ${H_3}^+$ number densities. As the first step, the results for the considered effective electron temperature profiles of Figure 27 are compared with each other. This is done only for the mean values of the physical parameters listed in Table 10. Three time slices of the longitudinal and radial profile evolutions are shown in Figure 28.

The time slices are chosen to represent those parts of the evolution where different effects dominate the shape of the longitudinal profiles. The first slice represents the dominant ionisation phase were the profiles closely resemble the underlying effective electron temperature profiles. The second slice represents dominant ambipolar diffusion near the end of the microwave power pulse. The third slice represents the recombination dominant phase for late times in a cold environment where ambipolar diffusion is practically frozen.

The initial normalised number density distribution of charged particles in the model is chosen as the last slice of the electron number density distribution at the end of a typical discharge/afterglow period, roughly 3.6 ms after the start of the microwave pulse. The difference between this profile and the ${H_3}^+$ profiles is due to clustering into ${H_5}^+$. At the end of the afterglow phase the ${H_3}^+$ ions are only a small fraction of all charged particles. To speed up the calculation the initial ${H_3}^+$ and ${H_5}^+$ number densities are both set to half of the electron number density.

8.2.2 *Plasma Density Evolution*

In the first half of the following subsection we will show a typical output of the temporal evolution of the plasma model for a chosen effective electron temperature profile. In the second half we will again compare the considered effective electron temperature profiles of Figure 27 in terms of the temporal evolutions of the effective width of the longitudinal cuts of charged particle volume number densities.

Figure 29 shows a typical output of the temporal evolution for the smoothed flat-top effective electron temperature profile. The results are split into three parts. The first part shows the number density evolution for all three species at the centre of the discharge container. The second part gives the effective length of the longitudinal profiles calculated as the ratio of the column number density (at the symmetry axis of the model) and the centre number density. The two representations can be always converted by this parameter. The third part shows the relative ion density of ${H_5}^+$ cluster ions defined as the ratio of electron and ${H_5}^+$ number densities at the centre position.

The full outputs (as in Figure 29) of the models for different effective electron temperature profiles behave qualitatively similar so that a complete comparison can be omitted and instead we focus on the differences in the longitudinal profiles of charged particle number densities. Figure 30 shows a comparison of effective width parameters for the different electron temperature profiles of Figure 27. The plotted values are relative to the case of the flat-top temperature profile. A comparison with the case of an ideally flat-top longitudinal number

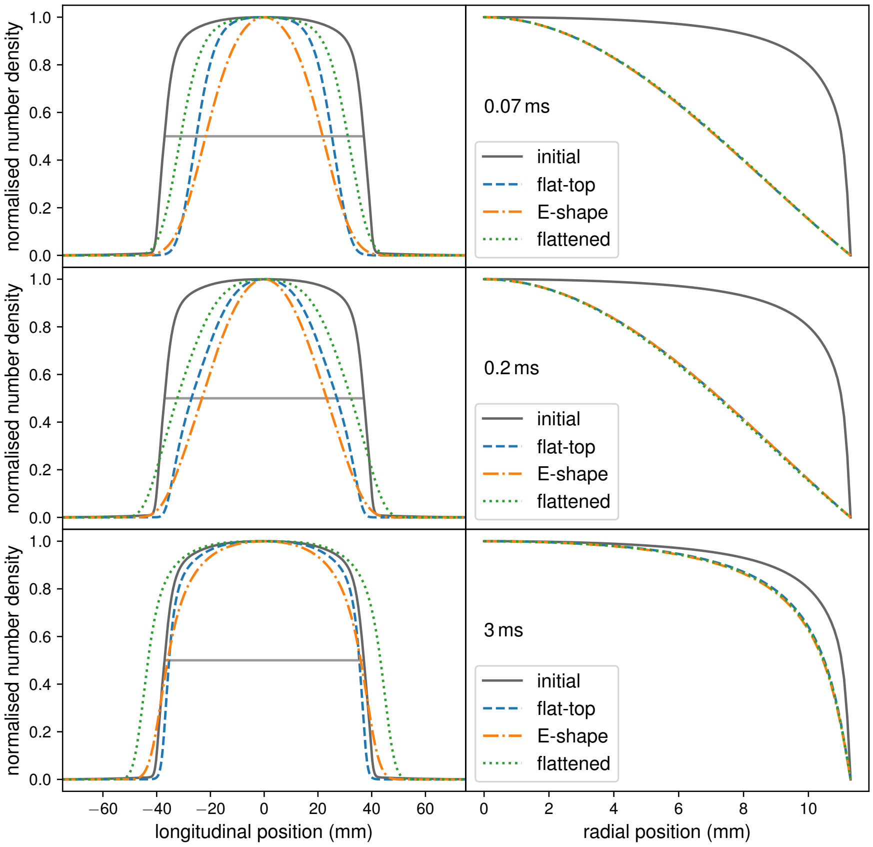

Figure 28. Longitudinal and radial profiles of normalised $H_3{}^+$ number density. Each row represents a time slice of the full temporal evolution. The left panels show the longitudinal profiles zoomed in on the main region for better clarity. The right panels show the radial profiles which are almost identical for each effective electron temperature profile. The labels of the lines correspond to the electron temperature profiles of Figure 27 and are identical for both panels. The initial profile for the given width (indicated by the solid horizontal line) corresponds to the profile of the leftover electrons at the end of the afterglow phase, see text for details.

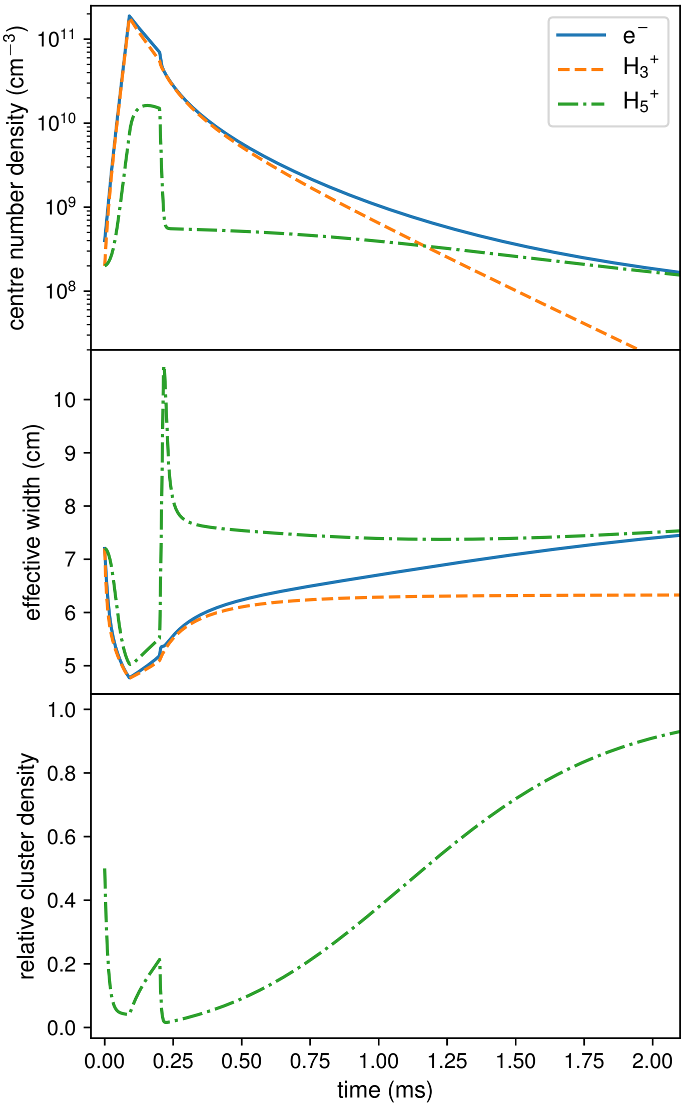

Figure 29. Temporal evolution of the plasma model. The upper panel shows the temporal evolution of electron, $H_3{}^+$ and $H_5{}^+$ number densities at the centre of the discharge container. The labelling of the lines is shared for all panels. The middle panel shows the temporal evolution of the effective width parameters for the longitudinal profiles of the named charged particle number densities. The lower panel shows the number density of $H_5{}^+$ cluster ions relative to the electron number density at the centre of the discharge container.

density profile that's width is also constant in time is also included. This profile is the standard assumption used in the preliminary analysis of the recorded column number densities in the experiments.

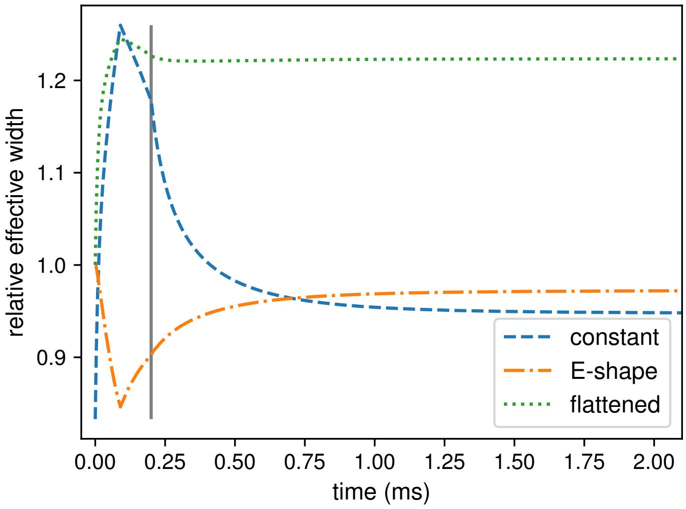

Figure 30. Temporal evolution of relative effective width parameters for the different electron temperature profiles of Figure 27. All plotted values are relative to the width parameter obtained for the flat-top electron temperature profile. The dashed line labelled 'constant' is the ratio of a constant (in time) width parameter of 6 cm and the reference width parameter. The rest of the labels correspond to the electron temperature profiles of Figure 27. The vertical solid line shows the end of the simulated microwave pulse.

In the following section we will consider only the case of the flat-top effective electron temperature profile for the comparison with experimental data and as the input of the optical simulations. The other cases can be related to it by the relative width parameters.

8.3 THROUGH THE CRDS

In this section we will closely examine the technique which allows to combine the sensitivity of CRDS with a temporally resolved approach to track the time evolution of transient species. We will concentrate on the special case when the characteristic time scales of changes of transient species number densities are similar to the photon lifetime in the optical cavity. This is the case of the results obtained utilising our novel cryogenic instrument and presented in Chapter 9.

The basic RD evaluation algorithm used throughout this work assumes that the column number density of the absorbing species for the duration of a single event is constant in time. Due to the approximately exponential nature of the light intensity decay, this criterion is relaxed to a certain extent. On the other hand, due to the non-linearity of the actual RD decay (see Section 4.3.6), the deviation from a perfect exponential strongly depends on the actual temporal evolution of the number density of the absorbing species. The basic RD evaluation algorithm assigns the initial time stamp of the signal (relative to the discharge/afterglow period) to the evaluated photon decay rate in a best approximation for a negligible deviation from the exponential shape. This method is referred to as the 0th-order approximation in this thesis.

An alternative time stamp evaluation would need to take into account the temporal evolution and the magnitude of the estimated photon decay rates. This approach can be well defined only for a limited subset of temporal evolutions, e. g., an exponentially decaying number density. In this thesis we choose to offer a tool that is able to estimate the systematic effects of this data evaluation algorithm. The preference of this approach will be explained in a comparison with alternative RD evaluation techniques.

8.3.1 *Systematic Effects*

The first step of assessing the systematic effects and errors introduced by a chosen method of RD evaluation is to estimate the actual temporal evolution of number densities of species of interest. Here we will use the results of the 2D model which offer various types of temporal evolutions as compared to a simple analytical decay model. Another advantage of the model results is the direct availability of column number densities. The time dependent longitudinal profile width parameters (see Figure 30) add an additional degree of variations to the simulation.

The optical simulation parameters of the cw-CRDS are chosen according to the properties of the actual optical setup employed in the cryogenic experiments of Chapter 9. The parameters are listed in Table 11. The RD signals are simulated based on the integral evaluation method of Section 4.3.6.

The main input parameter of the RD signal simulation is the temporal evolution of the modelled H_3^+ column number density. This is first converted into the corresponding optical depth evolution at the maximum of a chosen absorption line by calculating the integral line intensity and simulating a line shape. The Doppler width and the line intensity are calculated for the mean value of the temperature parameter listed in Table 10. The FWHM of pressure broadening is chosen as $2 \times 10^{-3}\,\mathrm{cm}^{-1}$, corresponding to the observed values. Only the two strongest *para*- and *ortho*-H_3^+ transitions are considered in this example. The corresponding spin manifold number densities are calculated from the modelled values by assuming a constant *para*-H_3^+ fraction.

First, the RD signals are generated for a chosen series of time stamps which is a subset of the input number density temporal evolution du-

PARAMETER	VALUE
Reflectance	>0.999 98
FSR	180 MHz
Finesse	220 000
Photon lifetime	200 µs
RD length	400 µs
RD amplitude	2000 arb.u.
RD offset	330 arb.u.
Sampling frequency	1.25 MHz

Table 11. Typical parameters of the enhanced cw-CRDS employed in the cryogenic experiments of Chapter 9.

ration. The time stamps of the simulated RD signals are generated in units of the ADC sampling frequency. A white noise can be also added at this time point to simulate the data acquisition conditions. Each of the simulated RD signals is fitted with the same procedure as the experimentally recorded waveforms. A constant weight is assigned to each data point. The non-linear fitting suite uses a Trust Region Reflective algorithm as implemented in the SciPy library[3]. In the last step the fitted photon decay rates are transformed back to column number densities. Figure 31 shows a comparison of cw-CRDS simulated and input *para*-H_3^+ column number densities

Two types of input column number densities are chosen in Figure 31 for a comparison to quantify the magnitude of the systematic error introduced by the chosen 0^{th}-order RD evaluation method. The first one is the full temporal evolution of the modelled H_3^+ column number density from Section 8.2.2 transformed to *para*-H_3^+ number density by a constant p_3 factor. The second one is a simple exponential decay with a decay rate corresponding to H_5^+ clustering in the plasma model. This type is chosen specifically as a reference. The relative error with an exponential decay is almost flat compared with a general decaying temporal evolution.

8.3.2 *Model vs Experiment*

The last phase of the cw-CRDS simulation is the comparison of the modelled and experimentally observed column number densities. For this purpose a specific measurement is chosen where it is possible to demonstrate each step of the plasma model. The data correspond to the experiments described in detail in Section 9.2, with the chosen measurements conducted in a helium buffered plasma with *para*-enriched

---

[3] Jones, E., T. Oliphant, P. Peterson, et al. `https://www.scipy.org/` (February 5, 2019)

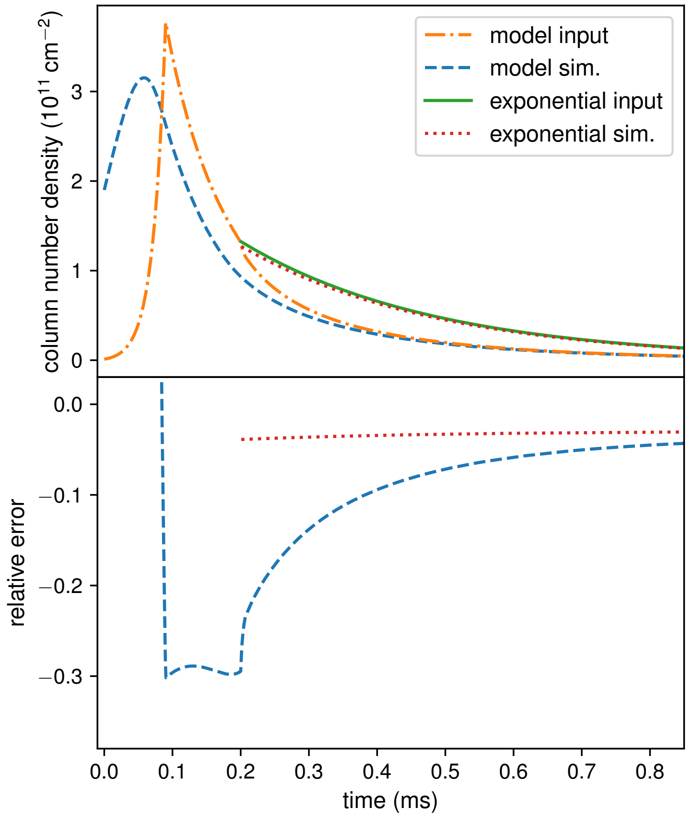

Figure 31. Comparison of cw-CRDS simulated and input column number densities. The upper panel shows the two types of input column number densities for *para*-$H_3{}^+$ and the respective simulation values labelled as 'sim.' where the sources of the inputs are the flat-top effective electron temperature model of Section 8.2.2 and a simple exponential decay, respectively. The decay rate of the exponential evolution corresponds to $H_5{}^+$ clustering used in the plasma model. The initial column density of the exponential decay roughly equals the model column density at the end of the microwave pulse. The lower panel shows the relative error of the cw-CRDS column number density evaluation calculated as the difference of the simulated and input column number densities divided by the input column number density. Labelling of the lines correspond to the upper panel.

hydrogen as the precursor of the ions at a nominal temperature of 50 K. The reasons for this specific choice will be discussed at the end of this chapter. Figure 32 shows a comparison of both modelled and experimentally recorded temporal evolutions of *para*- and *ortho*-H_3^+ column number densities.

In this specific case the *para*-H_3^+ fraction for the modelled values is chosen as the mean value of the full experimental temporal evolution. Since the $H_3^+ + H_2$ reactive collision system is not part of the model a constant p_3 values is chosen to test the influence of the cw-CRDS data evaluation on this assumption.

8.3.3 *Advanced Ring-down Processing*

Up to this point only the 0^{th}-order RD data processing method has been considered. The actual reason behind using the presented approach is its relatively simple applicability. The computational costs of this data processing method are low. As the simulations show, the systematic effects introduced by this method can be analysed for a given temporal evolution of column number densities. Moreover, by assigning the initial time stamps of the RD signals to the evaluated photon decay rates (and through that to the values of column number densities) the case of purely decaying temporal evolutions is still well defined. The displayed column number density evolution in this case always underestimates the actual values, as shown in Figure 31.

Alternative RD processing methods include iterative algorithms, numerical derivation or non-parametric fitting schemes. Each of these has their own drawbacks which can be also linked to the current hardware specifications of the RD waveform acquisition. Depending on the parameters of Table 11, the offset of the RD signal can be badly resolved, i. e., when the waveform is not recorded long enough to determine the offset independently. In this case the standard exponential fitting algorithm will fail if the deviation from true exponential behaviour of the recorded RD signal is greater than some noise limit. This failure shows up as a correlation between the parameters of a fit since the non-linear fitting algorithm will try to compensate for the observed deviation. Iterative algorithms based on the standard fitting procedure will fail in this case and are only applicable in restricted cases, e. g., for a purely decaying temporal evolution. Numerical derivation of the RD signals is the most straightforward approach but also depends on the subtraction of the offset values and is susceptible to electric noise.

Non-parametric fitting can be introduced as a last resort where the underlying temporally resolved photon decay rate is directly accessible. An optimisation algorithm would proceed by introducing an initial guess which is varied through the introduced cw-CRDS simulation. This is a highly expensive approach which is also susceptible to noise on the RD signals. A simple explanation for the difference in achievable

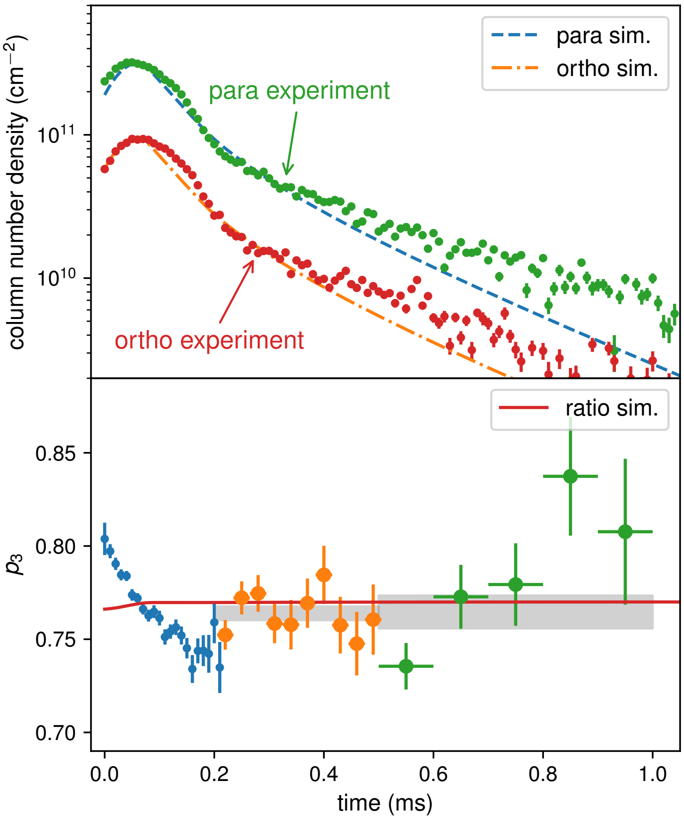

Figure 32. Comparison of cw-CRDS simulated and recorded column number densities for H_3^+ ions. Upper panel shows the comparison of experimentally recorded column number densities for both *para*- and *ortho*-H_3^+ (small filled circles annotated as experiment) with the modelled values of Figure 29 additionally processed through the cw-CRDS simulation. The dashed and dash-dotted lines correspond to the mean values of the model parameters. The shaded areas are the result of the Monte Carlo variation of the plasma model parameters. The outer area is defined as the maximum and minimum of all the modelled temporal evolutions. The inner areas are defined as the 16th and 84th percentile of the same, roughly corresponding to one sigma uncertainties. The lower panel shows the *para*-H_3^+ fractions for both the experimental (symbols) and modelled (solid line) column number densities. The shaded areas are averages of the experimental values in the given time intervals.

statistical uncertainties of the listed approaches is that the advanced methods use each data point of the recorded waveforms whereas the exponential fitting assumes a pre-defined shape of the RD decay and reduces each RD signal to three parameters.

8.4 DISCUSSION AND CONCLUSIONS

In this chapter I have presented a complex example of afterglow data interpretation. The various parts of this procedure include plasma modelling and simulation of the optical diagnostic technique. The presented examples focus on the case of our newly commissioned apparatus described in Chapter 7.

In the first half of the chapter I have described an approach of plasma modelling suitable for our experiments and the application of a specific model that can compared with experimental data. The predictive power of this model have been analysed in terms of the model parameters. A Monte Carlo approach is used to incorporate the uncertainty of the these parameters.

In the second half I have focused on the employed cw-CRDS and the systematic effects of RD signal evaluation. The enhanced sensitivity of the setup requires the redefinition of temporal resolution and a novel approach to extract temporally resolved column number densities.

8.4.1 *Predictive Power*

The predictive power and uncertainty of the presented plasma model is defined as the variation in the output parameters of the model for a given set of assumptions and input parameters. First of all we can examine the assumed effective electron temperature profiles. Figure 30 summarises the quantitative differences between the three cases. There are two effects that impact that ${H_3}^+$ longitudinal number density profiles. The overall shape of the effective electron temperature distributions and the transition from ${H_3}^+$ dominated to ${H_5}^+$ dominated plasmas. For the shapes not only the FWHM plays a role as it is evident from the comparison of the flat-top and microwave electric field shaped distributions at early afterglow times (compare with Figure 27). For similar shapes the increase in the input width (effective electron temperature profile) translates as increase in the output width parameter (longitudinal number density profile). The assumption of a flat-top longitudinal number density profile that is constant in time can result in a difference of up to 15 % in the evaluation of volume number densities at the centre of the discharge container in the early afterglow phase. The predicted effect of increasing longitudinal profile widths in the afterglow would manifest as a slow down of the decay of the evaluated volume number density under the assumption of a constant width. Naturally, this holds in the case of a high enough temporal resolution. The 0th-order RD evaluation further smooths out these effects.

8.4.2 *Final Approach*

For a final data interpretation scheme it is necessary to combine the modelled plasma temporal evolutions with the simulation of the cw-CRDS setup and RD evaluation procedure. An example is shown Figure 31 where the modelled temporal evolution of ${H_3}^+$ column number density from Figure 29 is used as input. The standard 0th-order RD fitting procedure smooths out transition effects and damps the actual decay. The modelled temporal evolution is compared to a simple exponential model as defined previously. For this case the relative error introduced by the evaluation procedure is roughly constant in time and it can be interpreted as the difference between the initial column number density at the start of the RD signal and a weighted average over the recorded length of the RD signal. An exponential decay of ${H_3}^+$ ions caused by a clustering reaction with a homogeneous reactant is also independent of the ion number density profile and its rate can be inferred from the observed column number density evolution.

This weighted averaging interpretation is only applicable when the difference between the actual and fitted RD signals is low enough. For a general decaying number density or fast enough changes, as seen in Figure 31, a breakdown of the fitting algorithm and the correlation of fit parameters has to be further considered.

Figure 32 demonstrates the combination of a Monte Carlo plasma modelling approach with the simulation of the cw-CRDS setup and employed RD evaluation procedure. The agreement between the model and experimental results are qualitative due to the uncertainties and approximations in the complex model. A quantitative agreement could be reached for the afterglow phase by adjusting the parameters of the model. However, a fitting procedure of the recombination rate coefficients would still rely on some initial estimate of the ion and electron longitudinal profiles. On the other hand, it is possible to infer the clustering rate coefficient from the presented data. This is avoided in Figure 32 to limit the dependence of the presented plasma model on the experimental data.

The assumption of a constant *para*-${H_3}^+$ fraction for the observed temporal evolution is also tested. The evolution of experimentally observed p_3 values can be excluded a result of the RD evaluation procedure. The capabilities of the current model in terms of ion chemistry are limited. Nonetheless, the actual p_3 temporal evolution is most likely smoothed out by RD evaluation procedure.

In the scope of the presented plasma model we can estimate typical systematic errors introduced by the unknown longitudinal profile widths and the RD signal evaluation algorithm. The final estimate builds on the combination of the results of Figure 30 and Figure 31. Assuming a constant width of 6 cm that is the standard assumption used to evaluate the H_3^+ volume number density at the centre of the discharge container we introduce a maximal relative error of roughly 40 % at the start of the afterglow phase that is slowly decreasing as both figures indicate. The largest source of this error is the 0th-order RD evaluation and is only relevant for the presented model case where we have a complete overview of the input parameters of the simulation. The actual error is likely the function of plasma parameters and would need to be determined on a case by case basis.

Ion chemistry plays a large role in both the temporal and spatial evolution of the modelled plasmas. The study of the $H_3^+ + H_2$ reactive collisional system under the conditions of afterglow plasmas at low temperatures and the interpretation of the observed *para*-H_3^+ fractions calls for the aid of plasma modelling. For a reliable data interpretation the presented model would need to be enhanced by the inclusion of several additional species like helium ions and metastable atoms and molecules. Model development would also benefit from experimental observation of these species that can be identified as the goal of future experiments.

To overcome the limitation of the current RD evaluation procedure improvement of the RD acquisition electronics is necessary. A reduction of the electrical noise by a factor of ten would already allow the use of advanced data processing techniques. A higher flexibility in this system would also allow the development of alternative RD processing methods. This could be achieved by reducing the number of electronic components present in the timing scheme and replacing digital signalling cables by optical fibres.

9

CRYOGENIC AFTERGLOW PLASMAS

This chapter is dedicated to the commissioning of our novel experimental instrument presented in Chapter 7. I contributed to both the design and testing of certain elements of the instrument. Here I present the details of the data processing of the very first commissioning and scientific measurements conducted using this instrument. Some of the data analysed in this chapter have appeared previously in two separate scientific articles (Dohnal et al. 2019; Plašil et al. 2018).

The main goal of the commissioning experiments was to asses the ion and neutral gas temperatures at the lowest achievable temperature in the current configuration. For this purpose we chose to exploit ${H_3}^+$ ions. These can be produced at a sufficiently high number density at the planned lowest temperatures and thanks to the relatively small mass of ${H_3}^+$, the Doppler width of the absorption lines could still be the main contribution over pressure broadening in the covered temperature range. The capabilities of this apparatus will be analysed in terms of temperature stability, repeatability of the experimental settings, achievable signal-to-noise ratio of spectral measurements and other systematic factors. I will systematically categorise and analyse our experiments, with the help of additional data not yet available in (Plašil et al. 2018), to study of the cooling capabilities of our novel instrument.

There is a long series of steps between building up a scientific instrument that is designed to study, for example, DR of molecular ions and actually producing scientific data. We chose the goal of our very first experiments conducted using this instrument as to probe some of the fundamental characteristics of ${H_3}^+$. Namely, the *para*/*ortho* ratios in low-temperature plasmas and the reactive collisions system of ${H_3}^+ + H_2$. An initial analysis of the experiments was published by Dohnal et al. 2019. Here I will analyse and compare the available data with my modelling efforts presented in Chapter 8 and the results of the 22-pole ion trap experiment of Grussie et al. 2012. My present analysis will focus on the interpretation of the experiments in terms of thermal relaxation processes and the role of the ${H_3}^+ + H_2$ collision system.

9.1 PURSUIT OF SENSITIVITY

The absorption spectrometer described in Section 7.5 has largely different optical parameters from that used in the experiments of Chapter 5 and Chapter 6 that impact the temporal resolution capabilities of the present experiments. Here we make use of the simulation and analysis reported in Section 8.3. When not otherwise stated, the presented absorption spectra and other related results are a product of the 0$^{\text{th}}$-order approximation. The reasons behind this approach will be revealed during the steps of the presented data analysis. For a complete discussion of the temporal resolution of the present spectrometer see Section 8.3.

We will adapt the statistical approach of Chapter 5 with a few additional modifications. The first steps taken in the experiments were based on the measurement schemes of the previous setup. What we later modified was the timing scheme of the microwave power pulses. This was largely possible due to the superior timing capabilities of the novel solid-state microwave source compared with the previous magnetron based type. The data analysis follows the same logic. The time period of the 'ON' state will be described as the nominal discharge period and similarly the 'OFF' state as the nominal afterglow period. The CRDS background for ionic and transitions species is again estimated from the last hundreds of microseconds of the nominal afterglow period depending on the actual repetition frequency of the whole cycle.

9.1.1 *First Experiments*

In the very first part of the spectral measurements we focused on the lowest achievable temperatures of the experimental configuration in He/H_2 or He/Ar/H_2 mixtures with normal hydrogen gas, i. e., that has a room temperature *para*/*ortho* ratio. We recorded several spectral lines in one set of measurements in the nominal temperature range of 28 K to 50 K. These values are based on the readings of temperature sensors placed at key positions in the apparatus.

While trying to use a similar timing scheme as in our previous experiments (nominal discharge period took roughly 15 % to 30 % of the whole cycle with a repetition period of roughly 4 ms), we observed two effects. The discharge had been regularly ignited in a few hundred nanoseconds after the onset of the cycle. The used microwave output power was in the range of 10 W to 25 W. The evaluated absorption signals reached a peak value after a few microseconds and then stabilised at a lower level. A similar effect could be observed on the reflected microwave power from the resonator. Although the 0$^{\text{th}}$-order RD evaluation method smooths out certain transient effects, the direction of changes are well encoded in the signal.

The second effect was a systematic increase in temperature sensor readings. This was positively identified as the heat load delivered at the gas by the microwave power reaching the discharge container wall. The room temperature gas entering the cryogenic area can be also considered as an additional heat load. Its heating effects were estimated to be negligible even at the lowest temperatures for a combination of mass flow and pressure below 0.5 Pa m^3 s^{-1} and 500 Pa, respectively. Moreover, we observed a drop in the temperature reading of sensor H (the one closest to the room temperature stage of the experimental vacuum system) when the helium buffer gas entered the system at the lowest temperatures, most likely due to an increase in thermal contact between the sapphire and the stainless steel parts. We can consider this observed temperature drop as evidence for effective pre-cooling of the buffer gas.

Following up on the initial peak in the evaluated signal, we optimised (shortened) the pulse width of the nominal discharge period while keeping the full cycle duration the same. As expected, several temperature sensors close to the discharge container reacted with a decrease in the temperature readings. Additionally, the initial 'peak' duration in the evaluated signal, i. e., before the maximum value drops to its half, turned out to be in the tens of microseconds range even when the nominal discharge period was set to, for example, 10 µs.

We adapted this approach of setting the nominal discharge period in the 10 µs to 200 µs range for the rest of the experiments. We systematically studied the dependence of the maximum achievable signal strength, i. e., maximum ion column number density, and its subsequent temporal evolution on experimental conditions, such as buffer gas pressure, temperature and H_2 partial pressure. The full discharge/afterglow cycle period was varied in the 3 ms to 10 ms range in the measurements in order to reliably determine the CRDS baseline.

The most probable explanation of the observed discharge effects is linked to the quality of the microwave resonator and power source. In the absence of the interacting electrons, the microwave field reaches its maximum intensity in the resonator. This leads to the ignition of a dynamic discharge where the ionising avalanche can reach estimated average electron number densities close to 10^{11} cm^{-3}. The sudden increase in plasma density shifts the resonance frequency and effectively blocks the microwave power. Without this source of energy for the electrons, such relatively high number densities cannot be maintained. Diffusion and recombination in this plasma proceeds at a slower rate than the initial ionising avalanche. If the microwave power source is still emitting its power to the resonator when a sustainable (10^{10} cm^{-3}) average number density is reached, the discharge can reach a quasi-steady state.

9.1.2 *Record Low Temperature*

Here we examine the first spectra recorded at the nominal temperature of 28 K. Argon would freeze out on the discharge container wall in this temperature range. We restricted the experiments to a He/H_2 mixture with a total pressure of 170 Pa. We set the relative pressure of the hydrogen gas to 7×10^{-5}. These values would translate to

$[\mathrm{He}] = 4 \times 10^{17}\,\mathrm{cm}^{-3}$ and $[\mathrm{H_2}] = 3 \times 10^{13}\,\mathrm{cm}^{-3}$ at 28 K. Figure 33 shows a pair of H_3^+ absorption lines that probe the lowest rotational states of the *para*- and *ortho*-manifolds, respectively.

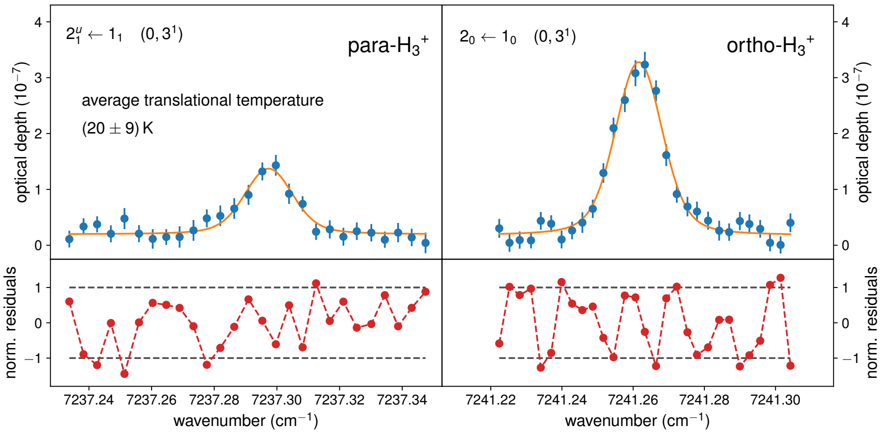

Figure 33. H_3^+ absorption lines recorded at the lowest temperature of the current experimental configuration. The value of the plotted optical depth at each wavenumber is the average of the evaluated values over the microwave pulse width. These are the product of the 0th-order RD evaluation method. The experimental conditions are given in the text. The ion translational temperature quoted in the upper left panel is a weighted average of both fitted values by Voigt line shape fits. The lower panels show the residuals of the fits normalised by the estimated statistical uncertainty.

The lines shown in Figure 33 were recorded with a pulse width of 100 µs and are a results of signal averaging over this period. Due to the non-linear behaviour of the 0th-order RD evaluation method, the 'future' values of the time dependent optical depth also influence the evaluated values up to the length of the recorded DR signal. On the other hand, thanks to weighted averaging, higher numerical values have higher relative weights (the statistical uncertainty associated with each RD signal is assumed to be constant) and the temporally averaged, estimated optical depth magnitude is closer to the maximum.

Pressure broadening of these lines at the chosen experimental conditions is a key factor in the translational temperature evaluation. It contributes roughly 25 % of the FWHM and its uncertainty accounts for the increased error in temperature determination. The fitted background, Doppler and pressure broadened FWHM are strongly correlated and care was taken to record the lines in a wide enough spectral range.

9.1.3 *Temperature Calibration*

The pair of lines shown in Figure 33 was just the beginning of the systematic study of ion translational temperature at different experimental conditions, mainly differing in the range of temperatures explored in the experiments.

Figure 34 shows a summary of the evaluated ion translational temperatures plotted as a function of recorded values of temperature sensor H. The same figure includes shaded areas that border the range of possible values of the discharge container wall temperature at a given sensor reading. Each of these is the result of separate experiments. The lower and upper limits are given by the readings of sensor C and H, respectively, that include the estimated absolute error of these measurements. The dashed line visualises the case when the reading of temperature sensor H is used as an estimator if the neutral gas temperature.

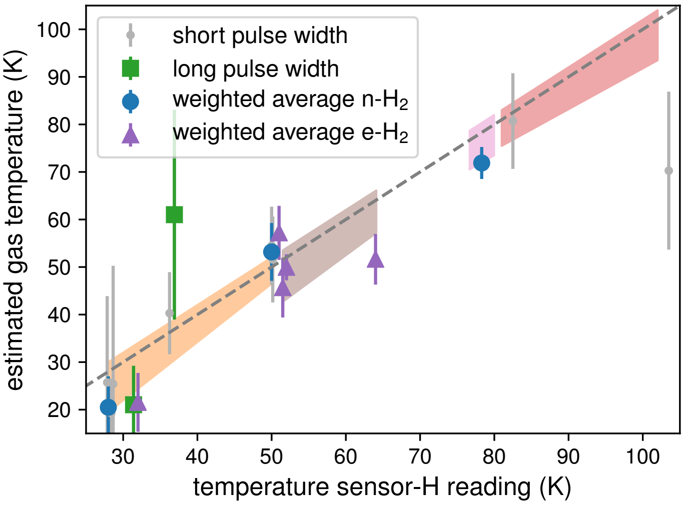

Figure 34. Comparison of neutral gas temperature estimators. Evaluated values of the ion translational temperature are plotted is symbols and are considered as an upper estimator. Recorded values of key temperature sensors constrain the shaded area of the estimated discharge container wall temperature. These are considered as a lower estimator. The dashed line plots the case when the reading of temperature sensor H is used as an estimator. A thorough explanation of the individual symbols is given in the text.

The symbols are also grouped into three larger categories. The first category is the pulse width. Values plotted as squares (long pulse width) belong to experiments where the pulse width of the microwave power was 1 ms. The values represented by the rest of the symbols are a product of experiments with pulse widths shorter than 200 µs. In each case the absorption lines are a product of averaging over the pulse width.

The second category is whether normal or *para*-enriched hydrogen was used in the experiments. Values plotted as triangles (weighted average of e-H_2) belong to experiments with *para*-enriched hydrogen. The rest of the symbols designate values evaluated from experiments with normal hydrogen.

And the thirds category is weighted averaging. Symbols labelled by short and long pulse width, respectively, denote individual values from spectral line fits. Symbols labelled with weighted average denote values that are products of averaging of individual fits. This category helps visualise the data and promotes the reproducibility of the experiments.

In the case of ion translational temperatures, there is no statistically significant difference between experiments with normal and *para*-enriched hydrogen gas. There is also no statistically significant difference between the present data from experiments with different pulse width expect for the systematic difference in the recorded temperature sensor readings, most likely due to the reachable signal-to-noise ratios. All processed absorption lines are averaged over the duration of the microwave power pulse. In the experiments with 'long' pulse width, the maximum observable average ion number density is lower which usually leads to a lower signal-to-noise with the same integration time. All the shown data were used equally for further data analysis and discussions.

The purpose of the comparison of evaluated ion translational temperatures and the estimated wall temperature is to find a good estimator of the neutral gas temperature. Both physical quantities put constraints on the actual neutral gas temperature. The evaluated values of the ion translational temperature characterise the overlapping region of the trapped laser light and the ions. It serves as an upper limit for the neutral gas temperature, as discussed in Section 4.2.4. On the other hand, the value of the discharge container wall temperature serves as a lower limit for the neutral gas temperature. The agreement between both limiting values is very good and helps further constrain the neutral gas temperature. The dashed line, i. e., the recorded values of sensor H, serves as an example of a systematic estimator that can be used to systematically control the neutral gas temperature in the experiments within a range of uncertainties. Such a parameter promotes the reproducibility of the presented experiments.

9.2 PARA VS ORTHO

In the second half of this chapter we will aim at the analyses of experiments where we varied the *para*/*ortho* ratio of the used reactant hydrogen gas to study the $H_3^+ + H_2$ reactive collision system. So far, we have avoided the question of column number densities of H_3^+ ions in the experiments. Generally, if we have an experimental knowledge of the values of ion translational and rotational temperatures we can estimate the ion column number densities from a pair of transitions coupled to *para* and *ortho* states. The subsequently derived *para*-H_3^+ fractions (p_3), in the literature sometimes mentioned as spin excitation temperatures, are the basis of this study.

As previously shown, there is a close relation between the neutral and ion temperatures and we promote the use of the experimentally evaluated ion translational temperature values and the readings of key temperature sensors to estimate the neutral gas temperature. This relation works both ways and can be theoretically extended to the ion rotational temperature.

In the following text the setup of *para*-enriched hydrogen based experiments, rotational temperature analysis and the derived *para*-H_3^+ fractions will be presented.

9.2.1 *Para-enriched Hydrogen*

We employed the *para*-hydrogen gas generator of Hejduk 2013. The purpose of this instrument is to convert room temperature hydrogen gas with a *para*-H_2 fraction of 0.25 (a high temperature statistical value) to an almost pure *para*-hydrogen gas with a *para*-H_2 fraction of approximately 0.995. This value was determined in the 22-pole ion trap experiments of Zymak et al. 2013. The generator is based on the catalytic conversion of hydrogen molecules on a paramagnetic surface cooled down to temperatures in the range of 11 K to 18 K.

An earlier version of this instrument with a different catalyst material was employed by Hejduk et al. 2012 to study the parameters of H_3^+-dominated plasmas in the temperature range of 77 K to 200 K. The presented study can be considered as a continuation of these experiments although the plasma excitation scheme discussed above is different enough that care must be taken when comparing the experiments.

In the present experiments we used mixtures of the *para*-enriched gas with normal hydrogen from a high purity gas bottle. The *para*-enriched hydrogen was mixed with the buffer gas and reactant mixtures prior entering the experimental vacuum system. The final *para*-H_2 fraction is evaluated from the ratio of the partial gas flows. The normal hydrogen gas flow was measured by a standard mass flow controller. The gas flow of the *para*-enriched gas can be controlled by the catalyst temperature of the generator. We calibrated this mass flow before each experiment by controlled filling of the experimental vacuum system with the *para*-enriched hydrogen gas at conditions similar to the experiments and measuring the temporal evolution of the recorded pressure. The precision of this calibration method depends on the error of the volume determination.

ION	TRANSITION		$\tilde{\nu}$ (cm^{-1})		
	ROT.	VIB.	PRESENT	OBS.	CALC.
H_3^+	$1_2 \leftarrow 2_2$	$(0, 3^1)$	6877.5548(4)	6877.546	6877.553
	$4^l_3 \leftarrow 3_3$	$(0, 3^1)$	–	7234.957	7235.007
	$2^u_1 \leftarrow 1_1$	$(0, 3^1)$	7237.2980(2)	7237.285	7237.304
	$2_0 \leftarrow 1_0$	$(0, 3^1)$	7241.2617(2)	7241.245	7241.239

Table 12. A list of H_3^+ transitions probed in the experiments presented in this chapter. Central wavenumbers labelled as 'present' and their error estimates were obtained in the current analysis. The values labelled as 'obs.' and 'calc.' are taken from Table 1. For a description of the transition labelling and used sources see Table 1.

The second systematic factor that determines the actual *para*-H_2 fraction in the experiments is reactive processing of the gas in the $H_3^+ + H_2$ collision system and the back-flow of hydrogen molecules synthesised on the surface of the discharge container. Both mechanisms depend on collision processes in the discharge. Duration of the microwave pulse and the maximum reachable plasma density are key factors in these processes.

9.2.2 *Spin Manifold Rotational Temperatures*

Following the same assumptions we can show that at a nominal temperature of 28 K only the respective lowest energy states of the *para*- and *ortho*-manifolds should be observable in the experiments. We are offered two partial solutions in this case. Probe all available transitions of H_3^+ and put an upper limit on the population of higher energy states and use the estimated neutral gas temperature to characterise the spin manifold rotational populations. We combined both in the experiments and analysis. Table 12 shows the list of H_3^+ transitions that were used in the experiments.

In the nominal temperature range of 50 K to 65 K we observed an additional transition ($1_2 \leftarrow 2_2$, $(0, 3^1)$) coupled to the *para*-manifold. Figure 35 shows a pair of recorded *para*-H_3^+ lines. The energy difference between the respective lower states of these transitions is roughly 150 K. This allows to evaluate a rotational temperature value with a comparable statistical uncertainty to that of the ion translational temperature even when the two transitions have several times different intensities, as shown in Figure 35. The plotted absorption lines were recorded in an experiment with pure *para*-enriched gas as the reactant.

In the same experiment, we also probed the spectral range where the *ortho*-H_3^+ transition $4^l_3 \leftarrow 3_3$, $(0, 3^1)$ was observed in previous experiments (see, e. g., Glosík et al. 2015). We did not observe the ab-

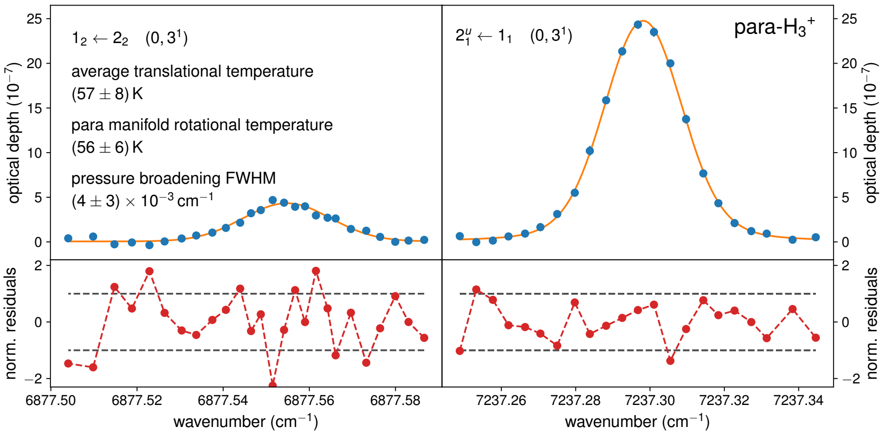

Figure 35. Example of para-manifold rotational temperature determination based on the ratio of two *para*-H_3^+ absorption lines. The transitions were probed in an experiment with a helium buffered plasma where pure *para*-enriched hydrogen was used as the precursor of the H_3^+ ions. Experimental conditions were: overall pressure of 450 Pa, estimated wall temperature in the range of 57 K to 66 K and $[H_2] = 1 \times 10^{14}\,\mathrm{cm}^{-3}$.

sorption lines, as expected in the range of experimental temperatures. We can estimate an upper limit of the *ortho*-manifold temperature from the sensitivity of the measurements as 100 K. For the same value as the estimated *ortho*-manifold rotational temperature the intensity of the $4_3^l \leftarrow 3_3$, $(0,3^1)$ transition would be one order of magnitude lower than the sensitivity of the spectral measurements.

9.2.3 *Reactive Collisions*

We chose the following approach in the experiments to systematically determine the *para*-H_3^+ fraction as a function of the reactant *para*-H_2 fraction. We integrated the absorption signal at the near-centre of the two strongest H_3^+ transitions to determine the respective column number densities of both *para* and *ortho* states. We monitored the laser frequency in order to correct for the offset of the set wavelength from the actual transition frequency. The observed differences in the frequencies combined with the uncertainty of the line shape can lead to a maximum of 1 % systematic uncertainty. We did not attempt to monitor background contributions for the following reasons. The spectral measurements of absorption lines determined from the signal corresponding to the nominal discharge period did not show a statistically significant background contribution for the experimental parameters covered in this analysis. And the *para*-H_3^+ fractions can be also determined from the recorded data with a low enough statistical uncertainty for time periods following the termination of the incident microwave power. Figure 36 shows a pair of H_3^+ absorption lines for both spin states recorded in a helium buffered plasma with pure *para*-enriched hydrogen as the precursor. The plotted optical depth is averaged over the nominal discharge time period.

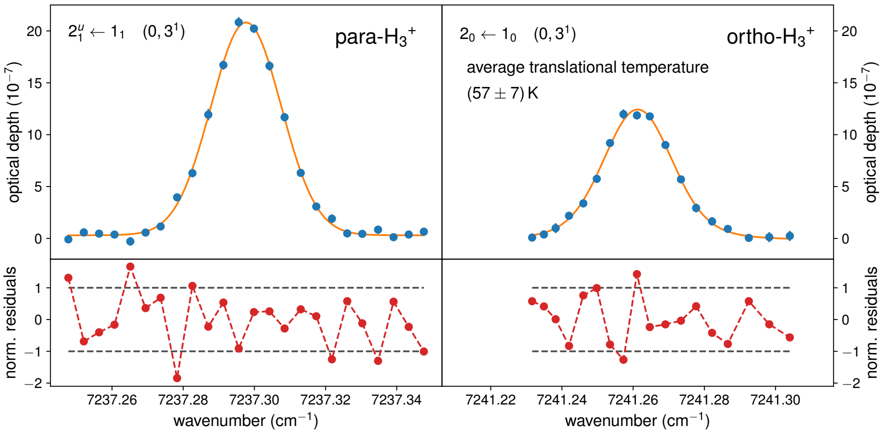

Figure 36. Example of *para*-H_3^+ fraction determination based on the ratio of one *para*- and one *ortho*-H_3^+ absorption lines. The transitions were probed in an experiment with a helium buffered plasma where pure *para*-enriched hydrogen was used as the precursor of the H_3^+ ions. Experimental conditions were: overall pressure of 350 Pa, estimated wall temperature in the range of 44 K to 51 K and $[H_2] = 1.3 \times 10^{14}\,\mathrm{cm^{-3}}$.

Figure 37 shows the combined result of several sets of our measurements conducted at nominal temperatures of 50 K and 60 K compared with chemical model calculations and the results of the 22-pole ion trap experiment of Grussie et al. 2012. The present results can be grouped into three categories where each plotted group is labelled additionally by the nominal collisional temperature of the $H_3^+ + H_2$ complex. All the presented experiments were conducted in helium buffered plasmas with hydrogen only as the precursor of the ions.

Two data points labelled as 'lines' are the results of full spectral measurements where the evaluated optical depth is averaged over the nominal discharge period. The data point labelled as 'extrapolation' is also evaluated from similar full spectral measurements and data averaging with one addition. We recorded four pairs of H_3^+ absorption lines at incrementally increased buffer gas pressures in the range of 200 Pa to 400 Pa to evaluate the pressure broadening of the transitions. We kept the flows of the buffer gas and *para*-enriched hydrogen constant and so the hydrogen number density stayed also constant in the measurements in the range of $1.0 \times 10^{14}\,\mathrm{cm^{-3}}$ to $1.9 \times 10^{14}\,\mathrm{cm^{-3}}$. When the evaluated *para*-H_3^+ fractions are plotted as a function of hydrogen number density or the multiply of helium and hydrogen number densities, a systematic increase of p3 towards lower values

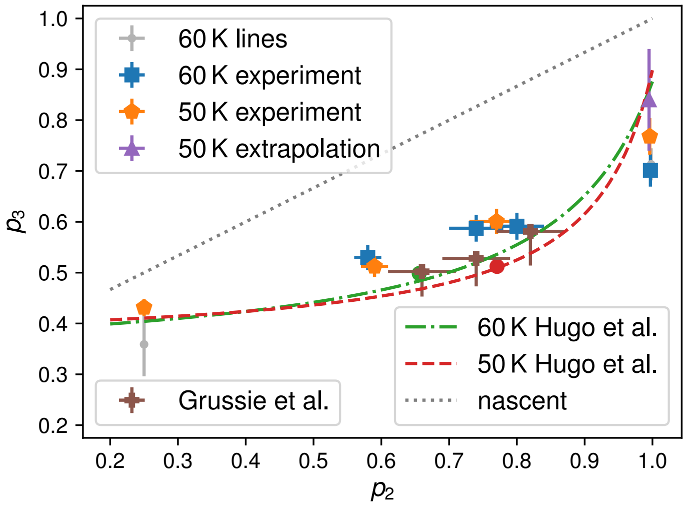

Figure 37. Dependence of para-$H_3{}^+$ fraction on para-H_2 in afterglow plasmas. The measurements were conducted in helium buffered plasmas with pure normal or *para*-enriched H_2, or their mixtures as the precursor of the $H_3{}^+$ ions. See text for experimental conditions and explanation of labelling. The unlabelled filled circles lying on top of the dashed and dot-dashed lines represent the corresponding values for the equilibrium of translational (collisional) and excitation temperatures.

can be observed. This can be interpreted in terms of $H_5{}^+$ clustering similar to the effect proposed by Hejduk et al. 2015. The authors of the cited articles propose a dependence of the effective recombination rate coefficient on helium and hydrogen number densities as described. The plotted value is the product of extrapolation to zero densities and its meaning will be discussed in the upcoming conclusions.

The last group of data points labelled as ‘experiment’ are the results of single point spectral measurements aimed at maximal integration times. The plotted values are averaged over a time interval of 200 µs following the end of the nominal discharge interval of same duration. The *para*-$H_3{}^+$ fractions determined over the stated time interval from these single point measurements have statistical uncertainties on the 1 % level (lower than the estimated total systematic uncertainties). This allows for the effective comparison of values averaged over the duration of the nominal discharge period (discharge values) and the immediate time interval following it (afterglow values). The nominal discharge values corresponding to experiments with normal hydrogen or its mixtures with *para*-enriched hydrogen are systematically shifted to higher values by a few percent while those corresponding to pure *para*-enriched hydrogen are unaffected compared to the nominal afterglow values. We prefer the latter values for further comparisons. The interpretation of the observed differences between different time periods are also discussed in the upcoming conclusions.

The experimental conditions at nominal temperatures of 50 K and 60 K (data points labelled as 'lines' and 'experiment') were the following. We used mixtures of He/H_2 with a total pressure of 350 Pa and 450 Pa, respectively. The *para*-H_2 fractions are determined from the relative gas flows of the normal and *para*-enriched hydrogen gases. The total number density of H_2 in the experiments is taken as the sum of both sources. Due to an initial calibration error of the *para*-enriched flow, the H_2 number density was set to increase in the experiments with increasing p_2 in the ranges of $0.7 \times 10^{14}\,\mathrm{cm}^{-3}$ to $1.4 \times 10^{14}\,\mathrm{cm}^{-3}$ and $1.3 \times 10^{14}\,\mathrm{cm}^{-3}$ to $1.9 \times 10^{14}\,\mathrm{cm}^{-3}$, respectively. An undefined source of uncertainty can be also present in the evaluated p_3 values due to this increase of total H_2 number density.

The main contribution to systematic uncertainties is the precision of the calculated Einstein coefficients of Mizus et al. 2017 (these are believed to be precise up to 5 %). A secondary source of systematic errors is due to the uncertainty of the ion rotational temperature. Its effect is at most below 3 %, mainly contributing to the uncertainty of the *para*-$H_3{}^+$ column number density determination. The present values shown in Figure 37 are plotted showing the total estimated uncertainties of both the p_3 (as discussed) and p_2 parameters. The main source of the *para*-H_2 fraction uncertainties is the mass flow calibration of the *para*-enriched hydrogen gas.

The results of chemical models shown in Figure 37 are calculated in the same approach as in Figure 5. The labels show the collisional temperature used in the calculations. The nascent distribution is independent of the collisional temperature. The filled circles show the corresponding values for the equilibrium of translational (collisional) and excitation temperatures.

Only selected results of the 22-pole ion trap experiment of Grussie et al. 2012 are shown in Figure 37. These correspond to values where the observed translational and rotational temperatures of the ions were close to 60 K. We note that the trap temperatures were systematically lower than the observed ion temperatures. This discrepancy is attributed to the insufficient cooling of ions in the ion trap.

9.3 DISCUSSION AND CONCLUSIONS

In this chapter I have presented the details of the data analysis of the very first commissioning and scientific measurements conducted using our novel cryogenic SA-CRDS instrument. Some of the data used for the analysis in this chapter have appeared previously in two separate scientific articles (Dohnal et al. 2019; Plašil et al. 2018).

9.3.1 *Temperature Estimates*

In the first part of this chapter I have assessed the ion and neutral gas temperatures, starting from the lowest achievable temperature of the cryo-cooler in the current configuration, as a function of the estimated discharge container wall temperature. For this purpose I have processed experiments studying ${H_3}^+$ ions for the purpose of ion vibrational spectroscopy aided thermometry. These can be produced at a sufficiently high number density even at the achievable lowest temperature and thanks to the relatively small mass of ${H_3}^+$, the Doppler width of the absorption lines was observed to be the main contribution over pressure broadening. I have systematically categorised and analysed our experiments, with additional data not yet available in (Plašil et al. 2018), to study of the cooling capabilities of our novel instrument.

Figure 34 shows the combined results of the present analysis. Two independent estimators of the neutral gas temperature are plotted in this figure. Experimentally evaluated ion translational temperatures (various symbols) are interpreted as the upper limit of the neutral gas temperature. Combined readings of key temperature sensors (shaded areas) are stepwise used as estimates of the discharge container wall temperature. These in turn serve as a lower limit of the neutral gas temperature.

The excellent agreement between the plotted independent estimators is interpreted as follows. The heat load presented by the microwave discharge is effectively cooled by the discharge container wall thanks to the sufficient heat transport system between the active cryo-cooler and the cryogenic elements. The temperature of the neutral gas is close to that of the discharge container wall, i. e., lies in the range of the combined uncertainties. The volume distribution of the neutral temperature is homogeneous in the range of uncertainties. This is supported by the observed ion translation temperature which is an average value for the line-of-sight overlap of the probing laser beam and the volume distribution of the ions. The ion rotational temperatures, when not directly observed, are estimated to be equal to the translational temperatures in the range of uncertainties. This procedure is based on the agreement between observed values of rotational and translational temperatures in our previous higher temperature experiments. We note that for ${H_3}^+$ below 60 K the rotational temperature and its uncertainty plays a minor role ($<3\,\%$ relative error) when determining absolute column number densities as long as the rotational sates can be characterised by a Boltzmann distribution. We did not observe anomalous rotational population distributions in the respective spin manifolds in the range of measurement sensitivity.

Alternatively, we can estimate both the ion and neutral kinetic (combined translational and rotational) temperatures from the recorded temperature sensor readings when direct observations are not available. This procedure is based on the repeatability and systematic dependence of the observed ion translational temperature on the readings of key temperature sensors shown in Figure 34. These represent a reliable control parameter of the experiments.

The unknown pressure broadening of the absorption lines affects the achievable statistical uncertainty of the translational temperature determination. As a future step, I propose the systematic study of the pressure broadening on both the buffer gas and reactant partial pressures. Care has to be taken when evaluating the parametric dependence of the proposed measurements. We observed a dependence of maximum ion number density in the temporally resolved experiments on both the buffer gas and reactant partial pressures. The microwave pulse width has to be also taken into account in the proposed experiments. A combined effect of the listed parameters can lead to variations of the discharge dynamics and possible changes in the heat load delivered by the discharge. I also propose a systematic study of the effective discharge termination mechanism (discussed earlier in Section 9.1.1) linked to the used microwave pulse width.

9.3.2 *Para/Ortho Equilibrium*

In the second part of this chapter I have analysed the experiments aiming at understanding the dependence of the *para*-$H_3{}^+$ fraction of the ions as a function of the *para*-H_2 fraction of the precursor gas. The presented experiments are considered the first step towards DR studies of $H_3{}^+$ in the newly available temperature range in afterglow plasmas.

Figure 37 shows the results of two sets of the present experiments at nominal temperatures of 50 K and 60 K compared with the results of chemical models (based on rate coefficients from Hugo, Asvany, and Schlemmer 2009) and the results of the 22-pole ion trap experiment of Grussie et al. 2012.

The theoretical calculations of Hugo, Asvany, and Schlemmer 2009 and the derived chemical models based purely on $H_3{}^+ + H_2$ reactive collisions are taken as the reference and basis of the interpretation of the presented results. The main reasons for this are the good agreement of the calculations with the corresponding values for the equilibrium of translational (collisional) and excitation temperatures (shown as filled circles lying on top of the respective model dependences) and the agreement with the Grussie et al. 2012 results.

In this reference framework, the present data can be split into two groups based on the direction of the shift of the values compared with the models. Only the values observed in pure *para*-enriched H_2 have negative shifts compared with the models in this limited dataset. Expanding the chemical model with the nascent production distribution of $H_3{}^+$ can explain the observed positive shifts but not the negative. With the addition of nuclear spin dependent DR and clustering effects we can qualitatively interpret the negative shift as well. In this scenario we additionally assume that clustering into $H_5{}^+$ proceeds at a different rate in pure *para*-H_2 and preferentially lowers the *para*-$H_3{}^+$ fraction. This interpretation is based on largely unknown clustering effects which include both three-body association mechanisms and collision induced dissociation, and their nuclear spin selection rules. For the same reason, the analysis of the p_3 values at a nominal temperature of 30 K was not attempted where we expect a larger influence of both DR and clustering effects.

The total uncertainties estimated above and shown in Figure 37 do not include the possible influence of differences in total hydrogen number densities for each data point. The purely statistical uncertainties included in the described extrapolation method of a limited dataset are too large to draw definite conclusions in this matter. The systematic study of the dependence of p_3 on p_2 in the range of $2 \times 10^{13}\,\mathrm{cm^{-3}}$ to $2 \times 10^{14}\,\mathrm{cm^{-3}}$ of total hydrogen number densities would allow to differentiate between the $H_3{}^+ + H_2$ reactive and three-body clustering collisions.

We note that the present experiments represent time averaged slices of the underlying temporal evolution. The chosen time intervals represent sections of the underlying temporal evolution in which the data could be integrated to achieve sufficiently low statistical uncertainties and shed light on the region of interest for DR studies. The length of the time intervals were also chosen to represent the time resolution capabilities of the cw-CRDS setup as analysed in Section 8.3. Increased time resolution capabilities are necessary for future DR related experimental studies, including the evolution of the *para*-$H_3{}^+$ fraction.

10

SUMMARY AND OUTLOOK

This thesis describes recent advancements made in Stationary Afterglow (SA) instrumentation and in DR research. The ultimate goal of which is the application of experimentally deduced reaction rate coefficients in astrochemical models and the contribution to the improvement of the theoretical understanding of the related processes. The scientific results of this thesis can be grouped into three topics.

The first two topics are linked to experimental campaigns conducted on a SA apparatus shortly described in Section 4.2.1. This instrument was employed in several earlier experiments and was designed with a cooling system capable of covering the 77 K to 300 K temperature range. A technical contribution of this thesis is the description of a newly commissioned instrument, see Chapter 7, that was designed and assembled based on years of experience with the previous version. An improved cooling system utilising a closed-cycle cryo-cooler and a modified microwave discharge excitation scheme forms the core of this new instrument. The last topic covers the first scientific campaign conducted in this apparatus.

Chapter 5 describes the partial re-evaluation of experiments focusing on the proton and deuteron containing ${H_3}^+$ isotopic system. A previous analysis was published in two research articles by Dohnal et al. 2016 and Plašil et al. 2017. The basic goal of the these experiments was to evaluate isotopologue specific DR rate coefficients. Two aspects of the measurements were re-examined, the estimated neutral gas and ion temperatures and the relative ion densities of the present isotopologues in the active discharge. The systematic evaluation of ion translation temperatures with the inclusion of pressure broadening effects is proposed, giving estimates of the overall temperature uncertainties. A possible systematic error was revealed during the re-evaluation of relative ion densities thanks to comparisons with simple ion chemical models and additional experiments. An example is shown in Figure 16 giving an estimate of the estimated total error of ion density determination. This propagates directly into the evaluation of effective recombination rate coefficients and can introduce roughly 90 % relative errors for the combined weighted effective recombination rates of H_2D^+ and ${HD_2}^+$ species as a function of relative ion densities, see discussion in Section 5.4.1. This possible systematic error would prevent reasonably accurate determination of individual rate coefficients for H_2D^+ and ${HD_2}^+$ species. An experimental re-investigations of relative ion densities for the given experimental conditions is proposed.

Chapter 6 describes the analysis of first overtone absorption spectra of N_2H^+ ions as the first step towards electron-ion recombination experiments. A preliminary analysis was published by Kálosi et al. 2017. In the presented analysis the systematic inclusion of pressure broadening effects is applied based on additional experimental observations. The scientific results include an improved set of molecular constants for the (20^00) excited vibrational state of the ion. These can be used to benchmark theoretical calculations aiming to describe excited vibrational states. The evaluation of ion rotational temperatures was demonstrated and the contribution of excited vibrational states to the ion number density determination was discussed.

Chapter 9 describes both the commissioning and scientific experiments conducted on the newly built SA instrument combined with a cw-CRDS (see Chapter 7 for a complete description of the apparatus). The cooling capabilities of the instrument were determined by comparing ion translational temperatures and key readings of temperature sensors installed in the apparatus. A combined estimator of the neutral gas temperatures is proposed. The present analysis extends with additional data the results of Plašil et al. 2018. The very first scientific campaign conducted utilising this instrument was dedicated to the role of *para*/*ortho* spin modifications in the reactive collision system of ${H_3}^+ + H_2$. Again as a first step towards state specific DR rate coefficient evaluation. The experiments were conducted in the nominal temperature range of 30 K to 60 K using normal and *para*-enriched hydrogen gas. A preliminary analysis of these experiments was published by Dohnal et al. 2019. Here an interpretation of the results is proposed based on plasma modelling. Part of the plasma models is described in Chapter 8 where a greater attention is paid to systematic effects of the optical diagnostic technique. In the analysis of *para*-${H_3}^+$ fractions a simple chemical model of the ${H_3}^+ + H_2$ reactive collision system was used. The present observations were discussed in terms of additional chemical processes, e. g., clustering reactions, that can play a comparable role in the determination of the *para*-${H_3}^+$ fractions.

BIBLIOGRAPHY

Abrahamsson, K. et al. (1993). ‘CRYRING – a synchrotron, cooler and storage ring.’ In: *Nuclear Instruments and Methods in Physics Research Section B: Beam Interactions with Materials and Atoms* 79.1, pp. 269–272. DOI: `10.1016/0168-583X(93)95341-2`.

Adams, N. G. and L. M. Babcock (1994). ‘Optical Emissions from the Dissociative Electron Recombination of N_2H^+ and HCO^+.’ In: *The Journal of Physical Chemistry* 98.17, pp. 4564–4569. DOI: `10.1021/j100068a014`.

Adams, N. G., C. R. Herd, M. Geoghegan, D. Smith, A. Canosa, J. C. Gomet, B. R. Rowe, J. L. Queffelec, and M. Morlais (1991). ‘Laser induced fluorescence and vacuum ultraviolet spectroscopic studies of H-atom production in the dissociative recombination of some protonated ions.’ In: *The Journal of Chemical Physics* 94.7, pp. 4852–4857. DOI: `10.1063/1.460570`.

Agdur, B. and B. Enander (1962). ‘Resonances of a Microwave Cavity Partially Filled with a Plasma.’ In: *Journal of Applied Physics* 33.2, pp. 575–581. DOI: `10.1063/1.1702469`.

Albertsson, T., N. Indriolo, H. Kreckel, D. Semenov, K. N. Crabtree, and Th Henning (2014). ‘First Time-dependent Study of H_2 and ${H_3}^+$ Ortho-Para Chemistry in the Diffuse Interstellar Medium: Observations Meet Theoretical Predictions.’ In: *The Astrophysical Journal* 787.1, p. 44. DOI: `10.1088/0004-637X/787/1/44`.

Alge, E., N. G. Adams, and D. Smith (1983). ‘Measurements of the dissociative recombination coefficients of ${O_2}^+$, NO^+ and ${NH_4}^+$ in the temperature range 200-600 K.’ In: *Journal of Physics B: Atomic and Molecular Physics* 16.8, p. 1433. DOI: `10.1088/0022-3700/16/8/017`.

Amano, T. (1990). ‘The dissociative recombination rate coefficients of ${H_3}^+$, ${HN_2}^+$, and HCO^+.’ In: *The Journal of Chemical Physics* 92.11, pp. 6492–6501. DOI: `10.1063/1.458594`.

Amano, T., M.-C. Chan, S. Civis, A. R. W. McKellar, W. A. Majewski, D. Sadovskii, and J. K. G. Watson (1994). ‘The infrared vibration–rotation spectrum of the ${D_3}^+$ molecular ion: extension to higher vibrational and rotational quantum numbers.’ In: *Canadian Journal of Physics* 72.11, pp. 1007–1015. DOI: `10.1139/p94-132`.

Amano, T., T. Hirao, and J. Takano (2005). ‘Submillimeter-wave spectroscopy of ${HN_2}^+$ and ${DN_2}^+$ in the excited vibrational states.’ In: *Journal of Molecular Spectroscopy* 234.1, pp. 170–175. DOI: `10.1016/j.jms.2005.09.004`.

Asvany, O., E. Hugo, F. Müller, F. Kühnemann, S. Schiller, J. Tennyson, and S. Schlemmer (2007). ‘Overtone spectroscopy of H_2D^+ and

D_2H^+ using laser induced reactions.' In: *The Journal of Chemical Physics* 127.15, p. 154317. DOI: 10.1063/1.2794331.

Bardsley, J. N. (1968a). 'Configuration interaction in the continuum states of molecules.' In: *Journal of Physics B: Atomic and Molecular Physics* 1.3, p. 349. DOI: 10.1088/0022-3700/1/3/303.

Bardsley, J. N. (1968b). 'The theory of dissociative recombination.' In: *Journal of Physics B: Atomic and Molecular Physics* 1.3, p. 365. DOI: 10.1088/0022-3700/1/3/304.

Bates, D. R. (1950). 'Dissociative Recombination.' In: *Physical Review* 78.4, pp. 492–493. DOI: 10.1103/PhysRev.78.492.

Bates, D. R. and S. P. Khare (1965). 'Recombination of positive ions and electrons in a dense neutral gas.' In: *Proceedings of the Physical Society* 85.2, p. 231. DOI: 10.1088/0370-1328/85/2/305.

Bates, D. R. and H. S. W. Massey (1947). 'The basic reactions in the upper atmosphere II. The theory of recombination in the ionized layers.' In: *Proceedings of the Royal Society of London A* 192.1028, pp. 1–16. DOI: 10.1098/rspa.1947.0134.

Baumann, P. et al. (1988). 'The Heidelberg Heavy Ion Test Storage Ring TSR.' In: *Nuclear Instruments and Methods in Physics Research Section A: Accelerators, Spectrometers, Detectors and Associated Equipment* 268.2, pp. 531–537. DOI: 10.1016/0168-9002(88)90573-6.

Becker, A. (2016). 'Imaging of Neutral Fragmentation Products from Fast Molecular Ion Beams: Paving the Way for Reaction Studies in Cryogenic Environment.' PhD thesis. Ruperto-Carola University of Heidelberg.

Beenakker, C. I. M. and P. W. J. M. Boumans (1978). 'Additional experience with the cylindrical TMO_{010} cavity for generating an MIP in helium and argon at atmospheric pressure.' In: *Spectrochimica Acta Part B: Atomic Spectroscopy* 33.1, pp. 53–54. DOI: 10.1016/0584-8547(78)80066-4.

Bernath, P. F. (2015). *Spectra of Atoms and Molecules*. 3rd ed. Oxford: Oxford University Press.

Biondi, M. A. (2003). 'Dissociative Recombination of Electrons and Ions: The Early Experiments.' In: *Dissociative Recombination of Molecular Ions with Electrons*. Ed. by S. L. Guberman. Springer US, pp. 13–23. DOI: 10.1007/978-1-4615-0083-4_2.

Botschwina, P. (1984). 'An ab initio calculation of the frequencies and IR intensities of the stretching vibrations of ${HN_2}^+$.' In: *Chemical Physics Letters* 107.6, pp. 535–541. DOI: 10.1016/S0009-2614(84)85152-0.

Coutens, A. et al. (2016). 'The ALMA-PILS survey: First detections of deuterated formamide and deuterated isocyanic acid in the interstellar medium.' In: *Astronomy & Astrophysics* 590, p. L6. DOI: 10.1051/0004-6361/201628612.

Crabtree, K. N., J. N. Hodges, B. M. Siller, A. J. Perry, J. E. Kelly, P. A. Jenkins, and B. J. McCall (2012). 'Sub-Doppler mid-infrared spectroscopy of molecular ions.' In: *Chemical Physics Letters* 551, pp. 1–6. DOI: 10.1016/j.cplett.2012.09.015.

Čurík, R. and Ch. H. Greene (2017). 'Inelastic low-energy collisions of electrons with HeH^+: Rovibrational excitation and dissociative recombination.' In: *The Journal of Chemical Physics* 147.5, p. 054307. DOI: 10.1063/1.4994921.

Daniel, F., J. Cernicharo, E. Roueff, M. Gerin, and M. L. Dubernet (2007). 'The Excitation of N_2H^+ in Interstellar Molecular Clouds. II. Observations.' In: *The Astrophysical Journal* 667.2, p. 980. DOI: 10.1086/520669.

Datz, S., G. Sundström, Ch. Biedermann, L. Broström, H. Danared, S. Mannervik, J. R. Mowat, and M. Larsson (1995). 'Branching Processes in the Dissociative Recombination of ${H_3}^+$.' In: *Physical Review Letters* 74.20, pp. 4099–4099. DOI: 10.1103/PhysRevLett.74.4099.2.

Dohnal, P., M. Hejduk, J. Varju, P. Rubovič, Š. Roučka, T. Kotrík, R. Plašil, J. Glosík, and R. Johnsen (2012). 'Binary and ternary recombination of para-${H_3}^+$ and ortho-${H_3}^+$ with electrons: State selective study at 77–200 K.' In: *The Journal of Chemical Physics* 136.24, p. 244304. DOI: 10.1063/1.4730162.

Dohnal, P., Á. Kálosi, R. Plašil, Š. Roučka, A. Kovalenko, S. Rednyk, R. Johnsen, and J. Glosík (2016). 'Binary and ternary recombination of H_2D^+ and ${HD_2}^+$ ions with electrons at 80 K.' In: *Physical Chemistry Chemical Physics* 18.34, pp. 23549–23553. DOI: 10.1039/C6CP04152C.

Dohnal, P., P. Rubovič, Á. Kálosi, M. Hejduk, R. Plašil, R. Johnsen, and J. Glosík (2014). 'H_2-assisted ternary recombination of ${H_3}^+$ with electrons at 300 K.' In: *Physical Review A* 90.4, p. 042708. DOI: 10.1103/PhysRevA.90.042708.

Dohnal, P., P. Rubovič, T. Kotrík, M. Hejduk, R. Plašil, R. Johnsen, and J. Glosík (2013). 'Collisional-radiative recombination of Ar^+ ions with electrons in ambient helium at temperatures from 50 K to 100 K.' In: *Physical Review A* 87.5, p. 052716. DOI: 10.1103/PhysRevA.87.052716.

Dohnal, P., D. Shapko, Á. Kálosi, M. Kassayová, Š. Roučka, S. Rednyk, R. Plašil, M. Hejduk, and J. Glosík (2019). 'Towards state selective recombination of ${H_3}^+$ ions at astrophysically relevant conditions.' In: *Faraday Discussions*. DOI: 10.1039/C8FD00214B.

Dunham, J. L. (1932). 'The Energy Levels of a Rotating Vibrator.' In: *Physical Review* 41.6, pp. 721–731. DOI: 10.1103/PhysRev.41.721.

Dutrey, A., T. Henning, S. Guilloteau, D. Semenov, V. Piétu, K. Schreyer, A. Bacmann, R. Launhardt, J. Pety, and F. Gueth (2007). 'Chemistry in disks - I. Deep search for N_2H^+ in the protoplanetary disks around LkCa 15, MWC 480, and DM Tauri.' In: *Astronomy & Astrophysics* 464.2, pp. 615–623. DOI: 10.1051/0004-6361:20065385.

Endres, Ch. P., S. Schlemmer, P. Schilke, J. Stutzki, and H. S. P. Müller (2016). 'The Cologne Database for Molecular Spectroscopy, CDMS, in the Virtual Atomic and Molecular Data Centre, VAMDC.' In: *Journal of Molecular Spectroscopy* 327, pp. 95–104. DOI: 10.1016/j.jms.2016.03.005.

Fárník, M., S. Davis, M. A. Kostin, O. L. Polyansky, J. Tennyson, and D. J. Nesbitt (2002). 'Beyond the Born–Oppenheimer approximation: High-resolution overtone spectroscopy of H_2D^+ and D_2H^+.' In: *The Journal of Chemical Physics* 116.14, pp. 6146–6158. DOI: 10.1063/1.1458244.

Ferguson, E. E., F. C. Fehsenfeld, and A. L. Schmeltekopf (1969). 'Flowing Afterglow Measurements of Ion-Neutral Reactions.' In: *Advances in Atomic and Molecular Physics*. Ed. by D. R. Bates and I. Estermann. Vol. 5. Academic Press, pp. 1–56. DOI: 10.1016/S0065-2199(08)60154-2.

Florescu-Mitchell, A. I. and J. B. A. Mitchell (2006). 'Dissociative recombination.' In: *Physics Reports* 430.5, pp. 277–374. DOI: 10.1016/j.physrep.2006.04.002.

Fonseca dos Santos, S., N. Douguet, V. Kokoouline, and A. E. Orel (2014). 'Scattering matrix approach to the dissociative recombination of HCO^+ and N_2H^+.' In: *The Journal of Chemical Physics* 140.16, p. 164308. DOI: 10.1063/1.4871982.

Fonseca dos Santos, S., V. Kokoouline, and Ch. H. Greene (2007). 'Dissociative recombination of ${H_3}^+$ in the ground and excited vibrational states.' In: *The Journal of Chemical Physics* 127.12, p. 124309. DOI: 10.1063/1.2784275.

Foster, S. C., A. R. W. McKellar, I. R. Peterkin, J. K. G. Watson, F. S. Pan, M. W. Crofton, R. S. Altman, and T. Oka (1986). 'Observation and analysis of the ν_2 and ν_3 fundamental bands of the H_2D^+ ion.' In: *The Journal of Chemical Physics* 84.1, pp. 91–99. DOI: 10.1063/1.450137.

Furtenbacher, T., T. Szidarovszky, E. Mátyus, Cs. Fábri, and A. G. Császar (2013). 'Analysis of the Rotational–Vibrational States of the Molecular Ion ${H_3}^+$.' In: *Journal of Chemical Theory and Computation* 9.12, pp. 5471–5478. DOI: 10.1021/ct4004355.

Gamer, L., D. Schulz, C. Enss, A. Fleischmann, L. Gastaldo, S. Kempf, C. Krantz, O. Novotný, D. Schwalm, and A. Wolf (2016). 'MOCCA: A 4k-Pixel Molecule Camera for the Position- and Energy-Resolving Detection of Neutral Molecule Fragments at CSR.' In: *Journal of Low Temperature Physics* 184.3, pp. 839–844. DOI: 10.1007/s10909-015-1453-0.

Gay, C. D., P. C. Stancil, S. Lepp, and A. Dalgarno (2011). 'The Highly Deuterated Chemistry of the Early Universe.' In: *The Astrophysical Journal* 737.1, p. 44. DOI: 10.1088/0004-637X/737/1/44.

Geppert, W. D. and M. Larsson (2008). 'Dissociative recombination in the interstellar medium and planetary ionospheres.' In: *Molecular Physics* 106.16, pp. 2199–2226. DOI: 10.1080/00268970802322074.

Geppert, W. D., R. D. Thomas, J. Semaniak, A. Ehlerding, T. J. Millar, F. Österdahl, M. af Ugglas, N. Djurić, A. Paál, and M. Larsson (2004). 'Dissociative Recombination of N_2H^+: Evidence for Fracture of the N-N Bond.' In: *The Astrophysical Journal* 609.1, p. 459. DOI: 10.1086/420733.

Gerlich, D., R. Plašil, I. Zymak, M. Hejduk, P. Jusko, D. Mulin, and J. Glosík (2013). 'State Specific Stabilization of $H^+ + H_2(j)$ Collision Complexes.' In: *The Journal of Physical Chemistry A* 117.39, pp. 10068–10075. DOI: 10.1021/jp400917v.

Glosík, J., P. Dohnal, P. Rubovič, Á. Kálosi, R. Plašil, Š Roučka, and R. Johnsen (2015). 'Recombination of ${H_3}^+$ ions with electrons in He/H_2 ambient gas at temperatures from 240 K to 340 K.' In: *Plasma Sources Science and Technology* 24.6, p. 065017. DOI: 10.1088/0963-0252/24/6/065017.

Glosík, J., I. Korolov, R. Plašil, O. Novotný, T. Kotrík, P. Hlavenka, J. Varju, I. A. Mikhailov, V. Kokoouline, and Ch. H. Greene (2008). 'Recombination of ${H_3}^+$ ions in the afterglow of a He–Ar–H_2 plasma.' In: *Journal of Physics B: Atomic, Molecular and Optical Physics* 41.19, p. 191001. DOI: 10.1088/0953-4075/41/19/191001.

Gómez-Carrasco, S., L. González-Sánchez, A. Aguado, C. Sanz-Sanz, A. Zanchet, and O. Roncero (2012). 'Dynamically biased statistical model for the ortho/para conversion in the $H_2 + {H_3}^+ \longrightarrow {H_3}^+ + H_2$ reaction.' In: *The Journal of Chemical Physics* 137.9, p. 094303. DOI: 10.1063/1.4747548.

Gordon, I. E. et al. (2017). 'The HITRAN2016 molecular spectroscopic database.' In: *Journal of Quantitative Spectroscopy and Radiative Transfer* 203, pp. 3–69. DOI: 10.1016/j.jqsrt.2017.06.038.

Green, S., J. A. Montgomery, and P. Thaddeus (1974). 'Tentative identification of U93.174 as the molecular ion N_2H^+.' In: *The Astrophysical Journal* 193, pp. L89–L91. DOI: 10.1086/181639.

Grussie, F., M. H. Berg, K. N. Crabtree, S. Gärtner, B. J. McCall, S. Schlemmer, A. Wolf, and H. Kreckel (2012). 'The Low-Temperature Nuclear Spin Equilibrium of ${H_3}^+$ in Collisions with H_2.' In: *The Astrophysical Journal* 759.1, p. 21. DOI: 10.1088/0004-637X/759/1/21.

Gwarek, W. K. (1985). 'Analysis of an Arbitrarily-Shaped Planar Circuit a Time-Domain Approach.' In: *IEEE Transactions on Microwave Theory and Techniques* 33.10, pp. 1067–1072. DOI: 10.1109/TMTT.1985.1133170.

Hansson, A. and J. K. G. Watson (2005). 'A comment on Hönl-London factors.' In: *Journal of Molecular Spectroscopy* 233.2, pp. 169–173. DOI: 10.1016/j.jms.2005.06.009.

Havenith, M., E. Zwart, W. Leo Meerts, and J. J. ter Meulen (1990). 'Determination of the electric dipole moment of ${HN_2}^+$.' In: *The Journal of Chemical Physics* 93.12, pp. 8446–8451. DOI: 10.1063/1.459282.

Hejduk, M. (2013). 'Reactions of Hydrogen Molecules with Ions and Recombination of $H_3{}^+$ Ions with Electrons at Cryogenic Temperatures.' PhD thesis. Charles University in Prague.

Hejduk, M., P. Dohnal, P. Rubovič, Á. Kálosi, R. Plašil, R. Johnsen, and J. Glosík (2015). 'Flowing-afterglow study of electron-ion recombination of para–$H_3{}^+$ and ortho–$H_3{}^+$ ions at temperatures from 60 K to 300 K.' In: *The Journal of Chemical Physics* 143.4, p. 044303. DOI: 10.1063/1.4927094.

Hejduk, M., P. Dohnal, J. Varju, P. Rubovič, R. Plašil, and J. Glosík (2012). 'Nuclear spin state-resolved cavity ring-down spectroscopy diagnostics of a low-temperature $H_3{}^+$-dominated plasma.' In: *Plasma Sources Science and Technology* 21.2, p. 024002. DOI: 10.1088/0963-0252/21/2/024002.

Hiraoka, K. (1987). 'A determination of the stabilities of $H_3{}^+(H_2)_n$ with $n = 1 - 9$ from measurements of the gas-phase ion equilibria $H_3{}^+(H_2)_{n-1} + H_2 = H_3{}^+(H_2)_n$.' In: *The Journal of Chemical Physics* 87.7, pp. 4048–4055. DOI: 10.1063/1.452909.

Hodgman, S. S., R. G. Dall, L. J. Byron, K. G. H. Baldwin, S. J. Buckman, and A. G. Truscott (2009). 'Metastable Helium: A New Determination of the Longest Atomic Excited-State Lifetime.' In: *Physical Review Letters* 103.5, p. 053002. DOI: 10.1103/PhysRevLett.103.053002.

Huang, J. and K. I. Öberg (2015). 'Detection of N_2D^+ in a Protoplanetary Disk.' In: *The Astrophysical Journal Letters* 809.2, p. L26. DOI: 10.1088/2041-8205/809/2/L26.

Hugo, E., O. Asvany, and S. Schlemmer (2009). '$H_3{}^+ + H_2$ isotopic system at low temperatures: Microcanonical model and experimental study.' In: *The Journal of Chemical Physics* 130.16, p. 164302. DOI: 10.1063/1.3089422.

Johnsen, R. and S. L. Guberman (2010). 'Chapter 3 - Dissociative Recombination of $H_3{}^+$ Ions with Electrons: Theory and Experiment.' In: *Advances In Atomic, Molecular, and Optical Physics*. Ed. by E. Arimondo, P. R. Berman, and C. C. Lin. Vol. 59. Advances in Atomic, Molecular, and Optical Physics. Academic Press, pp. 75–128. DOI: 10.1016/S1049-250X(10)59003-7.

Johnsen, R., P. Rubovič, P. Dohnal, M. Hejduk, R. Plašil, and J. Glosík (2013). 'Ternary Recombination of $H_3{}^+$ and $D_3{}^+$ with Electrons in He-H_2 (D_2) Plasmas at Temperatures from 50 to 300 K.' In: *The Journal of Physical Chemistry A* 117.39, pp. 9477–9485. DOI: 10.1021/jp311978n.

Jungen, Ch. and S. T. Pratt (2009). 'Jahn-Teller Interactions in the Dissociative Recombination of $H_3{}^+$.' In: *Physical Review Letters* 102.2, p. 023201. DOI: 10.1103/PhysRevLett.102.023201.

Kabbadj, Y., T. R. Huet, B. D. Rehfuss, C. M. Gabrys, and T. Oka (1994). 'Infrared Spectroscopy of Highly Excited Vibrational Levels of

Protonated Nitrogen, HN_2^+.' In: *Journal of Molecular Spectroscopy* 163.1, pp. 180–205. DOI: `10.1006/jmsp.1994.1016`.

Kálosi, Á., P. Dohnal, L. Augustovičová, Štěpán Roučka, R. Plašil, and J. Glosík (2016). 'Monitoring the removal of excited particles in He/Ar/H_2 low temperature afterglow plasma at 80–300 K.' In: *The European Physical Journal Applied Physics* 75.2, p. 24707. DOI: `10.1051/epjap/2016150587`.

Kálosi, Á., P. Dohnal, D. Shapko, Š Roučka, R. Plašil, R. Johnsen, and J. Glosík (2017). 'Overtone spectroscopy of N_2H^+ molecular ions–application of cavity ring-down spectroscopy.' In: *Journal of Instrumentation* 12.10, p. C10010. DOI: `10.1088/1748-0221/12/10/C10010`.

Keim, E. R., M. L. Polak, J. C. Owrutsky, J. V. Coe, and R. J. Saykally (1990). 'Absolute infrared vibrational band intensities of molecular ions determined by direct laser absorption spectroscopy in fast ion beams.' In: *The Journal of Chemical Physics* 93.5, pp. 3111–3119. DOI: `10.1063/1.458845`.

Kokoouline, V. and Ch. H. Greene (2003). 'Theory of Dissociative Recombination of D_{3h} Triatomic Ions Applied to H_3^+.' In: *Physical Review Letters* 90.13, p. 133201. DOI: `10.1103/PhysRevLett.90.133201`.

Kokoouline, V., Ch. H. Greene, and B. D. Esry (2001). 'Mechanism for the destruction of H_3^+ ions by electron impact.' In: *Nature* 412.6850, pp. 891–894. DOI: `10.1038/35091025`.

Kong, S., P. Caselli, J. C. Tan, V. Wakelam, and O. Sipilä (2015). 'The Deuterium Fractionation Timescale in Dense Cloud Cores: A Parameter Space Exploration.' In: *The Astrophysical Journal* 804.2, p. 98. DOI: `10.1088/0004-637X/804/2/98`.

Krantz, C. (2009). 'Intense electron beams from GaAs photocathodes as a tool for molecular and atomic physics.' PhD thesis. Ruperto-Carola University of Heidelberg.

Krantz, C. et al. (2017). 'Single-particle detection of products from atomic and molecular reactions in a cryogenic ion storage ring.' In: *Nuclear Instruments and Methods in Physics Research Section A: Accelerators, Spectrometers, Detectors and Associated Equipment* 851, pp. 92–102. DOI: `10.1016/j.nima.2017.01.050`.

Kreckel, H., A. Petrignani, O. Novotný, K. Crabtree, H. Buhr, B. J. McCall, and A. Wolf (2012). 'Storage ring measurements of the dissociative recombination of H_3^+.' In: *Philosophical Transactions of the Royal Society A* 370.1978, pp. 5088–5100. DOI: `10.1098/rsta.2012.0019`.

Kreckel, H. et al. (2010). 'High-resolution storage-ring measurements of the dissociative recombination of H_3^+ using a supersonic expansion ion source.' In: *Physical Review A* 82.4, p. 042715. DOI: `10.1103/PhysRevA.82.042715`.

Lacour, S., M. K. André, P. Sonnentrucker, F. Le Petit, D. E. Welty, J.-M. Desert, R. Ferlet, E. Roueff, and D. G. York (2005). 'Deuterated molecular hydrogen in the Galactic ISM - New observations along seven translucent sightlines.' In: *Astronomy & Astrophysics* 430.3, pp. 967–977. DOI: 10.1051/0004-6361:20041589.

Lammich, L. et al. (2003). 'Evidence for Subthermal Rotational Populations in Stored Molecular Ions through State-Dependent Dissociative Recombination.' In: *Physical Review Letters* 91.14, p. 143201. DOI: 10.1103/PhysRevLett.91.143201.

Larsson, M. (2012). 'Dissociative recombination of ${H_3}^+$: 10 years in retrospect.' In: *Philosophical Transactions of the Royal Society A* 370.1978, pp. 5118–5129. DOI: 10.1098/rsta.2012.0020.

Larsson, M., S. Lepp, A. Dalgarno, C. Stroemholm, G. Sundstroem, V. Zengin, H. Danared, A. Kaellberg, M. Af Ugglas, and S. Datz (1996). 'Dissociative recombination of H_2D^+ and the cosmic abundance of deuterium.' In: *Astronomy and Astrophysics* 309, pp. L1–L3.

Larsson, M. and A. E. Orel (2008). *Dissociative Recombination of Molecular Ions*. Cambridge: Cambridge University Press.

Lawson, P. A., D. Osborne, and N. G. Adams (2011). 'Effect of isotopic content on the rate constants for the dissociative electron–ion recombination of N_2H^+.' In: *International Journal of Mass Spectrometry* 304.1, pp. 41–44. DOI: 10.1016/j.ijms.2011.03.013.

Lehmann, K. K. and D. Romanini (1996). 'The superposition principle and cavity ring-down spectroscopy.' In: *The Journal of Chemical Physics* 105.23, pp. 10263–10277. DOI: 10.1063/1.472955.

Li, Sh., C. Akyel, and R. G. Bosisio (1981). 'Precise Calculations and Measurements on the Complex Dielectric Constant of Lossy Materials Using TM_{010} Cavity Perturbation Techniques.' In: *IEEE Transactions on Microwave Theory and Techniques* 29.10, pp. 1041–1048. DOI: 10.1109/TMTT.1981.1130496.

Liebig, T., A. Rennings, S. Held, and D. Erni (2013). 'openEMS – a free and open source equivalent-circuit (EC) FDTD simulation platform supporting cylindrical coordinates suitable for the analysis of traveling wave MRI applications.' In: *International Journal of Numerical Modelling: Electronic Networks, Devices and Fields* 26.6, pp. 680–696. DOI: 10.1002/jnm.1875.

Lindsay, C. M. and B. J. McCall (2001). 'Comprehensive Evaluation and Compilation of ${H_3}^+$ Spectroscopy.' In: *Journal of Molecular Spectroscopy* 210.1, pp. 60–83. DOI: 10.1006/jmsp.2001.8444.

Macdonald, J. A., M. A. Biondi, and R. Johnsen (1984). 'Recombination of electrons with ${H_3}^+$ and ${H_5}^+$ ions.' In: *Planetary and Space Science* 32.5, pp. 651–654. DOI: 10.1016/0032-0633(84)90117-X.

Macko, P., G. Bánó, P. Hlavenka, R. Plašil, V. Poterya, A. Pysanenko, O. Votava, R. Johnsen, and J. Glosík (2004). 'Afterglow studies of ${H_3}^+$(v=0) recombination using time resolved cw-diode laser cavity ring-down spectroscopy.’ In: *International Journal of Mass Spectrometry* 233.1, pp. 299–304. DOI: 10.1016/j.ijms.2003.12.035.

Mahdavi, M. R., J. B. Hasted, and M. M. Nakshbandi (1971). ‘Electron-ion recombination measurements in the flowing afterglow.’ In: *Journal of Physics B: Atomic and Molecular Physics* 4.12, p. 1726. DOI: 10.1088/0022-3700/4/12/020.

Maki, A., W. Quapp, and S. Klee (1995). ‘Intensities of Hot-Band Transitions: HCN Hot Bands.’ In: *Journal of Molecular Spectroscopy* 171.2, pp. 420–434. DOI: 10.1006/jmsp.1995.1130.

Mandelshtam, V. A. (2001). ‘FDM: the filter diagonalization method for data processing in NMR experiments.’ In: *Progress in Nuclear Magnetic Resonance Spectroscopy* 38.2, pp. 159–196. DOI: 10.1016/S0079-6565(00)00032-7.

Mandelshtam, V. A. and H. S. Taylor (1997). ‘Harmonic inversion of time signals and its applications.’ In: *The Journal of Chemical Physics* 107.17, pp. 6756–6769. DOI: 10.1063/1.475324.

Massey, H. S. W. (1937). ‘Dissociation, recombination and attachment processes in the upper atmosphere–I.’ In: *Proceedings of the Royal Society of London A* 163.915, pp. 542–553. DOI: 10.1098/rspa.1937.0243.

McCall, B. J. et al. (2003). ‘An enhanced cosmic-ray flux towards ζ Persei inferred from a laboratory study of the H_3^+ recombination rate.’ In: *Nature* 422.6931, pp. 500–502. DOI: 10.1038/nature01498.

McCall, B. J. et al. (2004). ‘Dissociative recombination of rotationally cold H_3^+.’ In: *Physical Review A* 70.5, p. 052716. DOI: 10.1103/PhysRevA.70.052716.

Meyer, C. et al. (2017). ‘Radiative Rotational Lifetimes and State-Resolved Relative Detachment Cross Sections from Photodetachment Thermometry of Molecular Anions in a Cryogenic Storage Ring.’ In: *Physical Review Letters* 119.2, p. 023202. DOI: 10.1103/PhysRevLett.119.023202.

Millar, T. J. (2005). ‘Deuterium in interstellar clouds.’ In: *Astronomy & Geophysics* 46.2, pp. 2.29–2.32. DOI: 10.1111/j.1468-4004.2005.46229.x.

Millar, T. J. (2015). ‘Astrochemistry.’ In: *Plasma Sources Science and Technology* 24.4, p. 043001. DOI: 10.1088/0963-0252/24/4/043001.

Mitchell, J. B. A. (1990). ‘The dissociative recombination of molecular ions.’ In: *Physics Reports* 186.5, pp. 215–248. DOI: 10.1016/0370-1573(90)90159-Y.

Mizus, I. I., A. Alijah, N. F. Zobov, L. Lodi, A. A. Kyuberis, S. N. Yurchenko, J. Tennyson, and O. L. Polyansky (2017). *ExoMol molecular line lists – XX. A comprehensive line list for* H_3^+.

Molek, C. D., J. L. McLain, V. Poterya, and N. G. Adams (2007). ‘A Remeasurement of the Products for Electron Recombination of N_2H^+ Using a New Technique: No Significant NH+N Production.’

In: *The Journal of Physical Chemistry A* 111.29, pp. 6760–6765. DOI: `10.1021/jp068965d`.

Møller, S. P. (1997). 'ELISA, and electrostatic storage ring for atomic physics.' In: *Nuclear Instruments and Methods in Physics Research Section A: Accelerators, Spectrometers, Detectors and Associated Equipment* 394.3, pp. 281–286. DOI: `10.1016/S0168-9002(97)00673-6`.

Mondelain, D., T. Sala, S. Kassi, D. Romanini, M. Marangoni, and A. Campargue (2015). 'Broadband and highly sensitive comb-assisted cavity ring down spectroscopy of CO near 1.57 µm with sub-MHz frequency accuracy.' In: *Journal of Quantitative Spectroscopy and Radiative Transfer* 154, pp. 35–43. DOI: `10.1016/j.jqsrt.2014.11.021`.

Nakano, Y., Y. Enomoto, T. Masunaga, S. Menk, P. Bertier, and T. Azuma (2017). 'Design and commissioning of the RIKEN cryogenic electrostatic ring (RICE).' In: *Review of Scientific Instruments* 88.3, p. 033110. DOI: `10.1063/1.4978454`.

Neale, L., S. Miller, and J. Tennyson (1996). 'Spectroscopic Properties of the $H_3{}^+$ Molecule: A New Calculated Line List.' In: *The Astrophysical Journal* 464, p. 516. DOI: `10.1086/177341`.

O'Malley, T. F. (1971). 'Diabatic States of Molecules – Quasistationary Electronic States.' In: *Advances in Atomic and Molecular Physics*. Ed. by D. R. Bates and I. Esterman. Vol. 7. Academic Press, pp. 223–249. DOI: `10.1016/S0065-2199(08)60361-9`.

O'Connor, A. P. et al. (2016). 'Photodissociation of an Internally Cold Beam of CH^+ Ions in a Cryogenic Storage Ring.' In: *Physical Review Letters* 116.11, p. 113002. DOI: `10.1103/PhysRevLett.116.113002`.

Oka, T. (2004). 'Nuclear spin selection rules in chemical reactions by angular momentum algebra.' In: *Journal of Molecular Spectroscopy* 228.2, pp. 635–639. DOI: `10.1016/j.jms.2004.08.015`.

Oka, T. (2013). 'Interstellar $H_3{}^+$.' In: *Chemical Reviews* 113.12, pp. 8738–8761. DOI: `10.1021/cr400266w`.

Pachucki, K. and J. Komasa (2008). 'Ortho-para transition in molecular hydrogen.' In: *Physical Review A* 77.3, p. 030501. DOI: `10.1103/PhysRevA.77.030501`.

Padellec, A. Le, M. Larsson, H. Danared, Å Larson, J. R. Peterson, S. Rosén, J. Semaniak, and C. Strömholm (1998). 'A Storage Ring Study of Dissociative Excitation and Recombination of $D_3{}^+$.' In: *Physica Scripta* 57.2, p. 215. DOI: `10.1088/0031-8949/57/2/010`.

Pagani, L., C. Vastel, E. Hugo, V. Kokoouline, Ch. H. Greene, A. Bacmann, E. Bayet, C. Ceccarelli, R. Peng, and S. Schlemmer (2009). 'Chemical modeling of L183 (L134N): an estimate of the ortho/para H_2 ratio.' In: *Astronomy & Astrophysics* 494.2, pp. 623–636. DOI: `10.1051/0004-6361:200810587`.

Park, K. and J. C. Light (2007). 'Microcanonical statistical study of ortho-para conversion in the reaction $H_3{}^+ + H_2 \longrightarrow (H_5{}^+)^* \longrightarrow$

H_3^+ + H_2 at very low energies.' In: *The Journal of Chemical Physics* 126.4, p. 044305. DOI: 10.1063/1.2430711.

Paul, W., B. Lücke, S. Schlemmer, and D. Gerlich (1995). 'On the dynamics of the reaction of positive hydrogen cluster ions (H_5^+ to H_{23}^+) with para and normal hydrogen at 10 K.' In: *International Journal of Mass Spectrometry and Ion Processes* 149-150, pp. 373–387. DOI: 10.1016/0168-1176(95)04269-Q.

Petrignani, A. et al. (2011). 'Resonant structure of low-energy H_3^+ dissociative recombination.' In: *Physical Review A* 83.3, p. 032711. DOI: 10.1103/PhysRevA.83.032711.

Plašil, R., P. Dohnal, Á. Kálosi, Š. Roučka, R. Johnsen, and J. Glosík (2017). 'Stationary afterglow measurements of the temperature dependence of the electron–ion recombination rate coefficients of H_2D^+ and HD_2^+ in He/Ar/H_2/D_2 gas mixtures at $T = 80 - 145$ K.' In: *Plasma Sources Science and Technology* 26.3, p. 035006. DOI: 10.1088/1361-6595/aa5916.

Plašil, R., P. Dohnal, Á. Kálosi, Š. Roučka, D. Shapko, S. Rednyk, R. Johnsen, and J. Glosík (2018). 'Stationary afterglow apparatus with CRDS for study of processes in plasmas from 300 K down to 30 K.' In: *Review of Scientific Instruments* 89.6, p. 063116. DOI: 10.1063/1.5036834.

Plašil, R., I. Zymak, P. Jusko, D. Mulin, D. Gerlich, and J. Glosík (2012). 'Stabilization of H^+–H_2 collision complexes between 11 and 28 K.' In: *Philosophical Transactions of the Royal Society A* 370.1978, pp. 5066–5073. DOI: 10.1098/rsta.2012.0098.

Polyansky, O. L. and A. R. W. McKellar (1990). 'Improved analysis of the infrared spectrum of D_2H^+.' In: *The Journal of Chemical Physics* 92.7, pp. 4039–4043. DOI: 10.1063/1.457817.

Poterya, V., J. L. McLain, N. G. Adams, and L. M. Babcock (2005). 'Mechanisms of Electron-Ion Recombination of N_2H^+/N_2D^+ and HCO^+/DCO^+ Ions: Temperature Dependence and Isotopic Effect.' In: *The Journal of Physical Chemistry A* 109.32, pp. 7181–7186. DOI: 10.1021/jp051945b.

Qi, Ch., K. I. Öberg, S. M. Andrews, D. J. Wilner, E. A. Bergin, A. M. Hughes, M. Hogherheijde, and P. D'Alessio (2015). 'Chemical Imaging of the CO Snow Line in the HD 163296 Disk.' In: *The Astrophysical Journal* 813.2, p. 128. DOI: 10.1088/0004-637X/813/2/128.

Quack, M. (1977). 'Detailed symmetry selection rules for reactive collisions.' In: *Molecular Physics* 34.2, pp. 477–504. DOI: 10.1080/00268977700101861.

Rennings, A., J. Mosig, C. Caloz, D. Erni, and P. Waldow (2008). 'Equivalent Circuit (EC) FDTD Method for the Modeling of Surface Plasmon Based Couplers.' In: *Journal of Computational and Theoretical Nanoscience* 5.4, pp. 690–703. DOI: 10.1166/jctn.2008.040.

Romanini, D., A. A. Kachanov, N. Sadeghi, and F. Stoeckel (1997). 'CW cavity ring down spectroscopy.' In: *Chemical Physics Letters* 264.3, pp. 316–322. DOI: 10.1016/S0009-2614(96)01351-6.

Rosen, P. (1949). 'The Propagation of Electromagnetic Waves in a Tube Containing a Coaxial D.C. Discharge.' In: *Journal of Applied Physics* 20.9, pp. 868–877. DOI: 10.1063/1.1698549.

Rosenthal, D., F. Bertoldi, and S. Drapatz (2000). 'ISO-SWS observations of OMC-1: H_2 and fine structure lines.' In: *Astronomy and Astrophysics* 356, pp. 705–723.

Roučka, Š. (2012). 'Laboratory Astrochemistry and Applications of Computer Simulations.' PhD thesis. Charles University in Prague.

Rubovič, P. (2014). 'Electron Ion Recombination in Low Temperature Plasma.' PhD thesis. Charles University.

Rubovič, P., P. Dohnal, M. Hejduk, R. Plašil, and J. Glosík (2013). 'Binary Recombination of ${H_3}^+$ and ${D_3}^+$ Ions with Electrons in Plasma at 50–230 K.' In: *The Journal of Physical Chemistry A* 117.39, pp. 9626–9632. DOI: 10.1021/jp3123192.

Saha, H. P. (1993). 'Ab initio calculation of scattering length and cross sections at very low energies for electron-helium scattering.' In: *Physical Review A* 48.2, pp. 1163–1170. DOI: 10.1103/PhysRevA.48.1163.

Sasada, H. and T. Amano (1990). 'Observation of the $2\nu_1$ band of ${HN_2}^+$ with a 1.57 µm distributed feedback semiconductor laser.' In: *The Journal of Chemical Physics* 92.4, pp. 2248–2250. DOI: 10.1063/1.458017.

Schlingman, W. M. et al. (2011). 'The Bolocam Galactic Plane Survey. V. HCO^+ and N_2H^+ Spectroscopy of 1.1 mm Dust Continuum Sources.' In: *The Astrophysical Journal Supplement Series* 195.2, p. 14. DOI: 10.1088/0067-0049/195/2/14.

Schmidt, H. T. et al. (2017). 'Rotationally Cold OH^- Ions in the Cryogenic Electrostatic Ion-Beam Storage Ring DESIREE.' In: *Physical Review Letters* 119.7, p. 073001. DOI: 10.1103/PhysRevLett.119.073001.

Shornikov, A., D. A. Orlov, C. Krantz, A. S. Jaroshevich, and A. Wolf (2014). 'Maximum intensity, transmission limited cold electron beams from GaAs photocathode in the eV and sub-eV kinetic energy range.' In: *Physical Review Special Topics - Accelerators and Beams* 17.4, p. 042802. DOI: 10.1103/PhysRevSTAB.17.042802.

Smith, D. and N. G. Adams (1984). 'Dissociative recombination coefficients for ${H_3}^+$, HCO^+, N_2H^+, and ${CH_5}^+$ at low temperature - Interstellar implications.' In: *The Astrophysical Journal* 284, pp. L13–L16. DOI: 10.1086/184342.

Sochi, T. and J. Tennyson (2010). 'A computed line list for the H_2D^+ molecular ion.' In: *Monthly Notices of the Royal Astronomical Society* 405.4, pp. 2345–2350. DOI: 10.1111/j.1365-2966.2010.16665.x.

Španěl, P. and D. Smith (2017). 'Selected Ion Flow Tube (SIFT) Applications in Mass Spectrometry.' In: *Encyclopedia of Spectroscopy and Spectrometry (Third Edition)*. Ed. by J. C. Lindon, G. E. Tranter, and D. W. Koppenaal. Oxford: Academic Press, pp. 56–68. DOI: 10.1016/B978-0-12-409547-2.05253-7.

Špirko, V., O. Bludský, and W. P. Kraemer (2008). 'Energies and Electric Dipole Moments of the Bound Vibrational States of $HN_2{}^+$ and $DN_2{}^+$.' In: *Collection of Czechoslovak Chemical Communications* 73.6, pp. 873–897. DOI: 10.1135/cccc20080873.

Stensgaard, R. (1988). 'ASTRID - The Aarhus Storage Ring.' In: *Physica Scripta* 1988 (T22), p. 315. DOI: 10.1088/0031-8949/1988/T22/051.

Stevefelt, J., J. Boulmer, and J.-F. Delpech (1975). 'Collisional-radiative recombination in cold plasmas.' In: *Physical Review A* 12.4, pp. 1246–1251. DOI: 10.1103/PhysRevA.12.1246.

Talicska, C. N., M. W. Porambo, A. J. Perry, and B. J. McCall (2016). 'Mid-infrared concentration-modulated noise-immune cavity-enhanced optical heterodyne molecular spectroscopy of a continuous supersonic expansion discharge source.' In: *Review of Scientific Instruments* 87.6, p. 063111. DOI: 10.1063/1.4953652.

Tanabe, T., K. Noda, and E. Syresin (2004). 'An electrostatic storage ring with a merging electron beam device at KEK.' In: *Nuclear Instruments and Methods in Physics Research Section A: Accelerators, Spectrometers, Detectors and Associated Equipment*. International Workshop on Beam Cooling and Related Topics 532.1, pp. 105–110. DOI: 10.1016/j.nima.2004.06.035.

Thomas, R. D. et al. (2011). 'The double electrostatic ion ring experiment: A unique cryogenic electrostatic storage ring for merged ion-beams studies.' In: *Review of Scientific Instruments* 82.6, p. 065112. DOI: 10.1063/1.3602928.

Tom, B. A. et al. (2009). 'Dissociative recombination of highly enriched para-$H_3{}^+$.' In: *The Journal of Chemical Physics* 130.3, p. 031101. DOI: 10.1063/1.3065970.

Turner, B. E. (1974). 'U93.174 - A new interstellar line with quadrupole hyperfine splitting.' In: *The Astrophysical Journal* 193, pp. L83–L87. DOI: 10.1086/181638.

van 't Hoff, M. L. R., C. Walsh, M. Kama, S. Facchini, and E. F. van Dishoeck (2017). 'Robustness of N_2H^+ as tracer of the CO snowline.' In: *Astronomy & Astrophysics* 599, A101. DOI: 10.1051/0004-6361/201629452.

Vigren, E., V. Zhaunerchyk, M. Hamberg, M. Kaminska, J. Semaniak, M. af Ugglas, M. Larsson, R. D. Thomas, and W. D. Geppert (2012). 'Reassessment of the Dissociative Recombination of N_2H^+ at CRYRING.' In: *The Astrophysical Journal* 757.1, p. 34. DOI: 10.1088/0004-637X/757/1/34.

Vogel, S. (2016). 'Developments at an Electrostatic Cryogenic Storage Ring for Electron-Cooled keV Energy Ion Beams.' PhD thesis. Ruperto-Carola University of Heidelberg.

von Hahn, R. et al. (2016). 'The cryogenic storage ring CSR.' In: *Review of Scientific Instruments* 87.6, p. 063115. DOI: 10.1063/1.4953888.

Wakelam, V. et al. (2012). 'A KInetic Database for Astrochemistry (KIDA).' In: *The Astrophysical Journal Supplement Series* 199.1, p. 21. DOI: 10.1088/0067-0049/199/1/21.

Weinberg, D. H. (2017). 'On the Deuterium-to-hydrogen Ratio of the Interstellar Medium.' In: *The Astrophysical Journal* 851.1, p. 25. DOI: 10.3847/1538-4357/aa96b2.

White, G. J. (1997). 'Using CO Isotopes to Probe the ISM.' In: *CO: Twenty-Five Years of Millimeter-Wave Spectroscopy*. Ed. by W. B. Latter, S. J. E. Radford, P. R. Jewell, J. G. Mangum, and J. Bally. International Astronomical Union, Union Astronomique Internationale. Springer Netherlands, pp. 101–109. DOI: 10.1007/978-94-011-5414-7_19.

Wilson, T. L. (1999). 'Isotopes in the interstellar medium and circumstellar envelopes.' In: *Reports on Progress in Physics* 62.2, p. 143. DOI: 10.1088/0034-4885/62/2/002.

Yariv, A. (1997). *Optical Electronics in Modern Communications*. 5th ed. Oxford: Oxford University Press.

Yu, S., J. C. Pearson, B. J. Drouin, T. Crawford, A. M. Daly, B. Elliott, and T. Amano (2015). 'Rotational spectroscopy of vibrationally excited N_2H^+ and N_2D^+ up to 2.7 THz.' In: *Journal of Molecular Spectroscopy* 314, pp. 19–25. DOI: 10.1016/j.jms.2015.05.001.

Zhaunerchyk, V., R. D. Thomas, W. D. Geppert, M. Hamberg, M. Kaminska, E. Vigren, and M. Larsson (2008). 'Dissociative recombination of D_2H^+: Comparison between recent storage-ring results and theoretical calculations.' In: *Physical Review A* 77.3, p. 034701. DOI: 10.1103/PhysRevA.77.034701.

Zymak, I., M. Hejduk, D. Mulin, R. Plašil, J. Glosík, and D. Gerlich (2013). 'Low-Temperature Ion Trap Studies of $N^+(3^{P}_{ja}) + H_2(j) \longrightarrow NH^+ + H$.' In: *The Astrophysical Journal* 768.1, p. 86. DOI: 10.1088/0004-637X/768/1/86.

Part IV

ATTACHED PUBLICATIONS

A

BIBLIOGRAPHIC RECORD

The articles attached to this thesis were chosen to best represent the authors main contributions in terms of scientific publications of the achieved results.

Kálosi, Á., P. Dohnal, D. Shapko, Š Roučka, R. Plašil, R. Johnsen, and J. Glosík (2017). 'Overtone spectroscopy of N_2H^+ molecular ions–application of cavity ring-down spectroscopy.' In: *Journal of Instrumentation* 12.10, p. C10010. doi: `10.1088/1748-0221/12/10/C10010`.

Plašil, R., P. Dohnal, Á. Kálosi, Š. Roučka, D. Shapko, S. Rednyk, R. Johnsen, and J. Glosík (2018). 'Stationary afterglow apparatus with CRDS for study of processes in plasmas from 300 K down to 30 K.' In: *Review of Scientific Instruments* 89.6, p. 063116. doi: `10.1063/1.5036834`.